

© 2020

VIKTOR DUBOVOY

ALL RIGHTS RESERVED

DEVELOPMENT OF NOVEL ANTIMICROBIAL FUNCTIONAL MATERIALS
COMPRISING QUATERNARY AMMONIUM COMPOUNDS AND MESOPOROUS SILICA
NANOPARTICLES

By

VIKTOR DUBOVOY

A dissertation submitted to the

School of Graduate Studies

Rutgers, The State University of New Jersey

In partial fulfillment of the requirements

For the degree of

Doctor of Philosophy

Graduate Program in Chemistry and Chemical Biology

Written under the direction of

Dr. Tewodros Asefa

And approved by

New Brunswick, New Jersey

May, 2020

ABSTRACT OF THE DISSERTATION

DEVELOPMENT OF NOVEL ANTIMICROBIAL FUNCTIONAL MATERIALS COMPRISING QUATERNARY AMMONIUM COMPOUNDS AND MESOPOROUS SILICA NANOPARTICLES

By VIKTOR DUBOVOY

Dissertation Director:

Prof. Dr. Tewodros Asefa

Over the past several decades, mesoporous silica nanoparticles (MSNs) have attracted a tremendous deal of interest in areas such as catalysis, drug delivery systems (DDSs), sensing, environmental remediation, and nanoelectronics due to their unique structures and properties. Since their discovery, research focused on MSN-based drug delivery systems has increased exponentially each year.¹ The current body of work utilizes MSNs as a delivery vehicle to host a variety of quaternary ammonium compounds (QACs) for biomedical applications. The results reported herein demonstrate that the combination of porous materials with QACs can have a significant synergistic effect on the antimicrobial properties of the resulting material which paves the way for further studies to build upon this enhancing effect.

In chapter 2, benzalkonium chloride (BAC) was used as a template to synthesize mesostructured silica nanoparticles for antimicrobial applications.¹ The synthesized material comprised a relatively high density (0.56 g per 1 g of SiO₂) of BAC and a high surface area (1500 m² g⁻¹) after calcination. In the physiologically-relevant pH range of

4.0 to 7.4, BAC was released in a controlled manner showing dependence between pH and rate of release. The material demonstrated inhibition of the gram-positive *Staphylococcus aureus* and the gram-negative *Salmonella enterica* at 10 and 130 mg/L, respectively. Taking into consideration a *ca.* 36 wt.% loading content of BAC within the BAC-SiO₂ material, this correlates to an inhibition of *S. aureus* with 4 mg/L BAC which is a 10-fold enhancement compared to the minimum inhibitory concentration (MIC) of 40 mg/L for pure BAC. These results indicate that either the release of an antimicrobial drug (*e.g.*, BAC) from the MSNs is not mandatory to achieve bactericidal efficacy or the host-guest relationship between BAC and silica MSNs boosts antimicrobial activity.

In chapter 3, cetylpyridinium chloride (CPC) was complexed with ZnCl₂ to yield cetylpyridinium tetrachlorozincate with a stoichiometry of C₄₂H₇₆Cl₄N₂Zn where zinc exists as [ZnCl₄]²⁻ tetrahedra. This novel material demonstrated parity antimicrobial efficacy as compared to pure CPC despite the fact that *ca.* 16% of the material is replaced with bacteriostatic ZnCl₂. A technique to load the novel material into porous frameworks was proposed and yielded a material with *ca.* 9.0 and 8.9 wt.% of CPC and Zn, respectively.

In chapter 4, a complex comprising chlorhexidine (CHX) with N-cyclohexylsulfamate (*i.e.*, cyclamate) was synthesized yielding a stoichiometry of [C₂₂H₃₂N₁₀Cl₂][C₇H₁₃O₃S]₂. This newly discovered material demonstrates excellent antimicrobial activity with a minimum inhibitory concentration (MIC) of 2.5 µg/mL for *Streptococcus mutans*. Moreover, this material is advantageous as compared to the indispensable chlorhexidine gluconate since the inactive gluconate ion is substituted with

the bioactive artificial sweetener (*i.e.*, cyclamate) which has the potential to mitigate the bitter taste commonly associated with chlorhexidine.

References

- (1) Dubovoy, V.; Ganti, A.; Zhang, T.; Al-Tameemi, H.; Cerezo, J. D.; Boyd, J. M.; Asefa, T., One-pot hydrothermal synthesis of benzalkonium-templated mesostructured silica antibacterial agents. *J. Am. Chem. Soc.* **2018**, *140* (42), 13534-13537.
- (2) Fazlara, A.; Ekhtelat, M., The disinfectant effects of benzalkonium chloride on some important foodborne pathogens. *Am. Eurasian J. Agric. Environ. Sci.* **2012**, *12* (1), 23-29.

DEDICATIONS

Dedicated to my parents,

Leonid Dubovoy and Tatyana Nazarova.

Brother, **Dmitriy Dubovoy.**

My fiancé and son,

Erika Regalado and Ethan Dubovoy.

Grandfather, **Ilya Dubovoy.**

Grandmother, **Lidiya Nazarova.**

ACKNOWLEDGEMENTS

The arduous journey of obtaining a doctorate degree, or any degree for that matter, is traversed through a long and winding road. This road, not unlike those ubiquitous throughout New Jersey, is filled with uneven and bumpy patches, unexpected detours, and perplexing roundabouts. While following along the path, one may find themselves astray or even arriving at a dead end. It is during these times that perseverance is challenged and we depend upon our family, mentors, and friends to provide the support needed to navigate back on track. Throughout my graduate studies, there have been numerous such occurrences and therefore this section of the thesis is dedicated to acknowledge those incredible people.

Firstly, I would like to thank the undergraduate, graduate, and auxiliary faculty of Rutgers University. In particular, my advisor, mentor, and friend, Dr. Tewodros Asefa, who has not only provided me with the necessary tools and skills to become a successful scientist, but also inspired me to constantly improve myself as a person and father. Additionally, my committee members Dr. Deirdre O'Carroll and Dr. Laura Fabris who have provided valuable research advice, feedback, and guidance. And last, but not least Dr. Gene Hall and Dr. Ralf Warmuth for their expertise and advice on instrumentation and chemical analyses and Dr. Alan Goldman who was instrumental in my admission to the doctorate program.

My sincere appreciation also goes out to the scientists of Colgate-Palmolive Company who have taught me a great deal throughout my internship. Specifically, Dr. Long Pan for his patience, breadth of knowledge that he bestowed upon me, and genuine interest in my academic success as well as overall well-being. Additionally, I would like

to thank Dr. Zhigang Hao, Dr. Christine Boyke, Dr. Richard Adams, Dr. Iraklis Pappas, and Dr. John Vaughn.

Moreover, my previous and current research group members have fully supported and encouraged me at every moment including: Dr. Vitor C. Almeida, Dr. Tais Larissa Silva, Dr. Heveline Follman, Dr. Rafael Silva, Dr. Xiaoxi Huang, and Dr. Xingquan (Andy) He. A special thanks to Dr. Katherine Koh and Tao Zhang for their invaluable support and collaboration.

Finally, I would like to express my deepest gratitude to my family: my grandfather and late grandmother who have fostered my learning since the age of four, most memorably through playing chess and reading, respectively; my mother and father who went to great lengths to allow me the opportunity of higher education in a seemingly foreign country after moving from Russia; my brother who fully supported me at every moment of my life and taught me how to be a better son, friend, and father; and, my fiancé and son whose love and support allowed me to persevere through the challenges along the way.

TABLE OF CONTENTS

ABSTRACT OF DISSERTATION	ii
DEDICATIONS	v
ACKNOWLEDGEMENTS	vi
TABLE OF CONTENTS	viii
LIST OF TABLES AND FIGURES	xi
CHAPTER 1	
<i>Ordered Mesoporous and Nanoporous Inorganic Materials via Self-Assembly</i>	
1.1 Introduction	1
1.1.1 Nanoscience and Nanotechnology	2
1.1.2 Mesoporous Materials	3
1.2 Types of Mesoporous Silicas	8
1.2.1 M41S-type Mesoporous Silicas	10
1.2.2 SBA-type Mesoporous Silicas	17
1.3 Synthetic Methods of Mesoporous Materials	19
1.3.1 Hydrothermal Synthesis	20
1.3.2 Non-aqueous Synthetic Routes	24
1.3.3 Mesoporous Materials by Post-synthesis	25
1.4 Properties of Mesoporous Materials	27
1.4.1 Surface Area	27
1.4.2 Pore Properties and Pore Size Distributions	29
1.4.3 Crystallinity	31
1.5 General Characterization Methods of Mesoporous Materials	32
1.5.1 Gas Porosimetry	33

1.5.2	Small Angle Powder X-ray Diffraction (PXRD) and Small Angle X-ray Scattering (SAXS).....	35
1.5.3	Transmission Electron Microscopy (TEM).....	36
1.5.4	Nuclear Magnetic Resonance (NMR) Spectroscopy.....	37
1.5.5	Thermogravimetric Analysis (TGA).....	40
1.5.6	X-ray Photoelectron Spectroscopy (XPS).....	41
1.5.7	Fourier Transform Infrared (FTIR) Spectroscopy.....	42
1.6	Applications of Mesoporous Materials.....	43
1.6.1	Biological and Drug Delivery Applications.....	43
1.7	Summary and Future Prospects.....	50
1.8	References.....	52

CHAPTER 2

One-Pot Hydrothermal Synthesis of Benzalkonium-Templated Mesostructured Silica Antibacterial Agents

2.1	Overview.....	60
2.2	Introduction.....	61
2.3	Experimental Section.....	63
2.4	Results and Discussion.....	68
2.5	Conclusion.....	88
2.6	References.....	90

CHAPTER 3

Synthesis, Characterization, and Investigation of the Antimicrobial Activity of Cetylpyridinium Tetrachlorozincate

3.1	Overview.....	94
-----	---------------	----

3.2 Introduction.....	95
3.3 Experimental Section.....	97
3.4 Results and Discussion.....	102
3.5 Conclusion.....	118
3.6 References.....	119

CHAPTER 4

Synthesis, Characterization, and Antimicrobial Investigation of a Novel Chlorhexidine Cyclamate Complex

4.1 Overview.....	122
4.2 Introduction.....	123
4.3 Experimental Section.....	126
4.4 Results and Discussion.....	129
4.5 Conclusion.....	145
4.6 References.....	146

CHAPTER 5

Conclusions and Perspectives.....	149
Appendix.....	154

LIST OF TABLES AND FIGURES

TABLES

Table 1.1. Pore sizes of ordered mesostructures obtained by various methods.....	30
Table 1.2. Common silicate species of mesoporous silica materials and their respective positions in ^{29}Si spectra.....	40
Table 2.1. Analysis of kinetic data for BAC desorption.....	80
Table 3.1. Crystal data and structure refinement for $(\text{CP})_2\text{ZnCl}_4$ at 100 K.....	107
Table 3.2. Crystal data and structure refinement for $(\text{CP})_2\text{ZnCl}_4$ at 298 K.....	108
Table 3.3. Statistical grouping information using Tukey method and 95.0% confidence..	111
Table 3.4. Elemental composition of powders used to prepare VSC reduction samples....	111
Table 3.5. Porosimetry results and SAXRD data.....	116
Table 4.1. Crystal data and structure refinement for CHX-cyclamate.....	130
Table 4.2. Selected bond lengths for CHX-cyclamate.....	133
Table 4.3. Selected bond angles for CHX-cyclamate.....	136
Table 4.4. MIC values for CHX-cyclamate, CHX-gluconate, and CHX-HCl.....	144

FIGURES

Figure 1.1. A representative scheme illustrating the potential use of functionalized mesoporous organosilica nanoparticles (MONs) for chemotherapy of tumors.....	4
Figure 1.2. (a) A transmission electron micrograph showing hexagonal channels, (b) a selected-area electron diffraction (SAED) pattern indexed as $hk0$ projection, (c) an X-ray diffraction pattern and (d) a N_2 adsorption isotherm of MCM-41.....	11

Figure 1.3. Formation of mesoporous materials by structure-directing agents (SDAs): (a) true liquid-crystal template and (b) cooperative liquid-crystal template mechanism.....	13
Figure 1.4. Structures of mesoporous M41S materials: (a) MCM-41 (2D hexagonal, space group <i>P6mm</i>), (b) MCM-48 (cubic, space group <i>Ia3d</i>), and (c) MCM-50 (lamellar, space group <i>P2</i>).....	16
Figure 1.5. Schematic illustration of the framework-composition alteration from traditional inorganic --Si--O--Si-- to organic–inorganic hybrid --Si--R--Si-- , transformation of bulk mesoporous organosilica into mesoporous organosilica nanoparticles of MONs, and their representative morphologies, nanostructures and applications in nanotechnology.....	45
Figure 1.6. Fraction of ibuprofen released from ibuprofen-loaded MCM-41 after 24 h in simulated body fluid (SBF).....	48
Figure 2.1. Schematic illustration of the synthetic procedure, drug release, and antimicrobial mode of action.....	63
Figure 2.2. Synchrotron-SAXS measurement of aqueous BAC/ NH_4OH solution prior to TEOS addition.....	69
Figure 2.3. SLS measurement of aqueous BAC/ NH_4OH solution prior to the addition of TEOS demonstrating scattering intensity (y-axis) versus diameter (x-axis).....	70
Figure 2.4. (a) ATR-FTIR spectra of lyophilized BAC, BAC- SiO_2 and calcined BAC- SiO_2 ; (b) thermogravimetric analysis (TGA) data plots of lyophilized BAC and as-synthesized BAC- SiO_2 ; (c) HR-TEM micrograph of calcined BAC- SiO_2 ; and (d) small-angle X-ray diffraction (SAXRD) pattern of calcined BAC- SiO_2	71
Figure 2.5. Differential scanning calorimetry (DSC) plots of BAC and BAC- SiO_2	72
Figure 2.6. (a) Normal and (b) enlarged TEM images of as-synthesized BAC- SiO_2	74

Figure 2.7. Nitrogen (77 K) sorption isotherms of calcined BAC-SiO ₂ and pore size distribution.....	75
Figure 2.8. UV-Vis spectrum of BAC in a quartz cuvette.....	76
Figure 2.9. (a) Release profile of BAC from BAC-SiO ₂ in PBS solution at pH 4.0, 5.0, 6.5, and 7.4. (b) Time and dose-dependent killing of <i>S. aureus</i> and <i>S. enterica</i> by BAC-SiO ₂ . (c) The percentage of <i>S. aureus</i> survival upon exposure to BAC and BAC-SiO ₂	78
Figure 2.10. Logarithmic variation of BAC fraction released over time in PBS pH 7.4.....	81
Figure 2.11. Logarithmic variation of BAC fraction released over time in HCl pH 4.0.....	81
Figure 2.12. Logarithmic variation of BAC fraction released over time for the second release in a fresh solution of HCl pH 4.0.....	82
Figure 2.13. pH measurements plotted against the concentration of BAC-SiO ₂	84
Figure 2.14. Growth analyses of (a) <i>S. enterica</i> and (b) <i>S. aureus</i> in the presence of NH ₄ OH.....	86
Figure 2.15. Time- and dose-dependent killing of <i>S. aureus</i> and <i>S. enterica</i> by NH ₄ OH, BAC-SiO ₂ , or SiO ₂	87
Figure 3.1. DSC plot of CPC and CPC-Zn material.....	103
Figure 3.2. XPS survey spectra of CPC and CPC-Zn material.....	104
Figure 3.3. Enlarged and normalized XPS spectra of the CPC and CPC-Zn material N1s peaks.....	105
Figure 3.4. Infrared absorption spectra of synthesized CPC-Zn material as well as CPC·H ₂ O and ZnCl ₂ precursors.....	106
Figure 3.5. Crystal structure of [(C ₂₁ H ₃₈ N) ₂][ZnCl ₄].....	108

Figure 3.6. Packing of $[(C_{21}H_{38}N)_2][ZnCl_4]$ along (a) 110 plane and (b) 100 plane at 100K.....	109
Figure 3.7. (a) Structure of $[(C_{21}H_{38}N)_2][ZnCl_4]$ at 298 K and (b) packing arrangement.....	110
Figure 3.8. A comparison of the PXRD patterns of the bulk sample, the calculated pattern at 298 K and the calculated pattern at 100 K.....	110
Figure 3.9. Inhibition of <i>S. aureus</i> (a), <i>S. mutans</i> (b), and <i>S. enterica</i> (c) with $ZnCl_2$, CPC and $(CP)_2ZnCl_4$. VSC reduction efficacy (d) of methyl mercaptan <i>via</i> GC.....	112
Figure 3.10. N_2 adsorption isotherms (77 K) for SBA-15, CPC@SBA-15 and CPC-Zn@SBA-15.....	115
Figure 3.11. BJH pore size distribution corresponding to the isotherms in Figure 3.10.....	115
Figure 3.12. SAXRD pattern of SBA-15 and $(CP)_2ZnCl_4$ @SBA-15.....	116
Figure 3.13. Infrared absorption spectrum of CPC-Zn@SBA-15 in comparison to CPC@SBA-15 and SBA-15.....	117
Figure 4.1. Molecular structure of chlorhexidine-cyclamate complex.....	124
Figure 4.2. View of the CHX unit with two cyclamate units.....	132
Figure 4.3. (a) The S-shaped CHX coils; and (b) depiction of the C-H---Cl hydrogen bonding interactions.....	132
Figure 4.4. (a) The cyclamate showing interaction with three CHX units; (b) the cyclamate dimer; (c) extension of dimers along the c-axis; and (d) alternating cyclamate molecules along the b-axis.....	134
Figure 4.5. Packing arrangement showing the network formation with CHX coils and cyclamate dimers.....	135

Figure 4.6. View of packing along (100) plane showing alternating cyclamate units..	136
Figure 4.7. Mass spectrum (positive mode) of CHX-cyclamate complex in methanol.....	137
Figure 4.8. Mass spectrum (negative mode) of CHX-cyclamate complex in methanol.....	138
Figure 4.9. MS/MS spectrum (negative mode) from the parent ion at $m/z = 681$	138
Figure 4.10. MS/MS spectrum (positive mode) from the parent ion at $m/z = 683$	139
Figure 4.11. MS/MS spectrum (positive mode) from the parent ion at $m/z = 863$	139
Figure 4.12. FTIR spectra of sodium N-cyclohexylsulfamate, CHX-HCl, CHX-gluconate, CHX-cyclamate crystals.....	140
Figure 4.13. ^1H NMR spectroscopy of crystal dissolved in deuterated DMSO.....	142
Figure 4.14. Chlorhexidine and cyclamate structures (a) with labelled protons and their corresponding COSY spectrum (b).....	143
Figure 4.15. MIC assays for CHX-cyclamate, CHX-gluconate, and CHX-HCl with (a) <i>S. mutans</i> and (b) <i>S. aureus</i>	144
Figure 4.16. MIC assay for CHX-cyclamate, CHX-gluconate, and CHX-HCl with <i>S. enterica</i>	145
Figure 5.1. Projected deaths (per year) attributable to antimicrobial resistance infections compared to other major causes of death in 2050.....	150

CHAPTER 1

Ordered Mesoporous and Nanoporous Inorganic Materials *via* Self-Assembly

1.1. Introduction

Since their discovery in the early 1990s, mesoporous silica materials have captured the attention of researchers worldwide because of their unique properties as well as their potential applications in catalysis, drug delivery, chromatography, separations, environmental remediation and nanoelectronics. Their properties and applications are largely dependent on their nanoporous structures and high surface areas, which allow the materials to support or carry various functional groups (*e.g.*, drug molecules). Furthermore, their properties can easily be tailored, as needed, by a simple modification of their surfaces with various functional groups. In this chapter, a brief historical background on mesoporous materials and the major synthetic methods used to make various mesoporous materials with different structures are discussed. Several notable mesoporous materials and their fundamental properties and potential applications in areas including catalysis, drug delivery, nanomedicine, and nanoelectronics are also included. Some of the unique advantages of these materials for various applications are highlighted by presenting some examples, such as stimuli-responsive, on demand delivery of anticancer drugs to targeted cells. Finally, conclusions and perspectives on where the field of mesoporous materials currently stands and what more may have to be done to fully utilize these materials in various commercial products are discussed.

1.1.1. Nanoscience and Nanotechnology

Nanoscience and nanotechnology, defined as the study and manipulation of matter with nanoscale sizes, still remain among the most rapidly advancing fields of science and technology today. According to most definitions, nanosized materials are materials with sizes in the range of 1-100 nm in at least one dimension, regardless of their compositions. But this definition should not be viewed in the strictest sense since materials below 1 nm and above 100 nm can still display related trends in properties as those having sizes within the traditional size range in the definition. In other words, matter with sizes below 1 nm or above 100 nm may still show nanoscale properties, rather than molecular or bulk properties, respectively.

Nanomaterials are captivating researchers' attentions mainly because of their inherent, unique nanoscale associated so-called quantum size properties and scalable nanoscale related features (*e.g.*, high surface areas and relatively large number of surface exposed atoms due to their small sizes). Thus, their properties not only are entirely different from those of their atomic/molecular or bulk counterparts but also change depending on their size, shape, morphology, etc. For example, nanomaterials with the same composition but different sizes can show colors that are different from one another or different from their molecular and bulk counterparts. They can also show much higher magnetic anisotropy than their bulk counterparts, etc. Hence, they are fascinating systems to study and explore. Furthermore, many of their unique properties can be taken advantage of and be utilized in potential applications ranging from catalysis to biomedicine.

One particular area where research in nanoscience and nanotechnology is extensively advancing is the development of synthetic methods to various new, “smart” and multifunctional nanomaterials to meet the need for the next generation of advanced materials and devices for nanoelectronics, nanophotonics, sensing, separations, catalysis, and drug delivery. The synthetic methods to produce nanomaterials can generally be classified into two groups: 1) bottom up synthesis, which involves the assembly of atoms and molecules, typically using chemical processes, and 2) top-down synthesis, which involves the crafting of bulk materials into nanosized products, typically using physical methods, and sometimes chemical, electrochemical and other methods. Furthermore, depending on the specific reagents and materials involved, these two synthetic methods can be or have successfully been applied together in complimentary ways, or in tandem, to produce the desired nanomaterials.

1.1.2. Mesoporous Materials

Mesoporous materials are a class of nanostructured materials that possess nanoporous structures, nanometer-sized pores, high surface areas, large pore volumes, and nanosized and micro-sized particles. According to the International Union of Pure and Applied Chemistry (IUPAC), nanoporous materials are classified into three major groups, regardless of their compositions and the overall sizes of their particles: 1) microporous, which are nanoporous materials whose pores are less than 2 nm (*e.g.*, zeolites); 2) mesoporous, which are nanoporous materials with pore sizes between 2-50 nm; and 3) macroporous, which are nanoporous materials whose pore sizes are above 50 nm.

Due to their nanometer pores, nanoporous materials (including mesoporous materials) possess several properties that are sought after from nanoscale materials and that are useful for many of the applications mentioned above. For instance, owing to their high surface areas and tunable nanometer pores, mesoporous materials are suitable as support or host materials for a variety of catalytic groups and bioactive guest molecules to generate heterogeneous catalysts or bioseparation media. Furthermore, since their particles size are often, or can intentionally be made, in nanometer or micrometer scales, they can possess additional, external surface areas. They can, therefore, serve as good adsorbents for pollutants and as host-guest inclusion platforms for adsorption and release of drugs and bioactive agents (an example is illustrated in Figure 1.1).¹

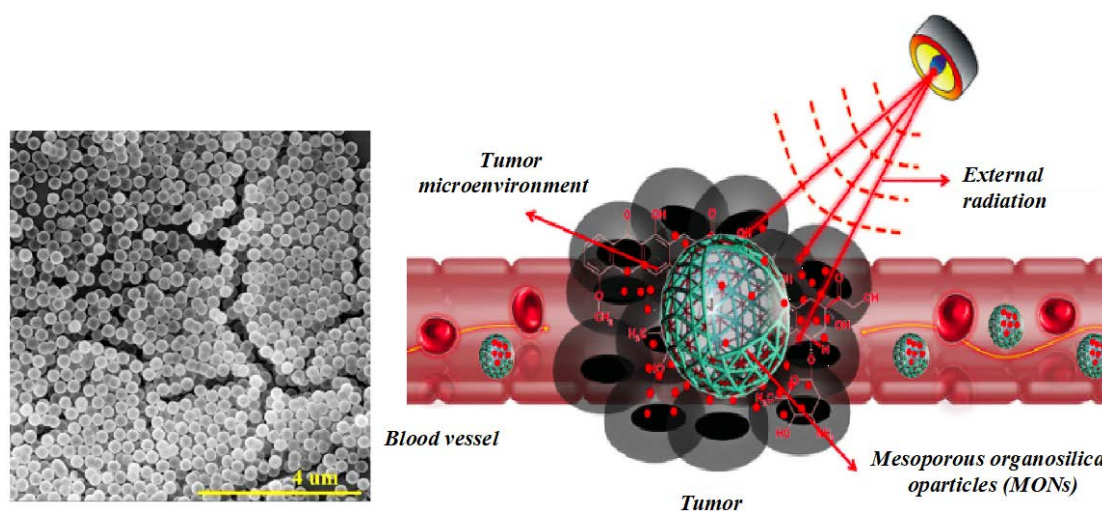


Figure 1.1. A representative scheme illustrating the potential use of functionalized mesoporous organosilica nanoparticles (MONs) for chemotherapy of tumors. Reprinted from Chen, Y.; Meng, Q.; Wu, M.; Wang, S.; Xu, P.; Chen, H.; Li, Y.; Zhang, L.; Wang, L.; Shi, J. *J. Am. Chem. Soc.* **2014**, *136*, 16326–16334, Copyright (2014), with permission from American Chemical Society.

Although, as nanostructured materials, mesoporous materials can be synthesized by one of the two general synthetic approaches mentioned above, the first one (bottom-up synthesis) is more preferred and more widely applied. In particular, the bottom-up synthetic method involving the so-called supramolecular assembly is quite versatile as it allows control over the arrangement of the precursors involved, and produces a range of hierarchical mesostructures with a broad range of compositions, pores sizes and pore types. Like the synthesis of many other materials, the synthesis of mesoporous materials, especially using such self-assembly techniques, requires optimization of the synthetic conditions, including temperature, pH, concentrations of reagents and the use of appropriate self-assembling molecules and other specific conditions that may allow the given precursors to properly self-assemble. A slight change in any one or many of the synthetic parameters or conditions can lead to different arrangement of atoms and molecules, or mesoporous materials with significantly different structures and properties. The synthesis of mesoporous materials with optimum structures and desired properties and potential applications thus requires perfecting all of these synthetic conditions and parameters as well as using the right combinations of reagents under optimal synthetic conditions. To find the optimal synthetic conditions that can generate the “ideal” or desired mesoporous materials, experimental investigations are now often coupled with theory and computational studies of self-assembly processes.

Fortunately, the properties of existing mesoporous materials can easily be further tuned or improved simply by placing some functional groups on the materials’ surfaces and/or within the materials’ pores using various synthetic routes. This can lead to the most desired mesoporous materials that may be hard to obtain directly by the self-

assembly synthesis. In fact, the functionalized mesoporous materials obtained by such further synthetic modifications are among those that have been demonstrated to have many potential advanced applications. However, this too (*i.e.*, the functionalization of mesoporous materials with various groups) may still require controlled synthetic conditions and appropriate reagents, some of which have to be designed and synthesized.

Additionally, by adjusting the various synthetic conditions involved, the pores of mesoporous materials can be tuned (as small or large monodisperse pores), or can intentionally be made to have two or three different pore sizes (bimodal, trimodal, etc.). These may, in turn, allow the materials to have useful mass transfer and other properties for various applications, especially those that involve the transport of reactants and analytes through the materials' pore networks.

Besides their nanoscale structural features and functional groups, mesoporous materials can be synthesized in different forms: in powder, thin film and monolithic forms as well as with nanoscale and macroscale dimensions, and also sometimes different shapes. Mesoporous materials also often inherently come with many other desirable and useful properties such as high mechanical strength, thermal stability, and chemical stability under a wide pH range while retaining their ordered pore structures, pore diameters, and overall morphologies.

The compositions of mesoporous materials can vary widely as well. In fact, their composition is one way by which these materials are classified. Based on composition, they can be classified as mesoporous silica, mesoporous titania, mesoporous zirconia, mesoporous organosilica, etc. Binary and ternary mesoporous oxides are also known.

Other mesoporous materials such as mesoporous carbons, organosilicas, and polymer-coated mesoporous metal oxides can be derived from the original mesoporous materials by additional synthetic steps as well. The current work focuses predominantly on mesoporous silicas.

The surfaces of mesoporous silicas (both internal and external) consist of some residual uncondensed hydroxyl groups (also called silanol or Si-OH groups), whose relative density can be controlled by various post-synthetic treatments. For example, high temperature treatment under inert atmosphere reduces the density of Si-OH groups. On the other hand, the treatments of the materials with H₂O₂ or water, especially at high temperature can hydrolyze the Si-O-Si bonds and thereby increase the density of Si-OH groups. Adjusting the density of the surface hydroxyl groups, in turn, indirectly enables one to control the density of other functional groups that can be placed on the materials by grafting onto the Si-OH groups, and thereby to tailor the materials' properties.² For example, a smaller density of surface Si-OH groups enables easier diffusion of reactants, products, or guest molecules in and out of the mesopores. On the other hand, placing a larger density of grafted groups by intentionally producing a larger density of surface Si-OH groups on the original material may result in functionalized pores that can serve as high adsorption capacity molecular sieves.³ Additionally, the pores of such materials may allow the diffusion of certain molecules but not others, depending on the size of the molecules or the ability of the molecules to interact with the high-density surface functional groups. Because they are both easier to synthesize and to functionalize their surfaces, mesoporous silica-based materials are particularly suited and are advantageous

for these purposes. All of these properties as a whole, thus, make mesoporous silica materials highly interesting and versatile for numerous applications.

The first major reports of the synthesis of well-ordered mesoporous materials by supramolecular self-assembly of molecular building blocks, with the aid of simple, conventional self-assembling surfactants, was independently reported in the early 1990s by two research groups, namely Yanagisawa *et al.* at Waseda University (Japan)⁴ and by Kresge *et al.* at Mobil (now ExxonMobil) Company (USA).⁵ The pores of these original materials were around 3-4 nm in size, although several methods have now been known to make the pores of these types of materials larger. Meanwhile, the synthesis of SBA-type (where SBA stands for Santa Barbara Amorphous) mesoporous silicas with hexagonal array of pores with diameters as high as 30 nm by Zhao *et al.*⁶ at the University of California, Santa Barbara (USA) in 1998 advanced the field of mesoporous materials further. Like the first materials, SBA-type materials were synthesized also *via* the method of self-assembly of molecular building blocks, but using block co-polymers, rather than simple surfactants, as the amphiphilic self-assembling agents. Besides these, there are now several other mesoporous materials that have been synthesized by similar self-assembly methods but using different types of reagents.

1.2. Types of Mesoporous Silicas

Mesoporous silicas are mesoporous materials whose structures are literally built with silica frameworks, and consist of silicon and oxygen atoms and some residual hydrogens in the form of silanol groups (isolated, geminal, or vicinal). A detailed description on synthesis of these materials are provided in Section 1.3 below.

The synthesis of mesoporous silicas *via* self-assembly is typically achieved through the hydrolysis and condensation of silicate precursors (*e.g.*, tetraethyl orthosilicate or TEOS) in the presence of spontaneously self-assembling surfactant templates in aqueous solutions. Depending on how ordered the self-assembly processes proceed or not, ordered or disordered mesostructured silica materials templated by the surfactant micelles can form. Upon removal of the surfactant templates, either by 1) calcination at higher temperature, typically above 350 °C, or 2) solvent-extraction in acidic or organic solutions, mesoporous silicas (ordered or disordered) ultimately form. It is worth mentioning that the surfactant micelle assemblies are largely responsible for the resulting mesoporous structures, pore sizes, pore volume and surface area as well as the types of ordered arrangement of the pore structures in these materials.

As mentioned above, research in mesoporous materials has significantly expanded since the discovery of the mesoporous silica materials by the Kuroda group at Waseda University (Japan)⁴ and the Kresge group at Mobil Oil Corporation (USA).⁵ Prior to these two independent reports in the early 1990s, the prominent inorganic nanoporous materials known and utilized (for example, in catalysis and sorption applications) were zeolites, especially aluminosilicate-based ones,⁷ which have pore sizes limited to less than *ca.* 1.5 nm. Two and a half decades after the first mesoporous materials were reported, the type and number of mesoporous silica materials that have been reported in the literature have been growing and are now numerous. Depending on the synthetic methods applied to make the materials or the synthetic laboratory in which they were first synthesized, the mesoporous materials were given different types of names, including M41S-, SBA-, FSM-, MSU-, KIT-, FDU-, CK-, KSW-, DAM-, JLU-, IBN-, UK-, AMS-, and CMI-

types.^{8,35-40} Among them, M41S-type mesoporous silicas are the most widely investigated for applications in catalysis, drug delivery, and imaging.

1.2.1. M41S-type Mesoporous Silicas

The M41S family of mesoporous materials comprises a variety of distinct structures, which collectively exhibit the common characteristic of highly ordered mesoporous structures and narrow pore size distributions in the range of *ca.* 1.5 – 20 nm.⁹ The M41S family is further divided into three sub-groups based on the type of ordered arrangement of frameworks the materials possess; *i.e.*, one-, two- or three-dimensional ordered structures. These are also respectively known as: MCM-41, which has a hexagonal arrangement of porous silica frameworks (*P6mm* symmetry); MCM-48, which has a cubic arrangement (*Ia-3D* symmetry) of mesopore networks; and MCM-50, which has a lamellar arrangement of pore frameworks. These variations in the arrangement of the channel pores of mesoporous materials arise from the way by which the surfactant templates self-assemble. This, in turn, depends on the type of the surfactant used, the surfactant's critical micelle concentration (CMC), the relative concentration of the surfactant in the silicate/surfactant solution, and other factors such as the reaction temperature and the ionic strength of the reaction mixture. By changing any of these synthetic parameters and conditions, different self-assembled surfactant/silicate structures, and consequently, the different members of the M41S family of materials can be obtained.

Among the M41S family, MCM-41 is the most prominent one and is also the one that is widely studied and considered for various applications in catalysis, sensing,

adsorption, host-guest inclusion, drug delivery, etc. MCM-41 possesses regular arrays of uniform hexagonally-arranged 1D channels (see Figure 1.2a) with tunable pore diameters in the range of 1.6 to 10 nm, based on the choice of surfactant template, additional chemicals such as micelle swelling agents, and reaction conditions employed to synthesize it.

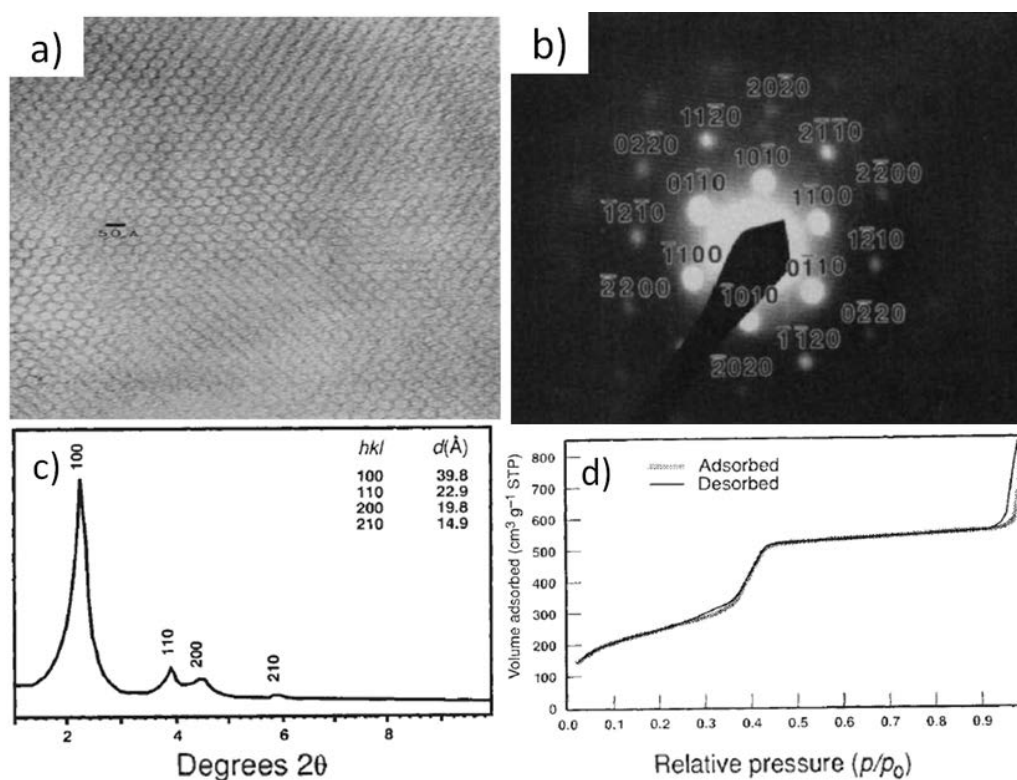


Figure 1.2. (a) A transmission electron micrograph showing hexagonal channels, (b) a selected-area electron diffraction (SAED) pattern indexed as $hk0$ projection, (c) an X-ray diffraction pattern and (d) a N_2 adsorption isotherm of MCM-41. Reprinted from Kresge, C. T.; Leonowicz, M. E.; Roth, W. J.; Vartuli, J. C.; Beck, J. S., *Nature* **1992**, 359, 710–712, Copyright (1992), with permission from Nature Publishing Group.

MCM-41 is typically synthesized by using cetyltrimethylammonium bromide (CTAB) or analogous surfactants as templates. After the self-assembly of the surfactant micelles with the hydrolyzed silicate precursors, followed by significant condensation of the silicate species around the surfactant micelles, takes place, the internal templates are removed to yield the mesoporous structures. In the initial disclosure of MCM-41, the synthesis was conducted using the combination of cationic cetyltrimethylammonium ion (comprising a mixture of hydroxide and chloride counter-anions) with alumina, tetramethylammonium silicate, and precipitated silica. Subsequent hydrothermal treatment, filtration of the reaction mixture, and calcination of the solid product yielded a material with a periodic lattice of hexagonal pores with a characteristic electron diffraction pattern along the c-axis as shown in Figure 1.2b and a (100) interplanar d -spacing of *ca.* 4 nm (40 Å) as shown in Figure 1.2c. The largest advantage of the resulting material became evident from its exceptionally large surface area, large pore volume, and narrow pore size distribution, which were expected to have various applications. When their surface area and pore volumes are measured *via* gas adsorption (see section 1.5.1),¹⁰ surface areas and pore volumes above 1,000 m² g⁻¹ and 1.1 cm³ g⁻¹, respectively, (see Figure 1.2d) are commonly obtained for these types of materials. Furthermore, typically, MCM-41 has pores around 3-4 nm in diameter (which are bigger than those of zeolites), good hydrothermal stability, and good thermal stability at high temperature and pressure. Thus, the material is suitable as a host or support material for a variety of guest molecules or as a scaffold for a wide array of functional groups to produce various heterogeneous catalysts, drug delivery systems and separation media.¹¹⁻¹⁴ In fact, various separation techniques have been successfully developed by taking

advantage of these structural features of MCM-41 material.¹⁵⁻¹⁹ Many other potential applications have also been widely demonstrated for MCM-41 materials (see section 1.6).

It has been debated by different researchers that the formation of mesoporous materials by structure-directing agents (SDAs) follows either a true liquid-crystal templating process or a cooperative liquid-crystal templating process as shown in Figure 1.3.²⁰ Although the mechanism by which mesoporous silicas are formed was long a matter of debate, it is now widely accepted that a stepwise process where the surfactant templates first self-assemble into an ordered hexagonal array of micelles, as illustrated in Figure 1.3, is part of the first major steps. Then, silane precursors hydrolyze and condense around the surfactant micelles to yield ordered silica frameworks. Finally, solvent extraction or calcination at temperatures $> 350\text{ }^{\circ}\text{C}$ (as shown in Figure 1.3) removes the micelle templates and yields ordered mesopore structures with a symmetry

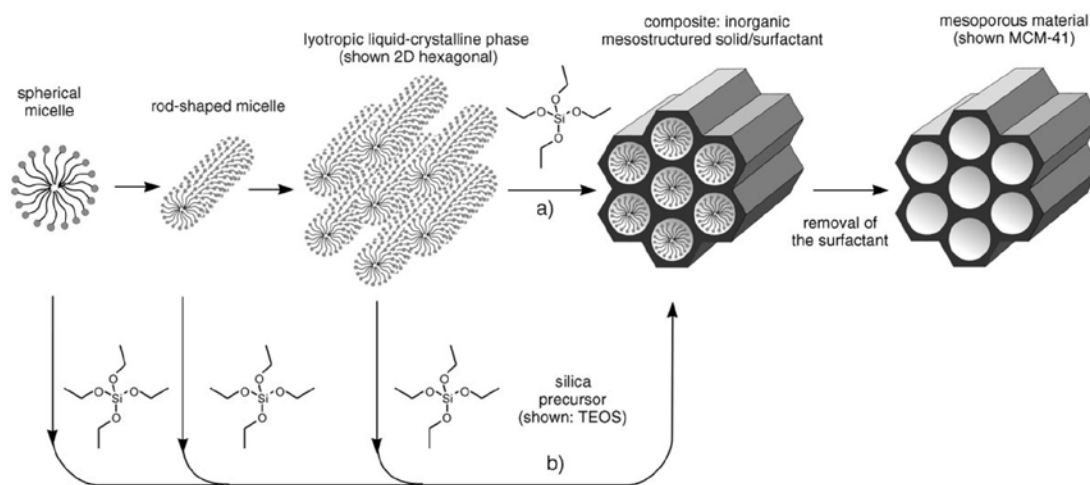


Figure 1.3. Formation of mesoporous materials by structure-directing agents (SDAs): (a) true liquid-crystal template and (b) cooperative liquid-crystal template mechanism. Reprinted from Hoffmann, F.; Cornelius, M.; Morell, J.; Froba, M., *Angew. Chem. Int. Ed.* **2006**, *45*, 3216–3251, Copyright (2006), with permission from Wiley VCH.

corresponding to the way the micelle templates are self-organized. The synthesized mesoporous solid material typically exhibits characteristic reflections in the low angle (2θ smaller than 8°) region of the X-ray diffraction (XRD) pattern (see Figure 1.2c), which can be indexed on the hexagonal unit cell with $a \approx 4.5$ nm.

The “liquid-crystal templating” (LCT) mechanism proposed by Beck *et al.*,²¹ which describes the formation of MCM-41 in terms of a surfactant liquid crystal serving as an organic template, unlocked many tangential synthetic routes that led to various other highly ordered mesoporous silica materials. Most of them utilized surfactant self-assembly and electrostatic interaction between template and silicate species. In the above examples, the synthetic pathways involve the organization of cationic quaternary ammonium surfactants and anionic silicate species (S^+T^-), *via* electrostatic attraction, producing three-dimensional (3D) periodic dual-phase lattices. However, it is feasible to produce parity mesoporous silica materials by utilizing reverse charge matching (S^-T^+)²² or even systems where surfactant and silica precursors carry the same charges (S^+XT^+ , where X^- is a halide anion or a charge mediator; or S^-M^+T , where M^+ is an alkali metal ion or a charge mediator).²³ The latter are achieved by purposely introducing oppositely charged inorganic species in the reaction mixtures in order to mediate the similarly charged surfactant moieties and silicate species.

Taking it a step further and expanding upon the aforementioned ionic-driven LCT mechanism, several other mechanisms have since been developed that take advantage of organic-inorganic self-assembly interaction other than those based on purely ionic ones. To this end, ordered mesoporous silicates have also been successfully synthesized under neutral conditions by employing neutral (S^0T^0)²⁴ or non-ionic surfactants (N^0T^0),²⁵ in

which hydrogen bonding between the surfactants and the silicate species is believed to be the force dictating their self-assembly and self-organization. In yet another templating mechanism, termed ligand-assisted LCT, mesoporosity is achieved by covalent bonding of the inorganic and the organic species during the surfactant self-assembly process, and then removal of the templates.²⁶ Alternative synthetic approaches where non-amphiphilic molecules are used as templating agents have also been successfully executed for making other mesoporous silicate materials.²⁷

Besides MCM-41, Mobil Oil Corporation simultaneously developed the other two members of M41S materials (*i.e.*, MCM-48 and MCM-50) by utilizing a similar electrostatic self-assembly synthetic route between cationic surfactants and anionic silicate precursors.²¹ Although the synthetic routes are similar, the latter two materials (see Figures 1.4b-c) are obtained by changing the ratio of silica precursor (silicate species) to CTAB (surfactant) in the reaction mixture^{28,29} or by replacing CTAB with gemini surfactants.³⁰ MCM-48 contains 3D channel networks running along [111] and [100] directions, and the morphology of the particles often resembles a distorted octahedra in electron microscope experiments.³¹ MCM-50 (see Figure 1.4c) has a lamellar structure, which often lacks structural integrity during template removal, and is thus of less scientific and industrial importance.

Due to their versatile properties, the M41S family of mesoporous silicas was quickly realized to have potential applications in many areas soon after its discovery in the early 1990s. Furthermore, many scientists have since focused on finding pore expansion synthetic routes that could lead to mesoporous silicas with even larger pore dimensions than the aforementioned materials. Some of these efforts have paid off. For

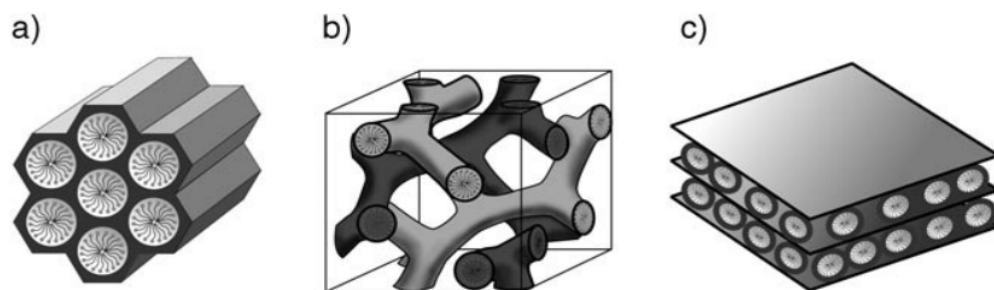


Figure 1.4. Structures of mesoporous M41S materials: (a) MCM-41 (2D hexagonal, space group $P6mm$), (b) MCM-48 (cubic, space group $Ia3d$), and (c) MCM-50 (lamellar, space group $P2$). Reprinted from Hoffmann, F.; Cornelius, M.; Morell, J.; Froba, M., *Angew. Chem. Int. Ed.* **2006**, 45, 3216–3251, Copyright (2006), with permission from Wiley VCH.

instance, while MCM-41, prepared with cationic cetyltrimethylammonium (CTA^+) surfactants, typically exhibits a d_{100} spacing of *ca.* 4 nm and pore sizes between 2 to 3 nm after calcination,⁶ by prolonging the duration of thermal treatment during synthesis³² or post-synthesis,³⁰ the pore sizes of the materials can be expanded to *ca.* 5 and 6 nm, respectively. The pores can be expanded significantly, up to 10 nm, by incorporating organic co-solvents (or so-called micelle swelling agents), such as 1,3,5-trimethylbenzene (TMB), during synthesis.^{5,21} Unfortunately, MCM-41-like materials with significantly larger pore dimensions, prepared *via* such co-solvent pore expansion synthetic routes, often have a substantially lower degree of ordered structure as evidenced by their extremely broad or less-resolved XRD peaks.³⁰

1.2.2. SBA-type Mesoporous Silicas

Six years after the discovery of M41S-type mesoporous silica materials, Santa Barbara Amorphous (SBA) mesoporous silica materials, which have significantly larger pore sizes than MCMS-type materials, were reported.⁶ The synthesis of these materials was attained by the self-assembly of silica precursors using block-copolymers as amphiphilic templates, under slightly different synthetic conditions compared with those employed for making M41S-type materials. Typically, poly(alkylene oxide) triblock copolymers (*e.g.*, Pluronic®) comprising alternating segments of poly(ethylene oxide) and poly(propylene oxide) are used as the SDAs for the synthesis of the SBA-type materials. These amphiphilic molecules are good SDAs for making mesoporous materials not only because they generally allow the formation of larger pores in mesoporous materials, but also because they are commercially available and biodegradable. Utilization of such amphiphilic triblock copolymers as SDAs during liquid crystal templating in acidic environment under optimized synthetic conditions yields well-ordered hexagonal (space group $P6mm$) mesoporous silica structures (*e.g.*, SBA-15). In general, favorable synthetic conditions for SBA-15, one of the most common SBA-type materials, includes the use of 0.5-6 % triblock copolymer, poly(ethylene oxide)-poly(propylene oxide)-poly(ethylene oxide) triblock copolymer (or Pluronic, $\text{PEO}_x\text{PPO}_y\text{PEO}_x$, most specifically P123 or $\text{EO}_{20}\text{PO}_{70}\text{EO}_{20}$), with silicate precursor at a reaction temperature between 35-80 °C and under very acidic conditions (typically $\text{pH} < 2$). Since both the polymer and the hydrolyzed silicate are positively charged under these conditions, the self-assembly mechanism leading to the material has been proposed as $(\text{S}^+\text{X}^+\text{T}^+)$ -type.³³ The polymer can be removed by solvent extraction (*e.g.*, in ethanol) or

calcination above *ca.* 300 °C for a few hours (*ca.* 3 h), and after which, a highly ordered mesoporous SBA-15 with larger pores (~8 nm) and thicker silica walls (~4 nm) results. The resulting material typically exhibits a BET surface area up to *ca.* 1,000 m² g⁻¹, a narrow pore size distribution ranging from 4.6 to 30 nm, a pore volume up to 0.85 cm³ g⁻¹, and thicker silica walls (ranging from 3.1 to 6.4 nm) as compared to that of MCM-41, and thus with highly desirable thermal stability.

It is noteworthy that the different categories of mesoporous silicas (*e.g.*, MCM, SBA) consist of multiple materials exhibiting different space groups, pore size ranges, and particle morphologies. In the case of SBA materials, besides SBA-15, there is another important, yet less commonly studied material called SBA-16. This material is also synthesized using a triblock copolymer (EO₁₀₆PO₇₀EO₁₀₆) with concentrations of *ca.* 3-5% under acidic conditions and mild temperatures.³⁴ However, generally polymer template concentrations lower than 3% and higher than 5% yield amorphous silica and silica gel materials, respectively. The as-synthesized SBA-16 shows a strong XRD reflection corresponding to d₁₁₀-spacing of 12.4 nm, which shifts by 0.5-0.7 nm upon calcination at 500 °C for 6 h. The XRD reflections can be indexed to a cubic structure (*Im* $\bar{3}m$) with *a* = 17.6 or 16.6 nm for as-synthesized and calcined products, respectively. Moreover, TEM images indicate that the material has a three-dimensional cubic cage structure. Calcined SBA-16 possesses a typical pore size of 5.4 nm, a pore volume of 0.45 cm³ g⁻¹, and a BET surface area of 740 m² g⁻¹.

1.3. Synthetic Methods of Mesoporous Materials

The synthesis of mesoporous silica is carried out by the bottom-up self-assembly method. In the synthesis, typically a silica precursor, which is generally an alkoxysilane or a halogenated silane, undergoes hydrolysis and condensation, in basic or acidic aqueous solutions, in the presence of amphiphilic templates (surfactant or block copolymer micelles). The resulting hydrolyzed silicate species condense around the spontaneously self-assembled amphiphilic molecules and form different types of mesostructured silica materials. There are several key parameters in the reaction mixture that can dictate these self-assembly processes, leading to different structures/materials: pH, temperature, concentration of reagents, auxiliary chemical agents (*e.g.*, co-solvents, inorganic salts), type of silica precursors, etc.

Notably, the pH, which can be controlled by adding acids or bases in the reaction mixtures, is an important parameter, as higher or lower pH speeds up the hydrolysis and condensation of silicate species, and also dictates whether or not a mesostructured silica forms, and if so, what its structure would be. In the case of temperature, although condensation of silica can occur at room temperature, increasing the temperature of the reaction mixture increases the hydrolysis and condensation kinetic rates as well as the degree of silica condensation, thereby allowing a robust mesostructured material to form sooner. Furthermore, at higher temperatures, the water and alcohol, formed as by-products during the hydrolysis and condensation processes, evaporates and facilitates the formation of a more condensed and physically robust mesoporous silica framework.

The specific supramolecular self-aggregates of amphiphilic molecules (or micelles), which serve as the SDAs or templates for the silicate species, form only under

certain conditions. So, besides temperature and pH, factors such as the type of silane precursor, the type of surfactant, and the concentrations or relative ratios of the reagents involved can all play important roles in the formation of the mesoporous materials. Conversely, optimal ratios of the different reagents (acid/base, silica precursor, surfactant, etc.) and appropriate reaction conditions (temperature, pH, reaction time, etc.) should be used in order to obtain the right type of self-assembled mesostructured silica. This also means, the synthetic conditions and the relative amount of precursors and reagents should be optimized to ultimately yield the desired self-assembled surfactant and silicate aggregates, and thereby mesostructured silica materials.

As a specific example, under certain conditions TEOS or tetramethyl orthosilicate (TMOS), which hydrolyze to form silicate species, spontaneously self-assemble with CTAB surfactant templates *via* electrostatic or hydrogen bonding interactions and lead to hierarchically ordered mesostructured silica. The CTAB templates are then removed by calcination or solvent-extraction to produce the mesoporous silica materials. Mesoporous silicas with different pore sizes and geometry can be produced by simply varying the relative amount of TEOS or TMOS with respect to CTAB used in the reaction mixtures or by changing the type and size of surfactant molecule used for the syntheses of the materials.

1.3.1. Hydrothermal Synthesis

Typical hydrothermal synthesis of ordered mesoporous silica materials involves the sol-gel process under hydrothermal conditions, entailing aqueous solutions at high temperature (100-200 °C) and pressure. Although the particular synthetic procedures and

conditions vary to a certain degree, the hydrothermal synthesis usually begins with dissolution of the surfactant(s) in a solvent (*i.e.*, water). As water is the most preferred and convenient solvent for economical and toxicological reasons, hydrothermal synthesis of mesoporous materials is appealing. Subsequent addition of suitable silicate precursors (*e.g.*, TEOS, TMOS) in the presence of acid or base catalysts leads to the hydrolysis of silica precursors and yields a homogeneous sol of silicate monomers and oligomers. The silicates formed *in situ* interact and assemble with the surfactant(s) micelles, *via* electrostatic, hydrogen-bonding, Van der Waals, or covalent interaction, and undergo continuous condensation and aggregation, eventually precipitating as a gel.

The formation of mesostructured silica under hydrothermal condition is relatively fast, which can generally take *ca.* 5 or 30 min with cationic or nonionic surfactants, respectively.⁸ It is worth noting here that the hydrothermal treatment significantly facilitates the condensation reaction and the formation of silica structures in the material. However, the rate of formation of mesostructured silica can additionally depend on the hydrolysis rate of the specific silica precursor. For example, for a series of alkoxysilanes, the rate of formation of the mesostructured material decreases in the order of TMOS > TEOS > tetrabutyl orthosilicate (TBOS). This is due to the concomitant reduction in the hydrolysis rate of the alkoxysilane precursors as their carbon chain length increases. After cooling to room temperature, the reaction product can be filtered, washed, and dried to yield a mesostructured silica material with the templates inside. Upon removal of the templates, by calcination or solvent extraction, hydrothermally-synthesized mesoporous silica material can be obtained.

Hydrothermal synthesis of highly ordered mesoporous silica is typically carried out in either acidic ($\text{pH} < 6$) or basic ($\text{pH} > 9$) environments under which the rapid controllable polymerization and cross-linking of silicates occur.⁴¹ Generally, the formation of ordered mesostructures near neutral pH is limited; however, addition of fluoride catalysts into the reaction mixture can overcome this limitation and promotes the formation of highly ordered mesoporous solid material even at neutral pH.^{42,43}

A wide array of silica precursors, including silica gels, sodium silicates, silica aerogels and alkoxysilanes (*e.g.*, TEOS), can all be used for the synthesis of mesoporous silica materials in an alkaline environment (pH 9.5-12.5) under hydrothermal conditions. Despite numerous investigations of various silica precursors, it has been demonstrated that TEOS is the most convenient and effective one for laboratory scale syntheses of mesoporous silica materials.^{5,23} To carry out the synthesis in this pH range, various bases, including inorganic bases (*e.g.*, ammonia, sodium and potassium hydroxide) and organic bases (*e.g.*, tetramethylammonium and tetraethylammonium hydroxide), can be used to catalyze the reactions or adjust the pH of the reaction mixtures. However, it is worth noting here that the organic quaternary ammonium bases are typically more expensive while ammonia often leads to poorly ordered mesostructures as a result of its weak alkalinity. It is also noteworthy that pH varies as the reaction proceeds throughout the synthesis with an initial reduction during the hydrolysis step, slightly increasing during the condensation and cross-linking step of silica. High quality MCM-41 can be synthesized by adjusting the pH of the base-catalyzed reaction mixture to the range of 11.0-11.5 with sulfuric or acetic acid during the condensation step of the synthesis.⁸

The discovery of acidic synthetic route for mesoporous silica, by Huo *et al.*,²³ paved the way for a variety of indispensable mesoporous silica materials including SBA-15. The acid-catalyzed synthesis of mesoporous silica materials and the degree of order of their mesostructures have a strong dependence on pH. Although the synthesis proceeds at a faster rate at lower pH values, it is imperative to optimize the effective H^+ concentration in the reaction mixture to obtain a highly ordered mesoporous silica material in the end. In the case of strong acids (*e.g.*, HCl, HBr, HI, HNO₃, H₂SO₄), highly ordered mesoporous materials are observed at pH less than 1, but low-quality products tend to form at extremely high concentrations of acid (*e.g.*, > 4 M HCl). On the other hand, highly ordered SBA-16 materials are favored at low concentrations of HCl (< 0.5 M) as well as in the presence of *n*-butanol as co-solvent, due to the reduced rates of condensation of silicate species in such environments.⁴⁴ Furthermore, the ratio of butanol to silica precursor (*e.g.*, TEOS) is found to dictate the mesophase symmetry, with disordered structures dominating in samples when higher concentrations of both TEOS and butanol are used. At the pH range close to silica's isoelectric point, pH between 1 and 2, the precipitation of silica occurs relatively more slowly.

There are several notable differences between the syntheses of mesoporous silica materials carried out in acidic versus basic conditions. Compared to base-catalyzed synthesis, the acid counterpart facilitates the formation of mesoporous materials with diverse morphologies (*e.g.*, thin films and fibers)⁴⁵ and allows enhanced morphology control as a result of slower polymerization and condensation reactions. Under acidic conditions, the polymerization of silicates is irreversible, which essentially means it leads to the formation of gel, compromising the formation of ordered mesostructures. Also,

unlike base-catalyzed syntheses, in acid-catalyzed synthesis of mesostructured materials, phase transformation seldom occurs; thus, a single type of surfactant template typically results in a material with a single space group with a few exceptions. Further advantages of acidic synthesis include low processing temperature, improvement in the degree of order of the materials simply by incorporation of inorganic salts and without the need of complicated silica sources for the synthesis of the mesoporous materials.⁸

1.3.2. Non-aqueous Synthetic Routes

Besides water, a number of organic solvents have been successfully utilized to synthesize ordered mesoporous materials. Synthesis involving solvents other than water is often referred to as a non-aqueous synthesis. Non-aqueous synthesis is especially a preferred synthetic method when mesoporous materials with unique morphologies (*e.g.*, spheres, thin films, monoliths) are desired. The synthesis is sometimes allowed to proceed through the so-called evaporation-induced self-assembly (EISA) process.⁴⁶ This pathway entails surfactant enrichment above the surfactant's critical micelle concentration (CMC) threshold—which is required for mesophase formation—by preferential evaporation of the organic phase. Typically, in the case of mesostructured film formation using EISA method, TEOS or TMOS is first dissolved in an organic solvent (*e.g.*, ethanol) and allowed to hydrolyze incompletely in the presence of limited amount of water and inorganic acid catalyst. The silica precursor undergoes complete condensation or polymerization while the organic phase is let to gradually evaporate. Evaporation of the organic phase causes an enrichment in the relative concentration of water, HCl, silica, and surfactant in the reaction mixture, thereby gradually increasing the

polymerization rate of silica and facilitating the self-assembly process.⁴⁶ The final polymerization step proceeds very fast, usually taking only a few seconds.⁴⁷

The organic solvents utilized for typical EISA synthesis of mesoporous material are chosen to be weakly polar so that the hydrophobic/hydrophilic properties of the surfactants are significantly reduced and the amphiphilicity of the surfactant is compromised, because both segments can interact with these solvents. Although nonpolar organic phases are generally rarely used in the synthesis of mesoporous materials, their ability to yield interesting mesophase morphologies makes them preferable to use in certain scenarios. For example, through the EISA synthetic approach, mesoporous silica nanowires with tunable dimensions have been synthesized in toluene or xylene solutions in presence of P-123 or F-127 templates.⁴⁸ Similarly, hollow mesoporous spheres have been obtained by adjusting the oil-to-water ratio in the reaction mixture during the synthesis.⁴⁹ The formation of this morphology is attributed to the inverted micelle structure forming in the oil-phase. Using a purely nonpolar solvent induces moisture sensitivity since the presence of water or moisture can have a significant effect on the morphology and the purity of the mesoporous product.

1.3.3. Mesoporous Materials by Post-synthesis

Post-synthesis, which is sometimes called secondary synthesis, involves further modification of as-synthesized mesoporous material *via* hydrothermal treatment, by grafting functional groups on the material's surfaces, or by introducing active functional groups into the pores or on the surfaces of the material. These post-modifications are usually carried out to enhance the physical or thermal stability of the material's

framework as well as to render much desired functionality to the material. Comprehensive reviews of post-synthesis and functionalization of silica can be found elsewhere.^{12,50-53}

Nonetheless, to illustrate the advantages of the post-synthetic modification procedure, a few examples are provided here. For instance, the hydrothermal post-synthetic treatment of mesoporous silica for some 3-7 days at a mild temperature (< 150 °C) improves the structural integrity and induces the phase transformation of the material.⁵⁴ The treatment of MCM-41 with various reagents (*e.g.*, AlCl₃) can increase the mechanical and hydrothermal stability of the material. This phenomenon is attributed to the increase in pore wall thickness, cross-linkages, and modification of weak defect sites in the framework of the material.⁵⁵ Post-synthetic treatment with a number of other reagents is also reported to improve structural ordering and thermal stability of mesoporous materials.^{56,57} Subjecting a mesoporous material to a secondary hydrothermal treatment in presence of ammonia or hydrocarbon analogues thereof has been demonstrated to expand the pores of the materials and improve the materials' stability.^{58,59} Although less common, a recrystallization synthetic technique can be used to improve structural ordering as well as to enlarge the pore dimensions of mesoporous materials.^{30,32} The method also introduces active functional groups into the materials. In another notable work, the Asefa group showed that the treatment of mesoporous silicas with BF₄⁻ species not only enlarges the materials' pores but also introduces fluoro functional groups into the material, making the material to show enhanced catalytic activity in some acid-catalyzed reactions.⁶⁰

1.4. Properties of Mesoporous Materials

1.4.1. Surface Area

Over the past few decades, a considerable amount of effort has been directed toward expanding our understanding of synthesis and characterization of mesostructured materials in order to produce inorganic nanoporous materials that have high surface areas and a broad range of applications. Generally, determination of surface area of such materials is carried out by gas porosimetry and involves methods such as the Brunauer-Emmett-Teller (BET) method,¹⁰ which is a multilayer extension of the Langmuir monolayer adsorption theory.⁶¹ In the laboratory, total BET surface area of mesoporous materials is typically determined from a low temperature (77 K) adsorption-desorption isotherm, obtained by gas porosimetry, using an inert gas (*e.g.*, Ar, N₂) as adsorbent. Furthermore, gas porosimetry provides information about the pore size, pore distribution and pore volume of the mesoporous materials. It is worth adding that, besides inert small gas molecule, others such as benzene, methane, water, etc. can also be used to elucidate various adsorption properties of mesoporous materials, or nanoporous materials in general (see section 1.5.1 for more details).

The surface area, pore morphology, pore wall thickness, etc. of mesoporous materials can be affected by the various synthetic parameters, synthetic conditions, and template removal procedures used to synthesize the materials. For example, by adjusting the hydrophobic chain length of quaternary ammonium bromide surfactants, C_nH_{2n+1}(CH₃)₃NBr, from $n = 8$ to 16, MCM-41 type materials with incrementally higher surface areas, as evidenced by benzene adsorption experiments, can be produced.²¹ Although not fully understood, mesoporous materials synthesized *via* an EISA synthetic

strategy generally exhibit lower surface areas as compared with those synthesized by a hydrothermal synthetic route.⁸ As mesoporous materials with high surface areas are generally expected to find several potential applications, various researchers tried to come up with synthetic methods that lead to such materials. For example, MCM-type materials with surface areas up to $1500 \text{ m}^2 \text{ g}^{-1}$ have been synthesized and investigated for various applications.⁶² It is noteworthy that such large surface area materials can also be used as hard templates for making other high surface area mesoporous materials through the nanocasting processes. In this case, the high surface area and the nanoporous structure of the mesoporous silica material are taken advantage of and then translated into other mesoporous materials (*e.g.*, mesoporous transition metal oxides or mesoporous carbon materials). So, ultimately new mesoporous materials are produced, as the negative replica of the original high surface area mesoporous silica material.

The specific template removal method applied to the surfactant-containing as-synthesized mesostructured material can also affect the surface area of the prepared mesoporous materials. For example, calcination at temperatures above 350 or 550 °C for PEO-PPO-PEO or long-chain alkyl surfactants of SBA-15 type material, respectively, yields materials with relatively lower surface areas, pore volumes and density of surface hydroxyl groups compared with materials obtained with a few other methods.⁸ Tien *et al.* demonstrated that using microwave digestion (MWD) can remove the templates more efficiently and yield SBA-15 type mesoporous material with higher surface area, larger pore volumes, and reduced framework shrinkage as compared to conventional template removal methods involving calcination.⁶³

1.4.2. Pore Properties and Pore Size Distributions

As previously mentioned, it is highly important to be able to control pore size and morphology of mesoporous materials since their adsorption properties as well as many of their potential applications rely heavily on their pore structures. Thus, since the discovery of highly ordered mesoporous silica materials, a great deal of research has focused on the investigation of the underlying mechanisms responsible for controlling pore sizes of these materials.^{8,30,54,64} In the laboratory, the average pores and pore size distributions, which are indispensable structural features of mesostructured materials, are typically determined from N₂ sorption isotherms obtained by gas porosimetry by various methods (typically by the Barret-Joyner-Halenda, BJH) method⁶⁵ (see section 1.5.1 for more details).

The pore size of mesoporous materials, synthesized *via* supramolecular self-assembly synthetic methods, depends predominantly on the hydrophobic region of surfactants employed for the synthesis of the materials as well as the general synthetic methods applied to prepare the materials. A summary of the relationships among structure directing agents, synthetic conditions, and the resulting pore size ranges are listed in Table 1.1. For example, it was demonstrated by Jana *et al.* that when the alkyl chain length increases from C₈ to C₂₂, the BJH pore width of MCM-41 increases from 1.6 to 4.2 nm.⁶⁴ Likewise, Widenmeyer *et al.* showed that the pore sizes of MCM-48 could be systematically adjusted from 1.6 to 3.8 nm by simply changing the alkyl chain length of cationic Gemini surfactant (C_{n-12-n}) templates.⁶⁶ In the case where traditional PEO-PPO-PEO triblock copolymers serve as templates for mesoporous silica materials synthesis, the pore dimensions could be expanded by increasing the molecular weight fraction of the hydrophobic PPO blocks.⁶⁷ It is noteworthy that the spherical micelles

formed from PEO-PO-PEO triblock copolymers are substantially larger in size than those formed from low molecular weight surfactants such as CTAB. Accordingly, the former generally yield mesoporous materials with larger pore dimensions than the latter (see Table 1.1). Adjusting the temperature during hydrothermal synthesis conditions can also affect the pore size of the products.⁶⁸⁻⁷⁰ Moreover, by using organic molecules that can dissolve within and swell the hydrophobic region of a surfactant micelle, the pore dimensions of the mesoporous materials can easily be expanded.^{58,71-73} By using such swelling agents in basic CTAB or acidic triblock copolymer solutions, the pore sizes of the mesoporous materials can be increased to as large as 10 or 40 nm, respectively, although the materials may possess disordered pore structures.⁵⁴ Other inorganic molecules (*e.g.*, supercritical CO₂) have also been used as swelling agents to expand the pores of mesoporous materials.⁷⁴ Using a binary surfactant system as SDA can lead to a mesophase with intermediate pore dimensions as compared with using the individual surfactant as template in the synthesis.⁶⁴

Table 1.1. Pore sizes of ordered mesostructures obtained by various methods.⁸

Pore Size (nm)	Method
2 - 5	Surfactants with different chain lengths including long-chain quaternary cationic salts and neutral organoamines
4 - 7	Long-chain quaternary cationic salts as surfactants high-temperature hydrothermal treatment
5 - 8	Charged surfactants with the addition of organic swelling agents such as TMB and mid-chain amines
2 - 8	Nonionic surfactants
4 - 20	Triblock copolymer surfactants
4 - 11	Secondary synthesis, for example, water-amine postsynthesis
10 - 27	High molecular weight block copolymers, such as PI- <i>b</i> -PEO, PIB- <i>b</i> -PEO and PS- <i>b</i> -PEO triblock copolymers with the addition of swelling agents TMB and inorganic salts low-temperature synthesis

By rational adjustment of synthetic conditions and procedures, homogeneous mesophases with different symmetries, and more importantly, different pore structures can be synthesized.⁵⁴ A detailed discussion of the types of mesophase symmetries and their respective syntheses is described elsewhere.⁸

1.4.3. Crystallinity

Crystallinity can be defined as the degree of long-range structural order comprising a crystal lattice within a (solid) material. The crystal lattice can extend in three directions or limited to just one, and it is a key parameter that can determine the physical and chemical properties of many solid-state materials. The advent of highly ordered mesoporous silica quickly initiated a debate on the crystallinity of the SiO₂ pore walls of the materials. Although not conclusive, ²⁹Si nuclear magnetic resonance (NMR) experiments suggested that mesoporous MCM-41 possessed a disordered wall structure.¹⁵ Direct evidence of amorphous pore walls within the mesostructures emerged later during Raman analysis of MCM-41 samples.⁷⁵ The dehydrated samples of mesoporous silica exhibited planar three-membered ring stretch Raman vibrations, which are clearly different from crystalline materials comprising three-membered rings in which this vibration is not observed.^{76,77} The amorphous nature of the material suggests that a variety of synthetic techniques can be implemented to achieve parity mesostructures.

A major breakthrough in the synthesis of mesoporous materials with crystalline pore walls emerged from the report by Inagaki *et al.* describing the surfactant-directed synthesis of an ordered mesoporous benzene-silica (a hybrid organosilica) material with crystal-like pore walls, as a result of the ordered arrangement of the organic groups in the

framework of the material.⁷⁸ So, any success in the development of a purely inorganic mesoporous silica with crystalline pore walls in the future would certainly be a major development and may constitute a cascade of improvements in the properties as well as potential applications of mesoporous materials in the future.

1.5. General Characterization Methods of Mesoporous Material

As discussed above, supramolecular synthetic methods leading to mesoporous materials have advanced tremendously over the past 30 years. It is now possible to make many of them with different pore sizes and compositions as well as chemical, physical and surface properties. Meanwhile, the development and/or availability of various powerful state-of-the-art characterization instruments for mesoporous materials, or nanomaterials in general, have made observations and analysis of the structures and properties of such materials easier, while also making further adjustments in the synthesis to produce mesoporous materials with more complex structures to be increasingly possible.

In this section, the general and widely used analytical instruments and methods for characterization of mesoporous materials and the kinds of information they can provide are discussed. Like in many solid-state materials, the characterizations of mesoporous materials are generally carried out in order to obtain three types of information about the materials: structural information, compositional information, and inherent materials property (surface, dielectric, mechanical, conductivity, etc.). The structural analyses of the materials are performed mainly by gas porosimetry, powder X-ray diffraction (PXRD), and transmission electron microscopy (TEM). Compositional

studies are often carried out by methods such as solid-state NMR, Fourier transform infrared (FTIR), and X-ray photoelectron spectroscopy (XPS), and also elemental (EA) and thermogravimetric analyses (TGA). The properties of mesoporous materials, which include hydrophobic, hydrophilic, electronic, conductivity, mechanical, and dielectric properties, are determined by N₂ porosimetry, UV-Vis spectroscopy, nanoindentation, etc. In many instances, many of these techniques have to be used in complimentary ways to get the full picture of the mesoporous materials. Some of these techniques are discussed further below.

1.5.1. Gas Porosimetry

As mentioned in several sections above, one of the most important structural features of mesoporous materials is their nanoporous structures, nanometer pores and high surface areas. These structural features also largely dictate the properties and potential applications of the materials in areas including catalysis, chromatography, and separations. Thus, they are among the structural features of mesoporous materials that are investigated first or have to be probed. This is done with gas porosimetry, which involves gas or liquid adsorption techniques, particularly using N₂ as the adsorbate (or N₂ adsorption technique).⁸⁰

Gas adsorption starts with the treatment of the sample at high enough temperature, under vacuum, to remove physisorbed species (*e.g.*, surface adsorbed water) from the material, and then slowly purging the sample with the probe molecules (*e.g.*, N₂). The amount of gas adsorbed by the sample at different relative pressures of the gas is measured. This is followed by the reverse process, called desorption, where the adsorbed

molecules are let to come off by slowly lowering the relative pressure. From the resulting plot of adsorption-desorption quantities versus relative pressure, also called isotherm, and by applying equations such as the BET on the monolayer adsorption part of the data, the surface areas of the materials can be determined. The total pore volumes of the mesoporous materials are determined by converting the quantity of gas adsorbed in the materials at the saturation pressure to the corresponding volume of that gas at the temperature used during the measurement, which is typically 77 K for N₂ porosimetry. The pore size distributions and the average pore size of the material can also be determined by applying various methods/equations on the data obtained. To determine the pore sizes of mesoporous materials, methods such as BJH method, Kruk-Jaroniec-Sayari (KJS) method, etc.⁸¹⁻⁸³ are commonly applied. The average pore diameter (w) of the materials is often determined by plugging the pore volumes and d -spacing values of mesoporous materials in the following equation, Equation 1.1:

$$w = cd_{100} \left(\frac{V_p \rho}{1 + V_p \rho} \right)^{1/2} \quad (\text{Equation 1.1})$$

where c has a value of 1.213 for cylindrical pore geometry, V_p is the pore volume, ρ is the pore wall density of the mesoporous material and d_{100} corresponds to the interplanar spacing of the (100) planes, which can be determined with small angle powder X-ray diffraction (PXRD) or small angle X-ray scattering (SAXS) techniques (see section 1.5.2) or imaging techniques such as transmission electron microscopy (TEM) (see section 1.5.3). Alternatively, w can be determined by using an equation $w = 4(V_p/S)$ where S is the surface area.⁹⁰ V_p can be determined from the BJH cumulative volume of the pores,

for pores ranging from 1.7-30.0 nm in either the adsorption or desorption branch of the gas sorption isotherm data for the material, and S is the surface area of the material.

1.5.2. Small Angle Powder X-ray Diffraction (PXRD) and Small Angle X-ray Scattering (SAXS)

As previously discussed, MCM-41, SBA-15 type, and several other mesoporous silica materials have highly ordered mesopore structures. For example, MCM-41 and SBA-15 materials have highly ordered hexagonal ($P6mm$) mesoporous structures. These structural features of mesoporous materials are typically determined using PXRD or SAXS techniques. Furthermore, PXRD allows the determination of the values of interplanar spacings (*i.e.*, d -spacing) of the ordered pore structure. This, in combination with the pore size results, obtained from gas adsorption results, enables the determination of the wall thickness of an ordered mesoporous material.

The X-ray diffraction (XRD) patterns or small angle X-ray scattering (SAXS) results are obtained by using X-ray diffractometers or SAXS instruments.⁸⁴ In these instruments, typically a mesoporous sample is bombarded with X-ray beams, and the X-ray beams diffract (or scatter) and give some diffraction (or scattering) patterns if the sample has some ordered arrangement of pores, groups, etc. The diffraction patterns occur at specific orientations, where in-phase or constructive interferences of the atoms or pore structures of mesoporous materials exist. From the patterns, the degree of long-range atomic or structural ordering, their d -spacings, and other important structural features about the material can then be discerned. If the material does not exhibit any ordered or crystalline features (*e.g.*, atomic arrangement and pore networks), no (or very

broad) diffraction pattern is obtained instead. Moreover, if the ordered mesoporous material is built from some crystalline particles, the size of crystalline domains can be determined from the degree of peak broadening according to the Scherrer equation.⁸⁵

1.5.3. Transmission Electron Microscopy (TEM)

TEM is among the techniques chosen for the analysis of mesoporous materials because it can quickly provide many kinds of useful information about mesoporous materials and because it involves simple sample preparations. The sample preparation merely involves spreading of a small amount of sample (either from a dried powdered material or from a solution/suspension) as a thin layer onto a copper, carbon-coated, or other types of TEM grids. The samples are then exposed to a beam of high-energy electrons, and electron scattering occurs in areas of higher electron density and low or no scattering results in the regions of the sample possessing low electron density. Based on the difference in the region where the light passes through and hitting a fluorescent screen on the detector, combined with the region where the light is scattered, using a series of electromagnetic lenses, two dimensional images corresponding to the structure of the mesoporous materials is obtained. Images at the nanometer scale, with resolutions as low as 0.05 nm or sub-nm, can now be routinely obtained using high-resolution TEM (HRTEM) instruments. Furthermore, with the recent developments of 3-dimensional imaging or tomography techniques, 3-dimensional imaging of mesoporous structure, which was not possible before, is now routinely attainable.

TEM analysis can provide important structural information about mesoporous materials. First, it can inform about how ordered the structure of the materials is, and if

so, the degree of the long-range order of the structure of the materials. Second, it provides data about the pore diameter and wall thickness of the mesoporous materials. It is also used in complimentary ways with XRD, SAXS and gas sorption analyses, supporting or refining the results obtained by the other methods. Third, it helps with the determination of the particle sizes of the mesoporous materials and their overall morphology. These properties are of great importance especially for applications relying on the transport of fluids in the structures of the materials, such as chromatography and drug delivery, and for applications relying on the ability of the materials penetrating tissues and cells. TEM is also helpful to analyze any possible changes (*e.g.*, framework collapse) that the materials may have undergone during some chemical processes; this is done by taking images of the samples before and after the chemical processes and comparing them. TEM may also be equipped with energy-dispersive X-ray (EDX) spectroscopy to provide elemental analysis on the obtained images.

1.5.4. Nuclear Magnetic Resonance (NMR) Spectroscopy

Solid-state NMR is a very useful technique for characterization of various mesoporous materials that have NMR active species.^{86,87} For mesoporous silica materials, for instance, the technique can provide information about the degree of condensation of the silica framework, the amount of surface uncondensed hydroxyl groups, etc. For mesoporous materials containing organic groups, either as grafted moieties on the surfaces of the materials or as condensed forms within the framework of the materials, the type and relative amount of organic groups can also be determined with solid-state NMR spectroscopy. For materials containing other NMR active species within the pores

or on the surfaces of the mesoporous materials, the species can be qualitatively and quantitatively elucidated by solid-state NMR techniques as well.

Solid-state NMR characterization of (mesoporous) materials became widely applicable and useful especially after the advent of the so-called magic angle spinning (MAS) technique. In typical solid-state NMR analysis, the sample is placed in a small rotor, usually made of partially stabilized zirconia (PSZ) or silicon nitride, and are spun rapidly about a specific axis and at a specific angle called the magic angle ($\theta = 54.74^\circ$) with respect to the magnetic field. This spinning efficiently averages out spin interactions, reduces line broadenings, and gives spectra with enhanced signal-to-noise ratio. The MAS techniques can further be coupled/decoupled with cross polarization (CP) techniques, where heteronuclear interactions such as $H \rightarrow Si$ or $H \rightarrow C$ are coupled or decoupled to differentiate specific species (*e.g.*, silicate or hydrocarbon species in mesoporous materials) and their chemical environments. Also, heteronuclear interactions such as $H \rightarrow Si$ or $H \rightarrow C$ are coupled in order to improve the signals of the ^{29}Si and ^{13}C nuclei in the mesoporous silica or organosilica materials, which normally give weak signals due to their low natural nuclear abundance. For example, with 1H - ^{29}Si cross polarization (CP) MAS, silicate species near hydrogen atoms in the material (*e.g.*, silanols in mesoporous silica or organosilica) are observable, whereas fully condensed silicates that are not near surface silanols are not. Although this improves the signals of certain species, and enables their characterizations, which are otherwise difficult to probe, it may not provide quantitative information, because it favors one type of species over another. For example, in the case of mesoporous silica materials, the $(SiO)_2\text{Si}(\underline{Si})(OH)_2$ (Q^2) as well as $(SiO)_3\text{Si}(\underline{Si})(OH)$ (Q^3) Si species are favored and give stronger signals than the

(SiO)₄Si (Q⁴) Si species. This means the ultimate result does not reflect the actual composition of the material, and is only of qualitative value. The same coupling and decoupling techniques can also be applied to other types of mesoporous materials that have NMR active species (*e.g.*, ²⁷Al in mesoporous alumina or aluminosilicates).

On the other hand, a high-powered (HP) MAS solid-state NMR technique can be employed to get quantitative results. In HP-MAS analysis of mesoporous silica, the signals from ¹H are decoupled and all silicates species present in the material are seen or give signals that commensurate their amount in the sample. Despite its ability to provide such useful quantitative information about mesoporous materials, the extended spin-lattice relaxation times necessary for HP-MAS experiments, coupled with low concentrations of some NMR-active species in the materials, may sometimes limit the ability of this technique. The longer recycle delays due to extended spin-lattice relaxation times, plus the absence of signal enhancement by cross-coupling, also make HP-MAS experiments to generally require more scans and take longer time to obtain spectra with good enough signal-to-noise ratios. The common silicate species that can be present in mesoporous silica and organosilica materials, with their approximate ²⁹Si chemical shifts, are listed in Table 1.2. In addition to Q species, T¹, T⁰, D⁰, and M⁰ species may also exist in solid-state NMR spectra of organic-functionalized mesoporous silica and periodic mesoporous organosilica (PMO) materials. So, the technique may also allow characterization of the presence and the relative density of organic or other functional groups in the mesoporous materials.

Table 1.2. Common silicate species of mesoporous silica materials and their respective positions in ^{29}Si spectra.

Possible Silicate Species on Mesoporous Silicas and Organosilicas	Nomenclature	Approximate Chemical Shift Positions (ppm) ^a
$(\text{SiO})_4\text{Si}$	Q^4	-110
$(\text{SiO})_3\text{SiOH}$	Q^3	-100
$(\text{SiO})_2\text{Si}(\text{OH})_2$	Q^2	-91
$(\text{SiO})_3\text{SiR}'$	T^3	-65 to -90
$(\text{SiO})_2\text{Si}(\text{OR})\text{R}'$	T^2	-57 to -72
$(\text{SiO})_2\text{SiR}_2$	D^2	-22
$(\text{SiO})_2\text{Si}(\text{OR})_1\text{R}_2'$	D^1	-13
$(\text{SiO})_1\text{SiR}_3$	M^1	11

^a The exact region may vary depending on the exact organic groups or other species present in the materials (*e.g.*, if R is alkyl or vinylic group). The numbers are only approximate regions generally expected for such species.

1.5.5. Thermogravimetric Analysis (TGA)

TGA is generally useful for the characterization of mesoporous materials containing thermally decomposable species, which come off as the material is heated at different temperatures. In such materials, TGA is used to generate a thermal decomposition profile of the material by measuring the weight loss (%) as a function of temperature change. The TGA experiments of mesoporous materials are generally carried out in a temperature range between room temperature to around 800 °C in different atmospheres (*e.g.*, air, N_2 , Ar), and the weight loss, in percent, is plotted as a function of

temperature for subsequent data interpretation. The results provide information about the presence and the relative amount of different species such as water and surface hydroxyl groups and other species such as organic groups in the materials. The results can also provide information about the thermal stability of the different groups in the mesoporous materials (*e.g.*, organic groups in multifunctional mesoporous organosilicas) at higher temperatures. In combination with mass spectrometry, TGA can provide more information on the exact species coming off from the high temperature decomposition of the mesoporous materials. TGA may have one major weakness though: in cases where decomposition temperatures of the different groups overlap, it is difficult to precisely determine the type and the relative amount of the different species present in the material.

The information provided by TGA is generally used to supplement other compositional information obtained by studies involving solid-state NMR, X-ray photoelectron spectroscopy (XPS) (see section 1.5.6 below), and elemental analyses (obtained by inductively coupled plasma - optical emission spectroscopy (ICP-OES) or inductively coupled plasma - mass spectroscopy (ICP-MS), CHN combustion, or EDX, etc.).

1.5.6. X-ray Photoelectron Spectroscopy (XPS)

XPS, also called Electron Spectroscopy for Chemical Analysis (ESCA), is a technique that allows analysis of the compositions of mesoporous materials based on the electronic state of the species present in the materials.^{88,89} This technique utilizes photoelectrons emitted from the elements within the mesoporous sample upon illumination with X-ray beams with a specific energy (in eV) under extremely high

vacuum. The absorption of X-ray photons by the sample leads to ionization and emission of inner shell electrons, whose energy is then measured by an electron-energy analyzer and compiled in a photoelectron spectrum, usually in the range of 0 – 1400 eV. From the energy profile, the kind of elements or molecular species present in the materials is deduced.

The technique allows the determination of possible changes that functional groups may undergo during chemical conversions (*e.g.*, changes in oxidation states during catalysis). This method is especially powerful in combination of FTIR and solid-state NMR techniques and may allow the full elucidation of the compositions and the different groups present in the mesoporous materials. However, since XPS is typically a surface analytical technique as X-rays penetrate only to a certain depth of the sample (*ca.* < 20 nm), the technique is most suited for analysis of the upper most layers of materials and is thus especially useful for thin film type mesoporous materials. Despite this, XPS can still be successfully used for analysis of the bulk composition of mesoporous materials if it is coupled with other surface etching techniques.

1.5.7. Fourier Transform Infrared (FTIR) Spectroscopy

In FTIR spectroscopy of mesoporous materials, a sample is exposed to a beam of infrared (IR) light with energy in the range of 200 - 4,000 cm^{-1} . The molecules or chemical species present in the mesoporous material may be excited by specific wavelengths of the IR light, concomitant to the vibrational excitation energy that the covalent bonds in the material require to undergo stretching, wagging, etc. This results in the absorbance of a specific series of wavelengths of IR light, which can be measured and

plotted. By comparing the peaks with tabulated peaks of known compounds and species, the different chemical species present in the mesoporous material can be determined. The use of FTIR spectroscopy in the compositional analysis of functionalized mesoporous silica materials does have certain limitations though. For example, the characteristic absorptions at around 3400-3600, 1050, 950 and 790 cm^{-1} , corresponding to Si-OH stretching, Si-O-Si asymmetric stretching, Si-OH stretching, Si-O-Si bending modes, respectively, may overlap amongst each other and with other functional groups that may be present in the mesoporous materials. This may make characterization of these different groups in such materials difficult. Nevertheless, FTIR spectroscopy, in combination with the other analytical techniques discussed above, is still helpful for compositional analyses of mesoporous materials and/or, in some cases, the specific functional groups present.

1.6. Applications of Mesoporous Materials

Because of their nanostructures, nanometer pores and high surface area, mesoporous materials have found a range of potential applications in areas such as drug delivery, catalysis, nanoelectronics, environmental remediation, chromatography, and separations.^{15-19,79,90,104-119} By further design and modification of their surfaces with various functional groups, mesoporous materials, that can serve as high adsorption capacity host materials for drugs, as controlled drug-delivery systems, for making biosensors, and as microfluidic bioseparation media can be produced.

1.6.1. Biological and Drug Delivery Applications

Many conventional drugs cause various unwanted side effects for different reasons. For instance, as the drugs administered by conventional means travels toward the

desired sites, they sometimes meet physiological obstacles or harm normal cells and tissues. Furthermore, the amount of drug that actually reaches to the desired sites may be less than what is administered. This inability of the drug to maintain therapeutic dosage to the targeted cells or tissues can lead to a decrease in the efficacy of the drug. So, the development of controlled drug-delivery systems that deliver the desired therapeutic dosage of the drug to the desired sites is important in the ongoing efforts to improve human health. By designing controlled drug release systems, the specificity of the drug can also be improved, and many adverse reactions of conventional drugs can be minimized. Through rational design and synthesis of novel nanomaterials with “smart” structures and functions, efficient drug-delivery is possible (Figure 1.5).⁹¹ Nanomaterials are also potentially capable of delivering drugs to areas of the body that are otherwise inaccessible, prevent the body’s normal defenses from interfering before the drugs reach their targets, reduce the chance that healthy tissues to be damaged, allow biodiagnosis of tissues, and minimize adverse reactions that lead to unwanted side effects.⁹²

Owing to their large surface area, tunable pore volume, and very easily modifiable surfaces, mesoporous nanomaterials were identified as potential drug delivery vehicles for biological and medical applications. Furthermore, since their surface can easily be functionalized by various functional groups, they are proven to be quite versatile for various biological applications. Mesoporous materials are ideal for many biological applications, mainly also because they can adsorb and release bioactive agents. By synthesizing functionalized mesoporous materials it is possible to control the adsorption and release of bioactive molecules.

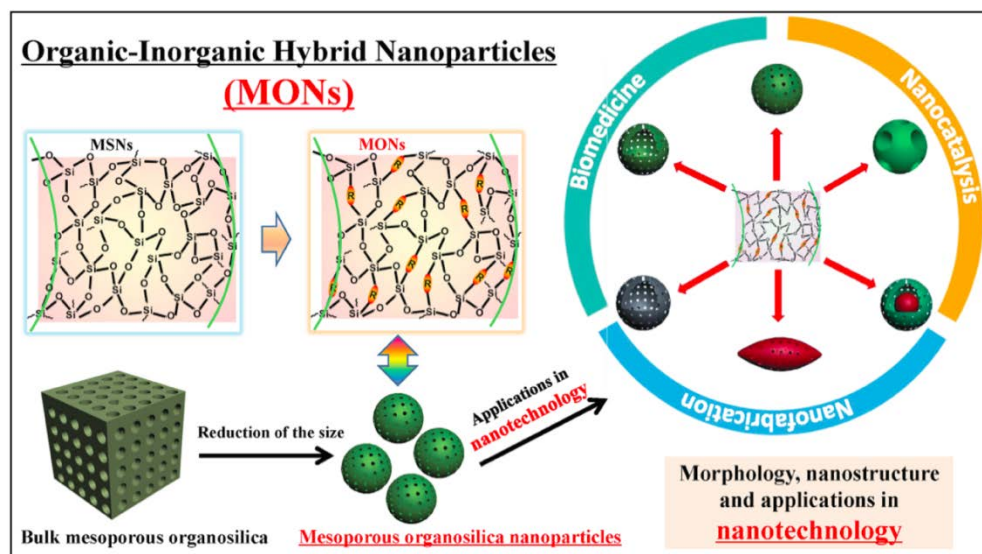


Figure 1.5. Schematic illustration of the framework-composition alteration from traditional inorganic -Si-O-Si- (mesoporous silica nanoparticles or MSNs) to organic-inorganic hybrid -Si-R-Si- (mesoporous organosilica nanoparticles or MONs), transformation of bulk mesoporous organosilica (e.g., periodic mesoporous organosilicas or PMOs) into mesoporous organosilica nanoparticles of MONs, and their representative morphologies, nanostructures and applications in nanotechnology. Reprinted from Chen, Y.; Shi, J. *Adv. Mater.* **2016**, 28, 3235–3272, Copyright (2016), with permission from Wiley VCH.

The initial report of mesoporous silica as a drug delivery system demonstrated the loading of a high payload of ibuprofen in the void spaces of mesoporous $\text{C}_{12-16}\text{TAB}$ -templated MCM-41 and the release of the drug in simulated body fluid (SBF). This material was proven to exhibit the desirable properties of uniform porosity, high surface area, robust host framework, and tunable dimensions to facilitate sustained drug release. Additionally, although *in vivo* biocompatibility remains a matter of scientific debate,

forms of mesoporous silica materials have been shown to be nontoxic when administered at the right dosage.⁹³

Another beneficial property of mesoporous silica materials is that their surfaces can be modified with various functional and bioactive groups, as discussed and shown in Figure 1.5 above. Besides helping control adsorption and release of molecules, the functional groups can dictate the materials' interactions with biological surfaces and help the materials to target specific sites and deliver the bioactive guest molecules specifically to those sites. Moreover, since their pores can be tailored, the loading as well as release of molecules can also be judiciously controlled. Normally, the pore selectivity can be dictated by the pore shape, size and covalent interactions that may take place between the functional groups on the pore surfaces and the bioactive molecules. By partially replacing the silica precursor (tetraethyl orthosilicate, TEOS) with organosilanes (Figure 1.5), it is possible to increase secondary non-covalent interactions such as hydrophobicity and hydrophilicity and further tailor the gate-keeping properties of the pores. Functionalization of mesoporous materials also helps many hydrophobic or hydrophilic or both types of bioactive agents to be introduced as guest species within the mesoporous materials, and be successively delivered or co-delivered.⁹⁴ Because of their larger (particle) sizes compared with small molecule drugs, mesoporous silica nanomaterials may also have an added advantage of long circulations times in the body and thereby be able to passively make it through the permeable tissues of cancerous tumor sites better, along with the payloads of drugs they carry. Furthermore, with the right photoactive functional groups, functionalized mesoporous silica nanomaterials can also be potentially useful for photodynamic therapy (PDT) of cancer, as illustrated in Figures 1.1.⁹⁵

Although mesoporous silica nanomaterials are entering into clinical studies only recently, their potential applications as efficient delivery systems for a variety of important drug molecules (*e.g.*, cisplatin, neurotransmitters, insulin) to desired intracellular sites for treatment of cancer, diabetes, etc. have been well demonstrated over the past 15 years. The biological and biomedical applications of silica nanomaterials are not restricted only to drug delivery though. There have also been hundreds of examples where mesoporous materials have been shown to serve as bioimaging, biodiagnostic and biosensing agents.

The advantages of leveraging mesoporous silica as a host for drug delivery include well-ordered uniform porosity with tunable dimensions, facile functionalization of pore openings or cavities *via* grafting of their surface silanol groups, high pore volume available for guest molecules, and high surface area to facilitate drug adsorption. Since drug loading is usually carried out *via* physical adsorption of highly concentrated drug solutions onto mesoporous framework, the limitation for efficient drug loading is the relative size of the pore openings and pore sizes to the drug molecules. The ability to systematically adjust pore size in the range of 1.5 to 30 nm suggests these materials can effectively host a wide array of small molecules or macromolecules (*e.g.*, proteins). For example, early adsorption studies by Hata *et al.*⁹⁶ of an antitumor agent (*i.e.*, Taxol) onto FSM-type mesoporous silica demonstrated that the drug only adsorbs within the channel pores of the material if its pore size is larger than 1.8 nm. A significant dependence of adsorption on solvent was additionally reported since physisorption was not observed in methanol or acetone environments. Besides restricting the size of guest molecules suitable for adsorption, pore size has a substantial effect on the rates of drug release from

these materials. In fact, a correlation between pore size and release rate of ibuprofen from various mesoporous materials has been documented (*e.g.*, C₈₋₁₆TAB templated MCM-41 as seen in Figure 1.6).⁹⁷ Besides confirming the same trend, studies conducted with cubic (*Ia3d*) mesoporous silica suggested the relationship between pore size and drug release rate is an inherent property of mesoporous solids.⁹⁸ Other studies focused on the relationship of pore morphology with drug release rate.⁹⁹ Additionally, pore volume can be a key parameter in the loading and the release rate of drugs from the materials. Assuming that a drug is small enough to enter the pores of mesoporous materials, the presence of drug-drug interactions may cause pore filling. In this case, the pore volume of the material dictates the maximum drug loading capacity.

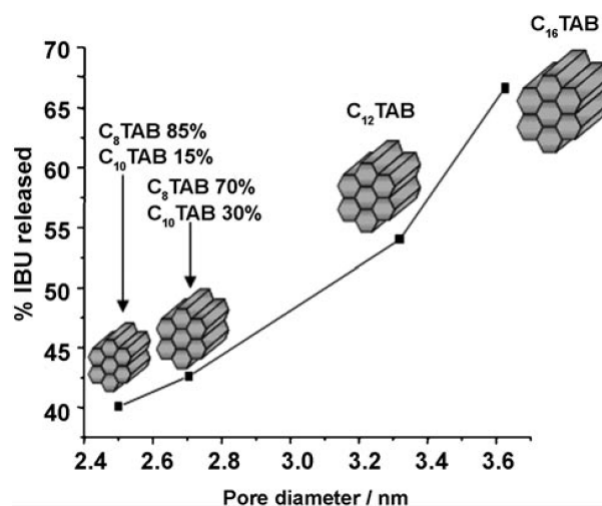


Figure 1.6. Fraction of ibuprofen released from ibuprofen-loaded MCM-41 after 24 h in simulated body fluid (SBF). Reprinted from Vallet-Regi, M.; Balas, F.; Arcos, D., *Angew. Chem. Int. Ed.* **2007**, 46, 7548–7558, Copyright (2007), with permission from Wiley VCH.

Efficacious drug loading and subsequent controlled-release requires adequate interaction between the surfaces of the mesoporous materials and the drug molecules. Therefore, the surface area of the materials available for physisorption is often the dominating factor dictating the maximum drug loading capacity and release kinetics. Assuming the host material has pore networks and pores with appropriate size to allow the entrance of guest molecules, increase in surface area typically results in higher drug loading capacity.¹⁰⁰ Another versatile technique to improve drug loading capacity and controlled release rate involves the modification of the pore surface *via* grafting using various functionalized alkoxysilane precursors. A comprehensive review for functionalization of mesoporous silica materials for controlled drug delivery can be found elsewhere.¹²

One of the most convenient and most commonly used approaches to equip mesoporous silica nanomaterials with guest molecules for biological and medical applications is by functionalizing their otherwise ‘unfunctionalized’ surfaces with organic groups. There are numerous examples in the literature now on the synthesis of such organic-modified silica nanomaterials and their use for controlled drug delivery and many other biological/medical applications.^{14,101} This chemical modification with organic groups allows the materials to interact better with the drug molecules, making the materials to demonstrate high adsorption capacity for drugs. The resulting materials may have an increase in secondary non-covalent interactions with the bioactive and drug molecules. This approach is important due to the hydrophobic nature of many bioactive materials and drugs, which suffer from poor bioviability as a result. An increased interaction of the drug within the host materials can also lead to better stability for the

drug and its more homogeneous, slow, or controlled release over longer times. The surface modification can also improve the biocompatibility of the mesoporous materials or enable the materials to target only specific cells within the body and deliver the drugs only to those targeted cells.^{102,103}

In order for mesoporous materials and their organic-modified counterparts to find applications in nanomedicine, their biocompatibility has to be fully and extensively examined. Numerous studies on the biocompatibility of mesoporous silica-based nanomaterials have already been conducted,³³⁻³⁷ and numerous important facts on the biological effects and biocompatibility/cytotoxicity of several mesoporous materials have already been documented. However, in some cases conflicting reports have also been reported for many of the materials.⁹³ Consequently, the possible clinical trials of these interesting materials are still in their infancy and may need additional studies beforehand.

1.7. Summary and Future Prospects

Over the last decade, there has been increasing interest and research effort in the synthesis, characterization, functionalization, molecular modeling and design and synthesis of various nanoporous materials. Because of their high surface area, large pore volume and nanometer pores, it did not take long for researchers to start investigating and to realize the potential uses of these materials (*e.g.*, as host materials for various types of guest molecules and for biological applications). As a specific example, the interaction of surface hydroxyl groups of these materials with many types of guest molecules *via* hydrogen bonding has been exploited to adsorb and release active molecules (*e.g.*, the anticancer drugs doxorubicin and cisplatin). Furthermore, the hydroxyl groups (*e.g.*,

surface silanols in case mesoporous silicas) on the pore walls as well as the external surfaces of these materials have been successfully taken advantage of to tether a variety of functional groups, including catalytic active acidic, basic, and organometallic complexes; cell targeting proteins and small molecules (*e.g.*, folic acid groups that can target folate receptors on cancer cells); etc. These processes generally substantially expanded the properties as well as the potential applications of these materials.

Some of the most notable synthetic strategies and the most notable materials and their properties have been described. The many potential biological applications of these materials in different areas have also been highlighted. In some cases, the manner by which rational design and synthetic approaches generates highly active heterogeneous catalysts have been emphasized. In addition, since the surface silanols themselves are intrinsically weak acid groups, specific examples highlighting their additional uses as co-catalysts in some reactions have been discussed.

Although many major developments have undoubtedly been made in the field of mesoporous materials since their inception, challenges remain to produce materials with tunable monodisperse and robust pore structures, crystalline frameworks, stable structures under various conditions, non-toxic to use in nanomedical and environmental applications. Furthermore, despite the great strides made thus far, more efforts, especially on the rational design and synthetic approaches for more advanced, multifunctional and smart mesoporous nanomaterials with multiple useful properties still remain and may be among the most important topics in the field yet to be explored further.

1.8. References

- (1) Chen, Y.; Meng, Q.; Wu, M.; Wang, S.; Xu, P.; Chen, H.; Li, Y.; Zhang, L.; Wang, L.; Shi, J., Hollow mesoporous organosilica nanoparticles: A generic intelligent framework-hybridization approach for biomedicine. *J. Am. Chem. Soc.* **2014**, *136* (46), 16326-16334.
- (2) Copéret, C.; Comas-Vives, A.; Conley, M. P.; Estes, D. P.; Fedorov, A.; Mougél, V.; Nagae, H.; Núñez-Zarur, F.; Zhizhko, P. A., Surface organometallic and coordination chemistry toward single-site heterogeneous catalysts: Strategies, methods, structures, and activities. *Chem. Rev.* **2016**, *116* (2), 323-421.
- (3) Feng, X.; Fryxell, G. E.; Wang, L.-Q.; Kim, A. Y.; Liu, J.; Kemner, K. M., Functionalized monolayers on ordered mesoporous supports. *Science* **1997**, *276* (5314), 923-926.
- (4) Yanagisawa, T. S., T.; Kuroda, K.; Kato, C., The preparation of alkyltrimethylammonium-kanemite complexes and their conversion to microporous materials. *Bull. Chem. Soc. Jpn.* **1990**, *63* (4), 988-992.
- (5) Kresge, C. T.; Leonowicz, M. E.; Roth, W. J.; Vartuli, J. C.; Beck, J. S., Ordered mesoporous molecular sieves synthesized by a liquid-crystal template mechanism. *Nature* **1992**, *359* (6397), 710-712.
- (6) Zhao, D.; Feng, J.; Huo, Q.; Melosh, N.; Fredrickson, G. H.; Chmelka, B. F.; Stucky, G. D., Triblock copolymer syntheses of mesoporous silica with periodic 50 to 300 angstrom pores. *Science* **1998**, *279* (5350), 548-52.
- (7) Baerlocher, C.; McCusker, L. B.; Olson, D. H., *Atlas of zeolite framework types*. 6th ed.; Elsevier: 2007.
- (8) Wan, Y.; Zhao, On the controllable soft-templating approach to mesoporous silicates. *Chem. Rev.* **2007**, *107* (7), 2821-2860.
- (9) Karge, H. G.; Weitkamp, J., *Molecular Sieves*. Springer: 1998; Vol. 3.
- (10) Brunauer, S.; Emmett, P. H.; Teller, E., Adsorption of gases in multimolecular layers. *J. Am. Chem. Soc.* **1938**, *60* (2), 309-319.
- (11) Corma, A., From microporous to mesoporous molecular sieve materials and their use in catalysis. *Chem. Rev.* **1997**, *97* (6), 2373-2420.
- (12) Yang, P.; Gai, S.; Lin, J., Functionalized mesoporous silica materials for controlled drug delivery. *Chem. Soc. Rev.* **2012**, *41* (9), 3679-98.
- (13) Slowing, II; Vivero-Escoto, J. L.; Wu, C. W.; Lin, V. S., Mesoporous silica nanoparticles as controlled release drug delivery and gene transfection carriers. *Adv. Drug Deliv. Rev.* **2008**, *60* (11), 1278-88.
- (14) Asefa, T.; Tao, Z., Mesoporous silica and organosilica materials — Review of their synthesis and organic functionalization. *Can. J. Chem.* **2012**, *90* (12), 1015-1031.
- (15) Davis, M. E., Ordered porous materials for emerging applications. *Nature* **2002**, *417* (6891), 813-821.
- (16) Chew, T. L.; Ahmad, A. L.; Bhatia, S., Ordered mesoporous silica (OMS) as an adsorbent and membrane for separation of carbon dioxide (CO₂). *Adv. Colloid Interface Sci.* **2010**, *153* (1-2), 43-57.

- (17) Zhao, J.; Gao, F.; Fu, Y.; Jin, W.; Yang, P.; Zhao, D., Biomolecule separation using large pore mesoporous SBA-15 as a substrate in high performance liquid chromatography. *Chem. Comm.* **2002**, (7), 752-753.
- (18) Han, Y.-J.; Stucky, G. D.; Butler, A., Mesoporous silicate sequestration and release of proteins. *J. Am. Chem. Soc.* **1999**, *121* (42), 9897-9898.
- (19) Raimondo, M.; Perez, G.; Sinibaldi, M.; De Stefanis, A.; A. G. Tomlinson, A., Mesoporous M41S materials in capillary gas chromatography. *Chem. Comm.* **1997**, (15), 1343-1344.
- (20) Hoffmann, F.; Cornelius, M.; Morell, J.; Froba, M., Silica-based mesoporous organic-inorganic hybrid materials. *Angew. Chem., Int. Ed.* **2006**, *45* (20), 3216-51.
- (21) Beck, J. S.; Vartuli, J. C.; Roth, W. J.; Leonowicz, M. E.; Kresge, C. T.; Schmitt, K. D.; Chu, C. T. W.; Olson, D. H.; Sheppard, E. W.; McCullen, S. B.; Higgins, J. B.; Schlenker, J. L., A new family of mesoporous molecular sieves prepared with liquid crystal templates. *J. Am. Chem. Soc.* **1992**, *114* (27), 10834-10843.
- (22) Ciesla, U.; Demuth, D.; Leon, R.; Petroff, P.; Stucky, G.; Unger, K.; Schuth, F., Surfactant controlled preparation of mesostructured transition-metal oxide compounds. *J. Chem. Soc., Chem. Commun.* **1994**, (11), 1387-1388.
- (23) Huo, Q.; Margolese, D. I.; Ciesla, U.; Feng, P.; Gier, T. E.; Sieger, P.; Leon, R.; Petroff, P. M.; Schuth, F.; Stucky, G. D., Generalized synthesis of periodic surfactant/inorganic composite materials. *Nature* **1994**, *368* (6469), 317-321.
- (24) Tanev, P. T.; Pinnavaia, T. J., A neutral templating route to mesoporous molecular sieves. *Science* **1995**, *267* (5199), 865-7.
- (25) Bagshaw, S. A.; Prouzet, E.; Pinnavaia, T. J., Templating of mesoporous molecular sieves by nonionic polyethylene oxide surfactants. *Science* **1995**, *269* (5228), 1242-4.
- (26) Antonelli, D. M.; Ying, J. Y., Synthesis of a stable hexagonally packed mesoporous niobium oxide molecular sieve through a novel ligand-assisted templating mechanism. *Angew. Chem., Int. Ed.* **1996**, *35* (4), 426-430.
- (27) Zhao, D.; Goldfarb, D., Synthesis of lamellar mesostructures with nonamphiphilic mesogens as templates. *Chem. Mater.* **1996**, *8* (11), 2571-2578.
- (28) Vartuli, J. C.; Schmitt, K. D.; Kresge, C. T.; Roth, W. J.; Leonowicz, M. E.; McCullen, S. B.; Hellring, S. D.; Beck, J. S.; Schlenker, J. L., Effect of surfactant/silica molar ratios on the formation of mesoporous molecular sieves: Inorganic mimicry of surfactant liquid-crystal phases and mechanistic implications. *Chem. Mater.* **1994**, *6* (12), 2317-2326.
- (29) Romero, A. A.; Alba, M. D.; Zhou, W.; Klinowski, J., Synthesis and characterization of the mesoporous silicate molecular sieve MCM-48. *J. Phys. Chem. B* **1997**, *101* (27), 5294-5300.
- (30) Huo, Q.; Margolese, D. I.; Stucky, G. D., Surfactant control of phases in the synthesis of mesoporous silica-based materials. *Chem. Mater.* **1996**, *8* (5), 1147-1160.
- (31) Alfredsson, V.; Anderson, M. W.; Ohsuna, T.; Terasaki, O.; Jacob, M.; Bojrup, M., Cubosome description of the inorganic mesoporous structure MCM-48. *Chem. Mater.* **1997**, *9* (10), 2066-2070.

- (32) Khushalani, D.; Kuperman, A.; Ozin, G. A.; Tanaka, K.; Coombs, N.; Olken, M. M.; Garcés, J., Metamorphic materials: Restructuring siliceous mesoporous materials. *Adv. Mater.* **1995**, 7 (10), 842-846.
- (33) Ciesla, U.; Schüth, F., Ordered mesoporous materials. *Micropor. Mesopor. Mat.* **1999**, 27 (2-3), 131-149.
- (34) Zhao, D.; Huo, Q.; Feng, J.; Chmelka, B. F.; Stucky, G. D., Nonionic triblock and star diblock copolymer and oligomeric surfactant syntheses of highly ordered, hydrothermally stable, mesoporous silica structures. *J. Am. Chem. Soc.* **1998**, 120 (24), 6024-6036.
- (35) Kleitz, F.; Hei Choi, S.; Ryoo, R., Cubic *Ia3d* large mesoporous silica: Synthesis and replication to platinum nanowires, carbon nanorods and carbon nanotubes. *Chem. Comm.* **2003**, (17), 2136-2137.
- (36) Shin, H. J.; Ryoo, R.; Liu, Z.; Terasaki, O., Template synthesis of asymmetrically mesostructured platinum networks. *J. Am. Chem. Soc.* **2001**, 123 (6), 1246-1247.
- (37) Yu, C.; Yu, Y.; Zhao, D., Highly ordered large caged cubic mesoporous silica structures templated by triblock PEO-PBO-PEO copolymer. *Chem. Comm.* **2000**, (7), 575-576.
- (38) Fan, J.; Yu, C.; Gao, F.; Lei, J.; Tian, B.; Wang, L.; Luo, Q.; Tu, B.; Zhou, W.; Zhao, D., Cubic mesoporous silica with large controllable entrance sizes and advanced adsorption properties. *Angew. Chem., Int. Ed.* **2003**, 42 (27), 3146-3150.
- (39) Yu, C.; Tian, B.; Fan, J.; Stucky, G. D.; Zhao, D., Nonionic block copolymer synthesis of large-pore cubic mesoporous single crystals by use of inorganic salts. *J. Am. Chem. Soc.* **2002**, 124 (17), 4556-4557.
- (40) Fan, J.; Yu, C.; Wang, L.; Tu, B.; Zhao, D.; Sakamoto, Y.; Terasaki, O., Mesotunnels on the silica wall of ordered SBA-15 to generate three-dimensional large-pore mesoporous networks. *J. Am. Chem. Soc.* **2001**, 123 (48), 12113-12114.
- (41) Brinker, C. J. S., G.W., *Sol-Gel Science: The Physics and Chemistry of Sol-Gel Processing*. Academic Press: New York, 1990.
- (42) Voegtlin, A. C. R., F.; Guth, J.L.; Patarin, J.; Huve, L., F- mediated synthesis of mesoporous silica with ionic- and non-ionic surfactants. A new templating pathway. *Micropor. Mesopor. Mat.* **1997**, 9 (1,2), 95-105.
- (43) Kim, J. M.; Han, Y.-J.; Chmelka, B. F.; Stucky, G. D., One-step synthesis of ordered mesocomposites with non-ionic amphiphilic block copolymers: implications of isoelectric point, hydrolysis rate and fluoride. *Chem. Comm.* **2000**, (24), 2437-2438.
- (44) Kleitz, F.; Kim, T.-W.; Ryoo, R., Phase Domain of the Cubic *Im3m* Mesoporous Silica in the $\text{EO}_{106}\text{PO}_{70}\text{EO}_{106}$ -Butanol- H_2O System. *Langmuir* **2006**, 22 (1), 440-445.
- (45) Zhao, D.; Sun, J.; Li, Q.; Stucky, G. D., Morphological control of highly ordered mesoporous silica SBA-15. *Chem. Mater.* **2000**, 12 (2), 275-279.
- (46) Lu, Y.; Ganguli, R.; Drewien, C. A.; Anderson, M. T.; Brinker, C. J.; Gong, W.; Guo, Y.; Soye, H.; Dunn, B.; Huang, M. H.; Zink, J. I., Continuous formation of supported cubic and hexagonal mesoporous films by sol-gel dip-coating. *Nature* **1997**, 389 (6649), 364-368.

- (47) Zhao, D.; Yang, P.; Melosh, N.; Feng, J.; Chmelka, B. F.; Stucky, G. D., Continuous mesoporous silica films with highly ordered large pore structures. *Adv. Mater.* **1998**, *10* (16), 1380-1385.
- (48) Yu, C. Z. T.; Fan, J.; Tu, B.; Zhao, D.Y., *Chem. J. Chin. Univ.* **2003**, *24*, 5.
- (49) Yu, C.; Tian, B.; Fan, J.; Stucky, G. D.; Zhao, D., Synthesis of siliceous hollow spheres with ultra large mesopore wall structures by reverse emulsion templating. *Chem. Lett.* **2002**, *31* (1), 62-63.
- (50) Vinu, A.; Hossain, K. Z.; Ariga, K., Recent advances in functionalization of mesoporous silica. *J. Nanosci. Nanotechnol.* **2005**, *5* (3), 347-71.
- (51) Liu, Y.-H.; Lin, H.-P.; Mou, C.-Y., Direct method for surface silyl functionalization of mesoporous silica. *Langmuir* **2004**, *20* (8), 3231-3239.
- (52) Kecht, J.; Schlossbauer, A.; Bein, T., Selective functionalization of the outer and inner surfaces in mesoporous silica nanoparticles. *Chem. Mater.* **2008**, *20* (23), 7207-7214.
- (53) Trewyn, B. G.; Giri, S.; Slowing, II; Lin, V. S., Mesoporous silica nanoparticle based controlled release, drug delivery, and biosensor systems. *Chem. Comm.* **2007**, (31), 3236-45.
- (54) Zhao D.; Wan Y.; Zhou, W., *Ordered mesoporous materials*. Wiley: 2013.
- (55) Xu, M.; Arnold, A.; Buchholz, A.; Wang, W.; Hunger, M., Low-temperature modification of mesoporous MCM-41 material with sublimated aluminum chloride in vacuum. *J. Phys. Chem. B* **2002**, *106* (47), 12140-12143.
- (56) Okabe, A.; Niki, M.; Fukushima, T.; Aida, T., Ethanol vapor-mediated maturing for the enhancement of structural regularity of hexagonal mesoporous silica films. *Chem. Comm.* **2004**, (22), 2572-2573.
- (57) Vogel, R.; Dobe, C.; Whittaker, A.; Edwards, G.; Riches, J. D.; Harvey, M.; Trau, M.; Meredith, P., Postsynthesis stabilization of free-standing mesoporous silica films. *Langmuir* **2004**, *20* (7), 2908-2914.
- (58) Sayari, A., Unprecedented expansion of the pore size and volume of periodic mesoporous silica. *Angew. Chem., Int. Ed.* **2000**, *39* (16), 2920-2922.
- (59) Hamoudi, S.; Belkacemi, K., Cubic mesoporous silica with tailored large pores. *J. Porous Mater.* **2004**, *11* (1), 47-54.
- (60) Duncan, C. T.; Biradar, A. V.; Rangan, S.; Mishler, R. E.; Asefa, T., Trimming nanostructured walls while fluorinating their surfaces: A route to making and widening pores of nanoporous materials and efficient catalysts. *Chem. Mater.* **2010**, *22* (17), 4950-4963.
- (61) Langmuir, I., The adsorption of gases on plane surfaces of glass, mica and platinum. *J. Am. Chem. Soc.* **1918**, *40* (9), 1361-1403.
- (62) Trewyn, B. G.; Slowing, I. I.; Giri, S.; Chen, H.-T.; Lin, V. S. Y., Synthesis and functionalization of a mesoporous silica nanoparticle based on the sol-gel process and applications in controlled release. *Acc. Chem. Res.* **2007**, *40* (9), 846-853.
- (63) Tian, B.; Lui, X.; Yu, C.; Gao, F.; Luo, Q.; Xie, S.; Tu, B.; Zhao, D., Microwave assisted template removal of siliceous porous materials. *Chem. Comm.* **2002**, (11), 1186-7.
- (64) Jana, S. K.; Mochizuki, A.; Namba, S., Progress in pore-size control of mesoporous MCM-41 molecular sieve using surfactant having different alkyl

- chain lengths and various organic auxiliary chemicals. *Catal. Surv. Asia* **2004**, *8* (1), 1-13.
- (65) Barrett, E. P.; Joyner, L. G.; Halenda, P. P., The determination of pore volume and area distributions in porous substances. I. Computations from nitrogen isotherms. *J. Am. Chem. Soc.* **1951**, *73* (1), 373-380.
- (66) Widenmeyer, M.; Anwender, R., Pore size control of highly ordered mesoporous silica MCM-48. *Chem. Mater.* **2002**, *14* (4), 1827-1831.
- (67) Yu, C.; Fan, J.; Tian, B.; Stucky, G. D.; Zhao, D., Synthesis of mesoporous silica from commercial poly(ethylene oxide)/poly(butylene oxide) copolymers: Toward the rational design of ordered mesoporous materials. *J. Phys. Chem. B* **2003**, *107* (48), 13368-13375.
- (68) Kim, S. S.; Karkamkar, A.; Pinnavaia, T. J.; Kruk, M.; Jaroniec, M., Synthesis and characterization of ordered, very large pore MSU-H silicas assembled from water-soluble silicates. *J. Phys. Chem. B* **2001**, *105* (32), 7663-7670.
- (69) Kim, T.-W.; Kleitz, F.; Paul, B.; Ryoo, R., MCM-48-like large mesoporous silicas with tailored pore structure: Facile synthesis domain in a ternary triblock copolymer-butanol-water system. *J. Am. Chem. Soc.* **2005**, *127* (20), 7601-7610.
- (70) Van Der Voort, P.; Benjelloun, M.; Vansant, E. F., Rationalization of the synthesis of SBA-16: Controlling the micro- and mesoporosity. *J. Phys. Chem. B* **2002**, *106* (35), 9027-9032.
- (71) Ruggles, J. L.; Gilbert, E. P.; Holt, S. A.; Reynolds, P. A.; White, J. W., Expanded mesoporous silicate films grown at the air-water interface by addition of hydrocarbons. *Langmuir* **2003**, *19* (3), 793-800.
- (72) Lettow, J. S.; Han, Y. J.; Schmidt-Winkel, P.; Yang, P.; Zhao, D.; Stucky, G. D.; Ying, J. Y., Hexagonal to mesocellular foam phase transition in polymer-templated mesoporous silicas. *Langmuir* **2000**, *16* (22), 8291-8295.
- (73) Blin, J. L.; Su, B. L., Tailoring pore size of ordered mesoporous silicas using one or two organic auxiliaries as expanders. *Langmuir* **2002**, *18* (13), 5303-5308.
- (74) Hanrahan, J. P.; Copley, M. P.; Ryan, K. M.; Spalding, T. R.; Morris, M. A.; Holmes, J. D., Pore expansion in mesoporous silicas using supercritical carbon dioxide. *Chem. Mater.* **2004**, *16* (3), 424-427.
- (75) Chen, C.-Y.; Li, H.-X.; Davis, M. E., Studies on mesoporous materials. *Micropor. Mesopor. Mat.* **1993**, *2* (1), 17-26.
- (76) Annen, M. J.; Davis, M. E., Raman and ^{29}Si MAS NMR spectroscopy of framework materials containing three-membered rings. *Micropor. Mesopor. Mat.* **1993**, *1* (1), 57-65.
- (77) de Man, A. J. M.; Ueda, S.; Annen, M. J.; Davis, M. E.; van Santen, R. A., The stability and vibrational spectra of three-ring containing zeolitic silica polymorphs. *Zeolites* **1992**, *12* (7), 789-800.
- (78) Inagaki, S.; Guan, S.; Ohsuna, T.; Terasaki, O., An ordered mesoporous organosilica hybrid material with a crystal-like wall structure. *Nature* **2002**, *416* (6878), 304-307.
- (79) Zhou, W.; Fu, H.; Pan, K.; Tian, C.; Qu, Y.; Lu, P.; Sun, C.-C., Mesoporous $\text{TiO}_2/\alpha\text{-Fe}_2\text{O}_3$: Bifunctional composites for effective elimination of arsenite contamination through simultaneous photocatalytic oxidation and adsorption. *J. Phys. Chem. C* **2008**, *112* (49), 19584-19589.

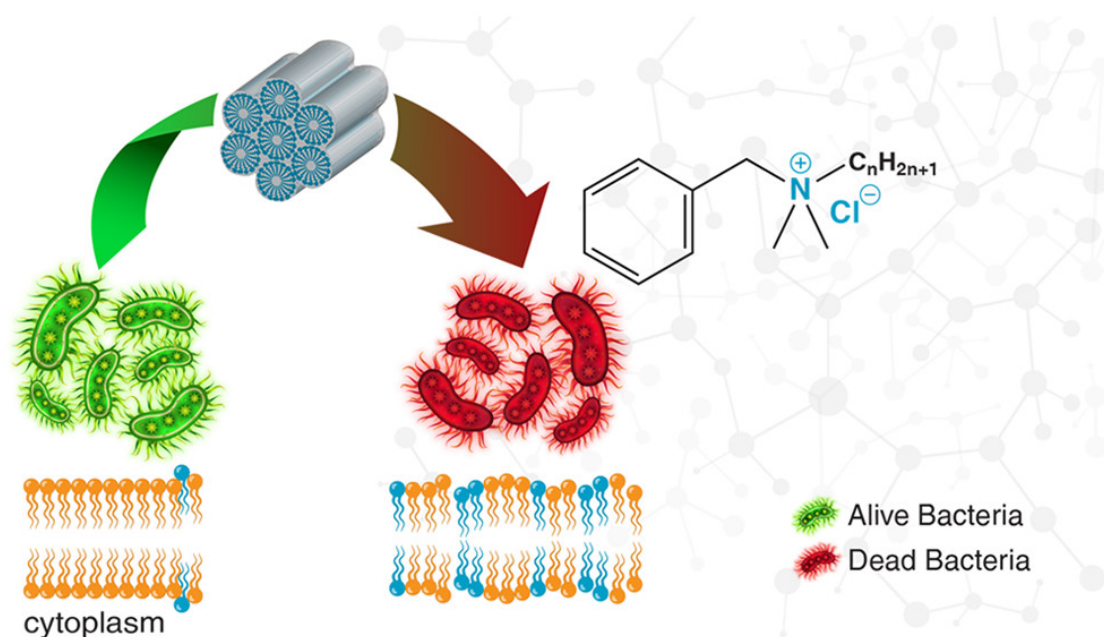
- (80) Kruk, M.; Jaroniec, M., Gas adsorption characterization of ordered organic–inorganic nanocomposite materials. *Chem. Mater.* **2001**, *13* (10), 3169–3183.
- (81) Jaroniec, M.; Solovyov, L. A., Improvement of the Kruk–Jaroniec–Sayari method for pore size analysis of ordered silicas with cylindrical mesopores. *Langmuir* **2006**, *22* (16), 6757–6760.
- (82) Jaroniec, M.; Kruk, M.; Jaroniec, C. P.; Sayari, A., Modification of surface and structural properties of ordered mesoporous silicates. *Adsorption* **1999**, *5* (1), 39–45.
- (83) Groen, J. C.; Peffer, L. A. A.; Pérez-Ramírez, J., Pore size determination in modified micro- and mesoporous materials. Pitfalls and limitations in gas adsorption data analysis. *Micropor. Mesopor. Mat.* **2003**, *60* (1–3), 1–17.
- (84) Solovyov, L. A.; Belousov, O. V.; Dinnebier, R. E.; Shmakov, A. N.; Kirik, S. D., X-ray diffraction structure analysis of MCM-48 mesoporous silica. *J. Phys. Chem. B* **2005**, *109* (8), 3233–3237.
- (85) Langford, J. I.; Wilson, A. J. C., Scherrer after sixty years: A survey and some new results in the determination of crystallite size. *J. Appl. Crystallogr.* **1978**, *11* (2), 102–113.
- (86) Trébosc, J.; Wiench, J. W.; Huh, S.; Lin, V. S. Y.; Pruski, M., Solid-state NMR study of MCM-41-type mesoporous silica nanoparticles. *J. Am. Chem. Soc.* **2005**, *127* (9), 3057–3068.
- (87) Babonneau, F.; Yeung, L.; Steunou, N.; Gervais, C.; Ramila, A.; Vallet-Regi, M., Solid state NMR characterisation of encapsulated molecules in mesoporous silica. *J. Sol-Gel Sci. Techn.* **2004**, *31* (1), 219–223.
- (88) Easwaramoorthi, S.; Ananthanarayanan, K.; Sreedhar, B.; Natarajan, P., X-ray photoelectron spectroscopic investigation of phenosafranine adsorbed onto micro and mesoporous materials. *J. Chem. Sci.* **2009**, *121* (5), 711–718.
- (89) Hartono, S. B.; Phuoc, N. T.; Yu, M.; Jia, Z.; Monteiro, M. J.; Qiao, S.; Yu, C., Functionalized large pore mesoporous silica nanoparticles for gene delivery featuring controlled release and co-delivery. *J. Mater. Chem. B* **2014**, *2* (6), 718–726.
- (90) Perego, C.; Millini, R., Porous materials in catalysis: Challenges for mesoporous materials. *Chem. Soc. Rev.* **2013**, *42* (9), 3956–3976.
- (91) Chen, Y.; Shi, J., Chemistry of mesoporous organosilica in nanotechnology: Molecularly organic-inorganic hybridization into frameworks. *Adv. Mater.* **2016**, *28* (17), 3235–72.
- (92) Rodzinski, A.; Guduru, R.; Liang, P.; Hadjikhani, A.; Stewart, T.; Stimphil, E.; Runowicz, C.; Cote, R.; Altman, N.; Datar, R.; Khizroev, S., Targeted and controlled anticancer drug delivery and release with magnetoelectric nanoparticles. *Sci. Rep.* **2016**, *6*, 20867.
- (93) Asefa, T.; Tao, Z., Biocompatibility of mesoporous silica nanoparticles. *Chem. Res. Toxicol.* **2012**, *25*, 2265–2284.
- (94) Chen, X.; Liu, Z., Dual responsive mesoporous silica nanoparticles for targeted co-delivery of hydrophobic and hydrophilic anticancer drugs to tumor cells. *J. Mater. Chem. B* **2016**, *4* (25), 4382–4388.

- (95) Croissant, J.; Salles, D.; Maynadier, M.; Mongin, O.; Hugues, V.; Blanchard-Desce, M.; Cattoën, X.; Wong Chi Man, M.; Gallud, A.; Garcia, M.; Gary-Bobo, M.; Raehm, L.; Durand, J.-O., Mixed periodic mesoporous organosilica nanoparticles and core-shell systems, application to in vitro two-photon imaging, therapy, and drug delivery. *Chem. Mater.* **2014**, *26* (24), 7214-7220.
- (96) Hata, H.; Saeki, S.; Kimura, T.; Sugahara, Y.; Kuroda, K., Adsorption of taxol into ordered mesoporous silicas with various pore diameters. *Chem. Mater.* **1999**, *11* (4), 1110-1119.
- (97) Horcajada, P.; Ramila, A.; Perez-Pariente, J.; Vallet-Regi, M., Influence of pore size of MCM-41 matrices on drug delivery rate. *Micropor. Mesopor. Mat.* **2004**, *68*, 105-109.
- (98) Izquierdo-Barba, I. M., A.; Doadrio, A.L.; Perez-Pariente, J.; Vallet-Regi, M., Release evaluation of drugs from ordered three-dimensional silica structures. *Eur. J. Pharm. Sci.* **2005**, *26*, 365-373.
- (99) Andersson, J.; Rosenholm, J.; Areva, S.; Lindén, M., Influences of material characteristics on ibuprofen drug loading and release profiles from ordered micro- and mesoporous silica matrices. *Chem. Mater.* **2004**, *16* (21), 4160-4167.
- (100) Vallet-Regi, M.; Balas, F.; Colilla, M.; Manzano, M., Drug confinement and delivery in ceramic implants. *Drug Metab. Lett.* **2007**, *1* (1), 37-40.
- (101) Zou, Z.; He, D.; Cai, L.; He, X.; Wang, K.; Yang, X.; Li, L.; Li, S.; Su, X., Alizarin complexone functionalized mesoporous silica nanoparticles: A smart system integrating glucose-responsive double-drugs release and real-time monitoring capabilities. *ACS Appl. Mater. Interfaces* **2016**, *8* (13), 8358-66.
- (102) Wu, K. C.; Yamauchi, Y.; Hong, C. Y.; Yang, Y. H.; Liang, Y. H.; Funatsu, T.; Tsunoda, M., Biocompatible, surface functionalized mesoporous titania nanoparticles for intracellular imaging and anticancer drug delivery. *Chem. Comm.* **2011**, *47* (18), 5232-4.
- (103) Feng, W.; Zhou, X.; He, C.; Qiu, K.; Nie, W.; Chen, L.; Wang, H.; Mo, X.; Zhang, Y., Polyelectrolyte multilayer functionalized mesoporous silica nanoparticles for pH-responsive drug delivery: layer thickness-dependent release profiles and biocompatibility. *J. Mater. Chem. B* **2013**, *1* (43), 5886-5898.
- (104) Grün, M.; Kurganov, A. A.; Schacht, S.; Schüth, F.; Unger, K. K., Comparison of an ordered mesoporous aluminosilicate, silica, alumina, titania and zirconia in normal-phase high-performance liquid chromatography. *J. Chromatogr. A* **1996**, *740* (1), 1-9.
- (105) Thoelen, C.; Van de Walle, K.; F. J. Vankelecom, I.; A. Jacobs, P., The use of M41S materials in chiral HPLC. *Chem. Comm.* **1999**, (18), 1841-1842.
- (106) Zhang, J.-H.; Xie, S.-M.; Zhang, M.; Zi, M.; He, P.-G.; Yuan, L.-M., Novel inorganic mesoporous material with chiral nematic structure derived from nanocrystalline cellulose for high-resolution gas chromatographic separations. *Anal. Chem.* **2014**, *86* (19), 9595-9602.
- (107) Jang, K.-S.; Kim, H.-J.; Johnson, J. R.; Kim, W.-g.; Koros, W. J.; Jones, C. W.; Nair, S., Modified mesoporous silica gas separation membranes on polymeric hollow fibers. *Chem. Mater.* **2011**, *23* (12), 3025-3028.

- (108) Zornoza, B.; Irusta, S.; Téllez, C.; Coronas, J., Mesoporous silica sphere-polysulfone mixed matrix membranes for gas separation. *Langmuir* **2009**, 25 (10), 5903-5909.
- (109) Newalkar, B. L.; Choudary, N. V.; Turaga, U. T.; Vijayalakshmi, R. P.; Kumar, P.; Komarneni, S.; Bhat, T. S. G., Potential adsorbent for light hydrocarbon separation: Role of SBA-15 framework porosity. *Chem. Mater.* **2003**, 15 (7), 1474-1479.
- (110) Katiyar, A.; Ji, L.; Smirniotis, P.; Pinto, N. G., Protein adsorption on the mesoporous molecular sieve silicate SBA-15: Effects of pH and pore size. *J. Chromatogr. A* **2005**, 1069 (1), 119-126.
- (111) Giraldo, L. F. L., B.L.; Perez, L.; Urrego, S.; Sierra, L.; Mesa, M., Mesoporous silica applications. *Macromol. Symp.* **2007**, 258, 129-141.
- (112) Nooney, R. I.; Kalyanaraman, M.; Kennedy, G.; Maginn, E. J., Heavy metal remediation using functionalized mesoporous silicas with controlled macrostructure. *Langmuir* **2001**, 17 (2), 528-533.
- (113) Brigante, M.; Pecini, E.; Avena, M., Magnetic mesoporous silica for water remediation: Synthesis, characterization and application as adsorbent of molecules and ions of environmental concern. *Micropor. Mesopor. Mat.* **2016**, 230, 1-10.
- (114) Nakamura, T.; Sugihara, F.; Matsushita, H.; Yoshioka, Y.; Mizukami, S.; Kikuchi, K., Mesoporous silica nanoparticles for ¹⁹F magnetic resonance imaging, fluorescence imaging, and drug delivery. *Chem. Sci.* **2015**, 6 (3), 1986-1990.
- (115) Hurley, K. R.; Ring, H. L.; Etheridge, M.; Zhang, J.; Gao, Z.; Shao, Q.; Klein, N. D.; Szlag, V. M.; Chung, C.; Reineke, T. M.; Garwood, M.; Bischof, J. C.; Haynes, C. L., Predictable heating and positive MRI contrast from a mesoporous silica-coated iron oxide nanoparticle. *Mol. Pharm.* **2016**, 13 (7), 2172-2183.
- (116) Cao, M.; Wang, P.; Kou, Y.; Wang, J.; Liu, J.; Li, Y.; Li, J.; Wang, L.; Chen, C., Gadolinium(III)-chelated silica nanospheres integrating chemotherapy and photothermal therapy for cancer treatment and magnetic resonance imaging. *ACS Appl. Mater. Interfaces* **2015**, 7 (45), 25014-25023.
- (117) Konjhodzic, D.; Bretinger, H.; Marlow, F., Structure and properties of low-n mesoporous silica films for optical applications. *Thin Solid Films* **2006**, 495 (1-2), 333-337.
- (118) Chen, H.-W.; Liang, C.-P.; Huang, H.-S.; Chen, J.-G.; Vittal, R.; Lin, C.-Y.; Wu, K. C. W.; Ho, K.-C., Electrophoretic deposition of mesoporous TiO₂ nanoparticles consisting of primary anatase nanocrystallites on a plastic substrate for flexible dye-sensitized solar cells. *Chem. Comm.* **2011**, 47 (29), 8346-8348.
- (119) Choi, M.; Kleitz, F.; Liu, D.; Lee, H. Y.; Ahn, W.-S.; Ryoo, R., Controlled polymerization in mesoporous silica toward the design of organic-inorganic composite nanoporous materials. *J. Am. Chem. Soc.* **2005**, 127 (6), 1924-1932.

CHAPTER 2

One-Pot Hydrothermal Synthesis of Benzalkonium-Templated Mesostructured Silica Antibacterial Agents



2.1. Overview

Novel mesostructured silica nanoparticles were synthesized, *via* soft-templating with a cationic bactericidal drug, benzalkonium chloride (BAC), characterized and investigated as a drug delivery system (DDS) for antimicrobial applications. The material exhibited a relatively high density (0.56 g per 1 g SiO₂) of BAC, pore channels of 18 Å in width, and a high surface area ($\sim 1500 \text{ m}^2 \text{ g}^{-1}$). Comparison of SAXRD pattern with BJH pore size distribution data suggests that the 18 Å pores exhibit short range ordering and a wall thickness of *ca.* 12 Å. Drug release studies demonstrate pH-responsive controlled release of BAC without additional surface modification of the material. Prolonged drug

release data was analyzed using a power law (Korsmeyer-Peppas) model and indicates substantial differences in release mechanism in acidic (pH 4.0) versus neutral (pH 7.4) solutions. Microbiological assays demonstrate a significant time-dependent reduction in *Staphylococcus aureus* and *Salmonella enterica* viability above 10 and 130 mg L⁻¹ of the synthesized material, respectively. The viability of cells was reduced over time compared to no treatment or SiO₂ only treatment. The findings will help in widening the use of BAC as a disinfectant and bactericidal agent especially in pharmaceutical and food industries where gram-positive and gram-negative contamination is common.

2.2. Introduction

Over the past several decades, mesoporous silica nanoparticles (MSNs) have attracted a great deal of interest in fields such as catalysis, drug delivery systems (DDS), sensing, environmental remediation, and nanoelectronics due to their unique structures and properties (*e.g.*, high surface area, uniform pores, large pore volumes and tunable pore sizes).¹⁻⁸ Since the first report of drug delivery systems based on MSNs, research on biomedical applications of MSNs has increased exponentially each year.^{2,9} MSNs demonstrated significant advantages over traditional nano-based formulations for potential treatment of diabetes, inflammation, and especially cancer.¹⁰⁻¹⁴ However, significant effort is still warranted to overcome the key challenges involved with developing effective DDSs that can attain: 1) sufficient drug loading capacity; 2) controlled or activated release; 3) targeted delivery of drug; and 4) biocompatibility. In this work, novel mesostructured silica nanoparticles, dubbed BAC-SiO₂, are developed

for antimicrobial drug delivery by using the bactericidal drug benzalkonium chloride (BAC) as the template during a one-step hydrothermal synthesis.

MSNs are typically synthesized with “inert” structure directing agents (SDAs), commonly referred to as soft templates, with their subsequent removal to yield nanoporous structures suitable for surface modification and drug loading. On the other hand, several previous reports have described the use of different active molecules (*e.g.*, a corrosion inhibitor, an antitumor drug) as templates for the synthesis of various porous silica materials.¹⁵⁻¹⁷ Although numerous advantages of one-step fabrication of DDSs have been realized through these works, there have been only a few reports, especially involving those with antimicrobial applications, and the efficacy of the fabricated materials is often not evaluated beyond the scope of drug release kinetics.

BAC is a mixture of different alkylbenzyltrimethylammonium ions or surfactants with a range of hydrocarbon chains (C₈-C₁₈) (Figure 2.1). BAC forms micelles in aqueous solution above critical micelle concentration of *ca.* 0.5 mM.¹⁸ BAC is a ubiquitous ingredient in food, pharmaceutical, and industrial formulations due to its broad spectrum of bactericidal activity. In small concentrations, it affects the membrane permeability to cause cytolytic leakage of cytoplasmic materials (Figure 2.1); however, at high concentrations, it targets carboxylic groups to cause coagulation in the bacterial cytoplasm.¹⁹ Herein, we report the synthesis, drug release kinetics, and antibacterial activity of benzalkonium-templated mesoporous silica (BAC-SiO₂). The material demonstrates a relatively high payload of drug, sustained and prolonged release of BAC in physiologically-relevant pH ranges (4-8), an extremely high surface area framework upon removal of the BAC, and a time-dependent bactericidal activity. To the best of our

knowledge, this is the first report of a BAC-templated mesoporous silica as well as its antibacterial activities.

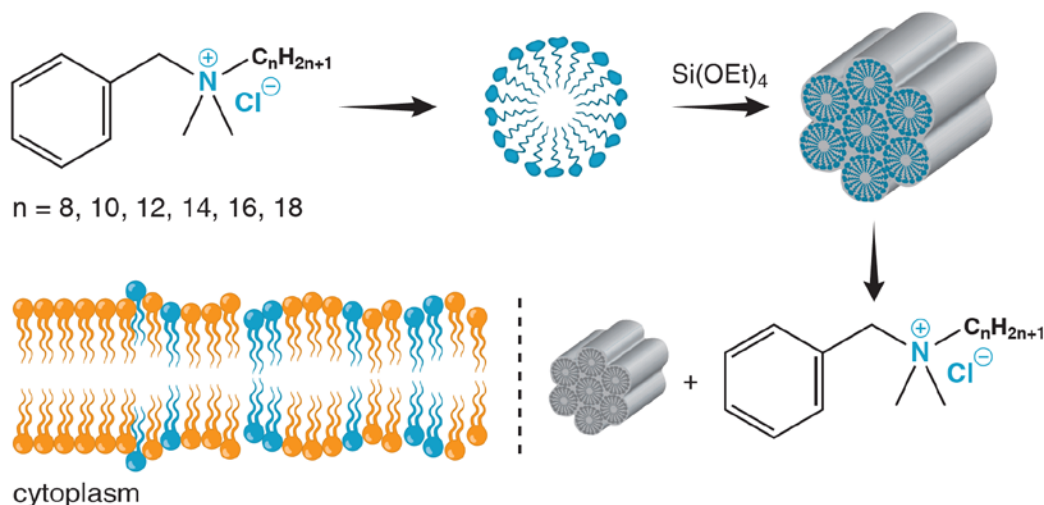


Figure 2.1. Schematic illustration of the synthetic procedure, drug release, and antimicrobial mode of action.

2.3. Experimental Section

2.3.1. Materials and Reagents

Reagent grade tetraethyl orthosilicate (TEOS), BTC® 50 solution of 50% benzalkonium chloride (BAC), and 30% aqueous ammonium hydroxide (NH_4OH) were supplied by Sigma-Aldrich (St. Louis, MO), Stepan (Northfield, IL) and Sigma-Aldrich (St. Louis, MO), respectively. All materials were used as received without any further purification.

2.3.2. Synthesis of MSNs

Synthesis of the MSN was carried out under mildly alkaline conditions according to the molar ratio 1 TEOS: 4 NH_4OH : 0.25 BAC : 135 H_2O . BAC (4.023 g), NH_4OH (11.40 g), and deionized water (56.7 g) were combined in a Teflon-lined autoclave, under magnetic stirring, to form a clear solution. Then, 5.076 g of TEOS was added dropwise under stirring, and the mixture was subsequently heated at 80 °C for 72 h. A fluffy, white powder was recovered after filtration, washing, and drying at 50 °C. For subsequent analysis and characterization experiments, the as-synthesized sample was calcined in air at 550 °C for 6 h to remove the template.

2.3.3. Synthesis of BAC-SiO₂

The synthesis of BAC-SiO₂ nanoparticles entailed diluting appropriate amounts of BAC and NH_4OH using deionized water with subsequent drop-wise addition of tetraethyl orthosilicate (TEOS) under stirring. The distribution of alkyl chains in BAC is 50% C12, 30% C14, 17% C16, and 3% C18. The mixture, with the composition of BAC : TEOS : NH_4OH : H_2O = 0.25 : 1.00 : 4.00 : 135.00, was heated at 80 °C in a 125 mL autoclave for 72 h and subsequently filtered, and the solid product was washed with 100 mL of water and dried in a 50 °C oven overnight.

2.3.4. Instrumentation

Attenuated total reflectance Fourier transform infrared (ATR-FTIR) spectroscopy analysis was conducted on BAC-SiO₂ and lyophilized BAC samples. The ATR-FTIR

spectra ($650\text{--}4000\text{ cm}^{-1}$ with 4 cm^{-1} resolution) were collected using a Perkin Elmer (Waltham, MA) Spectrum 2000 system featuring a KBr beam splitter, DTGS detector, and single-bounce diamond ATR crystal.

Prior to N_2 sorption experiments, the samples were initially de-gasified for 8 h at $80\text{ }^\circ\text{C}$ under a nitrogen atmosphere using a Micromeritics (Norcross, GA) FlowPrep 060 Sample Degas System. Nitrogen adsorption-desorption isotherms were measured on a Micromeritics (Norcross, GA) Tristar 3000 instrument (Norcross, GA). The specific surface areas were calculated by using the Brunauer-Emmett-Teller (BET) method. The pore sizes and pore size distributions were calculated from the isotherms according to the Barrett-Joyner-Halenda (BJH) method. From the amount of N_2 adsorbed at a relative pressure (P/P_0) of 0.99, the total pore volume of the material was obtained.

Aqueous size distribution was measured by the static light scattering technique. An aliquot of the fresh solution was transferred to a polystyrene cuvette prior to analysis. The SAXS measurements were performed at the 12-ID-B beamline of the Advanced Photon Source (APS) at Argonne National Laboratory, using 13.3 keV X-ray energy and 0.9322 \AA wavelength. The SAXS data were collected with a Pilatus 2 M detector (DECTRIS Ltd.), and the cutoff energy was set as 10 keV to eliminate possible fluorescence background. The beam size with $0.1 \times 0.2\text{ mm}^2$ and exposure times of 1 s were used for the measurement. The sample-to-detector distance was *ca.* 2 m , and the scattering vector (q) range covers $0.004 - 0.9\text{ \AA}^{-1}$. The 2-D SAXS patterns were fully corrected, reduced to 1-D intensity versus q profiles, and background subtracted, using the software package at the beamline.

The amount of BAC incorporated in the MSN was calculated by thermogravimetric analysis (TGA) using a TGA 7 Thermogravimetric Analyzer (Perkin Elmer, Waltham, MA) instrument. The analysis was carried out in open platinum crucibles over a temperature range of 50-550 °C at a heating rate of 10 °C /min. Differential scanning calorimetry was conducted on a TA DSC Q20 equipped with a TA refrigerated cooling system.

Sample preparation for TEM experiments entailed suspending the sample in ethanol, dropping onto a holey copper grid, and allowed to air-dry in room temperature. The electron microscopy experiments were performed using a JEOL 2010F microscope operated at 197 kV. The spatial resolution of the microscope in the high resolution (HRTEM) mode is ~ 0.14 nm. The fast Fourier transform of the HRTEM images generates spots which correspond to crystallographic periodic arrangements of atomic planes. These spots were also used as filters to remove background noise from the high resolution images. All HRTEM images were analyzed using Gatan Digital Micrograph software.

The X-ray scattering from the sample was obtained by use of a Bruker Vantec-500 area detector and a Bruker FR571 rotating-anode X-ray generator operating at 40 kV and 50 mA. The diffraction system was equipped with a 3-circle Azlan goniometer, but the sample was not moved during X-ray data collection. The system used 0.5 mm pinhole collimation and a Rigaku Osmic parallel-mode (*e.g.*, primary beam dispersion less than 0.01 deg in 2θ) mirror monochromator (Cu K α ; $\lambda = 1.5418\text{\AA}$). Data were collected at room temperature (20 °C) with a sample to detector distance of 26.2 cm. Spatial calibration and flood-field correction for the area detector were performed at this distance

prior to data collection. The 2048 x 2048 pixel images were collected at the fixed detector (2θ) angle of 50° for 3 min with ω step of 0.00 deg. For the intensity versus 2θ plot, a 0.02 degree step, bin-normalized χ integration was performed on the image shown below with settings $0 < 2\theta < 13$ deg and $-180 < \chi < 180$ deg. Data collection and rocking curve creation: Bruker GADDS v.4.1.51 (2015). Data display and graphics: MDI JADE7 v.7.0.6 (2004).

2.3.5. Drug Release Studies

The release of BAC from the MSN under static condition at room temperature was investigated at different pH conditions: 1) HCl solution pH 4.0 and 2) phosphate-buffered saline (PBS) solution pH 7.4. Calibration curves were plotted by measuring the UV-Vis spectroscopy of pure BAC in the corresponding solutions. Specifically, 400 mg of BAC-SiO₂ was suspended in 50 mL of dispersion medium. The solution was centrifuged at prefixed time intervals, and a 1 mL aliquot of the supernatant was taken using a pipette and analyzed for BAC content at λ_{max} of 262 nm. The region between 240 and 280 nm exhibits three peaks in UV-Vis, which is consistent with UV-Vis of other quaternary ammonium surfactants.²⁰ The analyzed supernatant was then returned to the solution. This process was repeated at different intervals of time until no further substantial release was observed. The absorption intensity was plotted as a function of time using a Lambda 850 UV/VIS Spectrometer (Perkin Elmer, Waltham, MA). The drug loading capacity was then computed to a value of x g/g using the following equation:

$$\text{Drug loading capacity} = \frac{\text{mass of drug in the MSNs}}{\text{mass of drug-loaded MSN}} \quad (\text{Equation 2.1})$$

2.3.6. Antimicrobial Assays

Broth cultures were grown at 37 °C with a shake speed of 200 RPM in 250 mL flasks. Cultures of *Staphylococcus aureus* USA300_LAC and *Salmonella enterica* serovar typhimurium LT2 were grown for 18 hours in 75 mL of Mueller-Hinton (Sigma-Aldrich) medium. *S. enterica* and *S. aureus* were individually diluted in triplicate into flasks containing 30 mL or 100 mL of Mueller-Hinton broth to an optical density (A_{600}) of 0.1, respectively. Subsequently, bacteria were combined with vehicle control, BAC-SiO₂, BAC, or SiO₂. At various times, bacteria were removed from the flasks, serially diluted using sterile phosphate buffered saline, and 5 μ L of each dilution was then by drop plated onto solid tryptic soy medium (MP biomedical). The plates were incubated at 37 °C for 18 hours before the number of viable bacteria was enumerated by counting the number of colony forming units (CFU).

2.4. Results and Discussion

Synchrotron small-angle X-ray scattering (SAXS) and static light scattering (SLS) measurements of aqueous BAC/NH₄OH solution prior to TEOS addition revealed the presence of nano-sized BAC micelle aggregates. SAXS profile (Figure 2.2) exhibits diffraction peaks within the range of *ca.* 20-70 Å. Static light scattering (SLS) measurements (Figure 2.3), in decent agreement of SAXS, revealed size distribution between *ca.* 10-50 Å. The FTIR spectra of both BAC and BAC-SiO₂ (Figure 2.4a) exhibited C-H stretching bands (2854 cm⁻¹ and 2924 cm⁻¹) and C-H bending vibration band (1457 cm⁻¹), due to alkylammonium groups.¹²⁻¹⁴ Asymmetric (1044 cm⁻¹) and

symmetric (809 cm^{-1}) bands associated with Si-O-Si were observed in the spectra of BAC-SiO₂ before and after calcination.^{20,21}

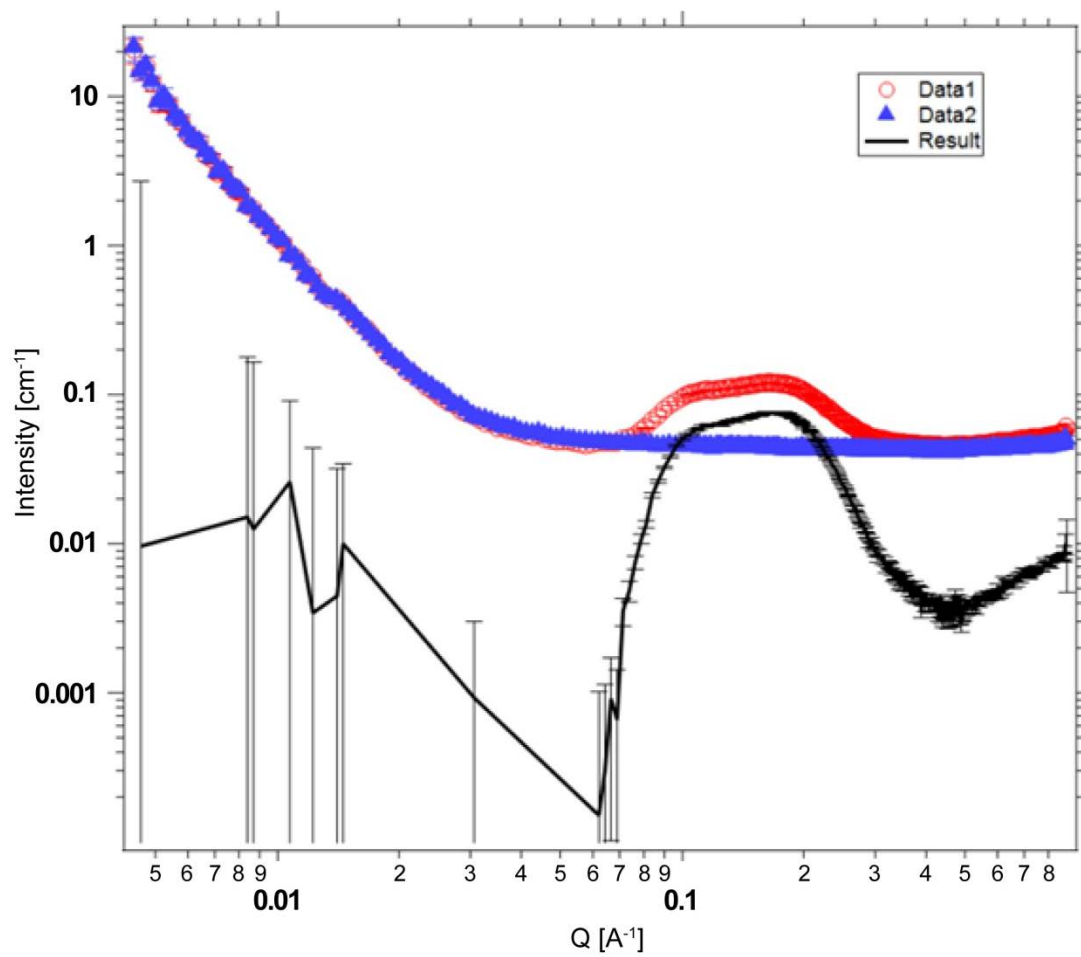


Figure 2.2. Synchrotron-SAXS measurement (red) of aqueous BAC/NH₄OH solution prior to TEOS addition with its corresponding curved fit (blue) and the subtracted plot (black).

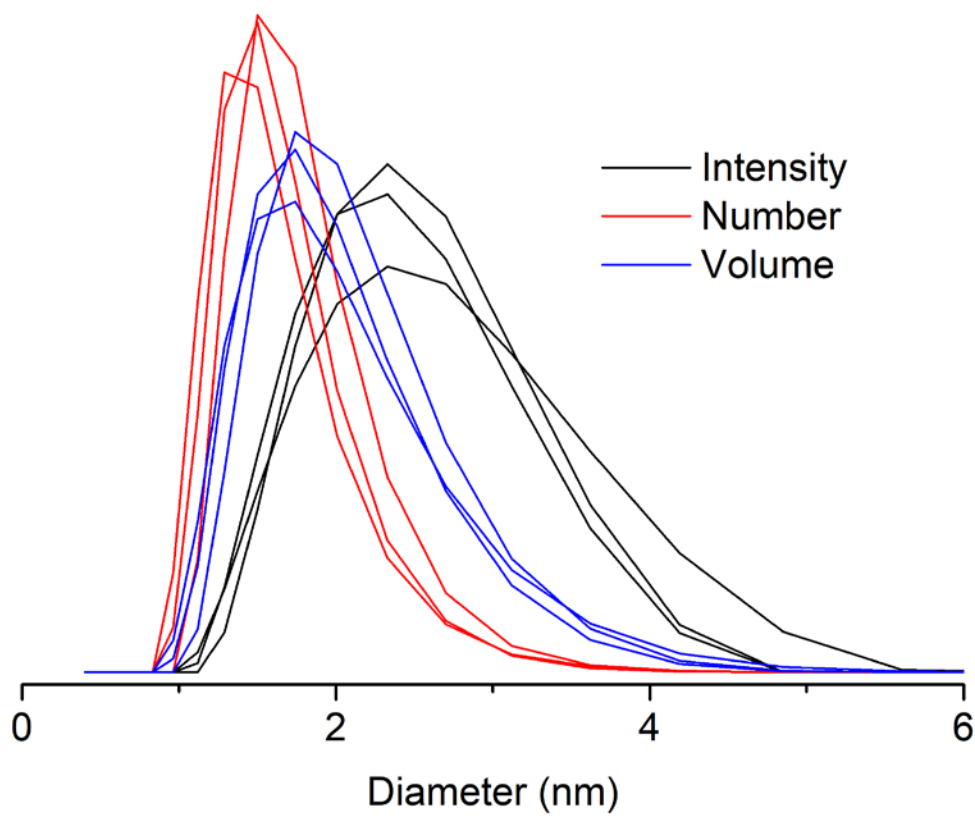


Figure 2.3. SLS measurement of aqueous BAC/ NH_4OH solution prior to the addition of TEOS demonstrating scattering intensity (y-axis) versus diameter (x-axis).

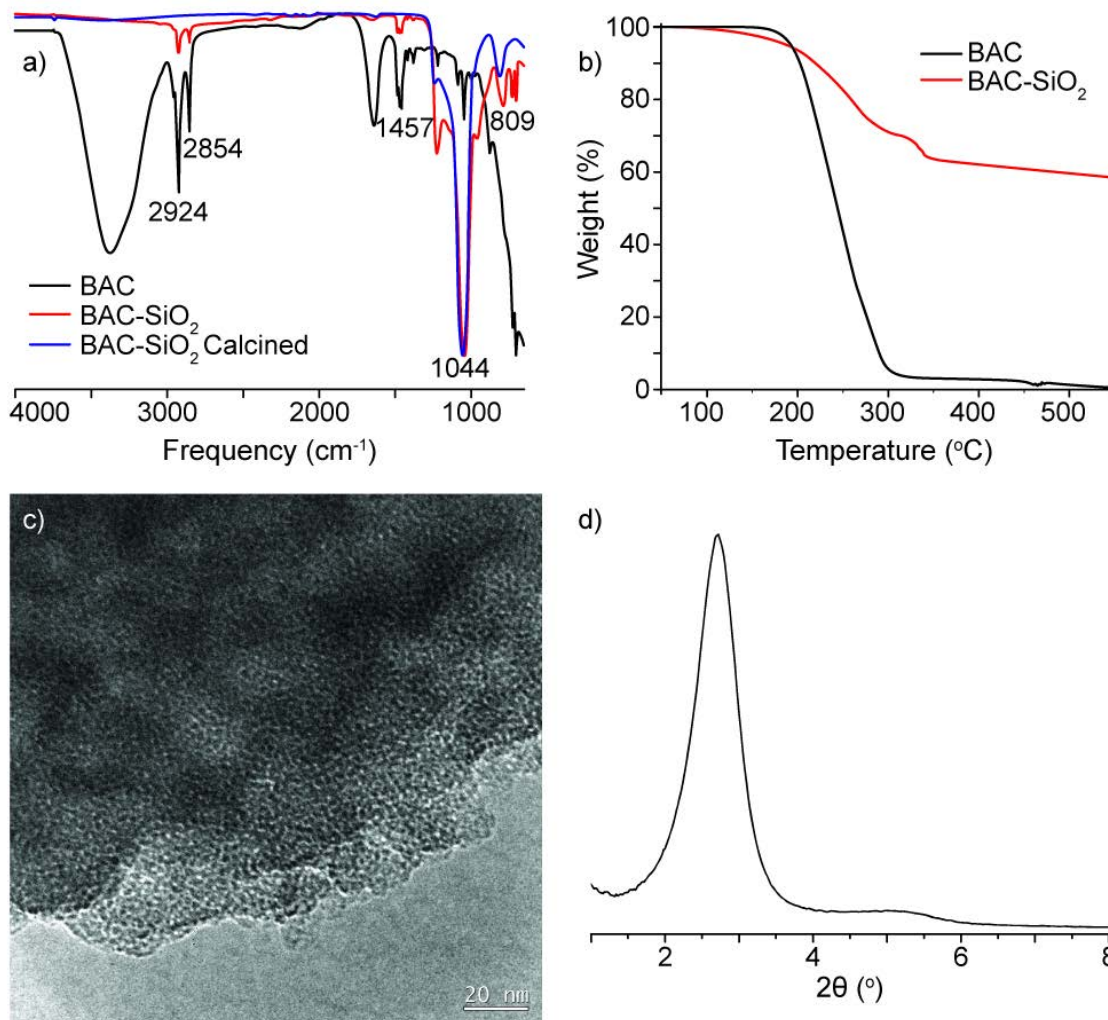


Figure 2.4. (a) ATR-FTIR spectra of lyophilized BAC, BAC-SiO₂ and calcined BAC-SiO₂; (b) thermogravimetric analysis (TGA) data plots of lyophilized BAC and as-synthesized BAC-SiO₂; (c) HR-TEM micrograph of calcined BAC-SiO₂; and (d) small-angle X-ray diffraction (SAXRD) pattern of calcined BAC-SiO₂.

Quantification of BAC within the framework of BAC-SiO₂ was conducted using TGA. Consistent with previous reports of quaternary ammonium surfactants, TGA data of freeze-dried BAC showed a 95 % weight loss in the range of 170-300 °C due to its

thermal degradation (Figure 2.4b).^{20,22} On the other hand, the TGA curve of BAC-SiO₂ exhibited four distinct weight loss ranges: 1) the loss of water, and maybe residual ammonia from the synthesis, at < 170 °C; 2) first step of BAC degradation in the range of 170-300 °C; 3) second step of BAC degradation in the range of 300-340 °C; and 4) loss of water due to condensation of silanol groups. The weight loss between 170-340 °C was *ca.* 36% (0.56 g per 1 g SiO₂), which corresponds to the amount of BAC within the BAC-SiO₂. DSC results obtained for the materials (Figure 2.5) demonstrated that the predominant endothermic peak for BAC-SiO₂ and BAC occurred at 120-140 °C and 185-230 °C, respectively.

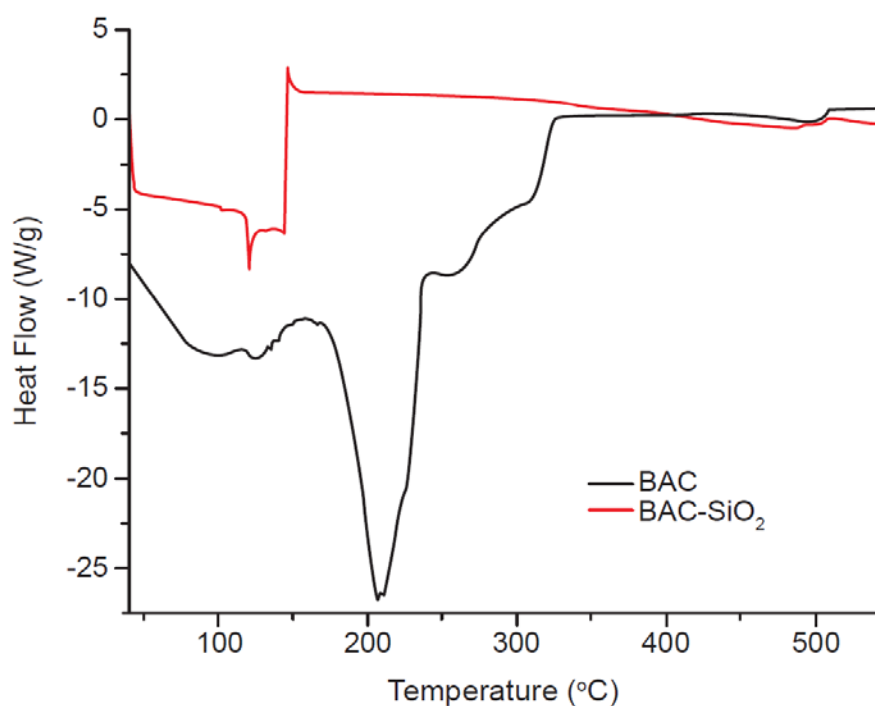


Figure 2.5. Differential scanning calorimetry (DSC) plots of BAC and BAC-SiO₂.

Calcination of BAC-SiO₂ at 550 °C for 6 h yielded mesoporous silica. TEM micrograph of the starting (Figure 2.6a-b) and resulting material (Figure 2.4c) showed seemingly disordered mesopores structures with pore widths on the order of 30 - 50 Å. The particle size was on the order of 600-900 nm in diameter. The SAXRD pattern (Figure 2.4d) was characteristic of an isotropic material that forms layers by virtue of consistent size rather than by extended 1D or 2D periodic arrangements of molecules. Thus, there was no short d-spacing diffraction pattern from aligned molecular species. There was only random packing of nearest neighbor pores that gave rise to a consistent, but isotropic, scattering vector near 32 Å, which is the approximate distance between rows of pores. If the pattern was cubic, then the pore-to-pore centroids are what were measured. However, information gathered from TEM micrographs and expected packing arrangements of random spheres appeared to favor an hcp motif, making the observed value to be $\sqrt{3}/2$ times the average core-to-core distance. Thus, the average core-to-core distance was about 37 Å. By incorporating the Scherrer equation, the domain spacing was determined to be *ca.* 11 nm, which is consistent with three repeats of the 37 Å spacing (*i.e.*, on average there are triplets of pores that scatter well enough).^{23,24}

The N₂ sorption results revealed a type IV isotherm with a capillary condensation step with a type H4 hysteresis loop (Figure 2.7), which is characteristic of mesoporous materials. The BET surface area, the average pore width, and the pore volume were found to be 1579 m² g⁻¹, 18.4 Å, and 0.56 cm³ g⁻¹, respectively.^{25,26} However, the Kruk-Jaroniec-Sayari (KJS) corrections on the data with cylindrical pore assumptions yielded a pore width closer to 30 Å.²⁷ The hysteresis loop also suggested the presence of larger mesopores (~100-500 Å) due to inter-particle gaps.

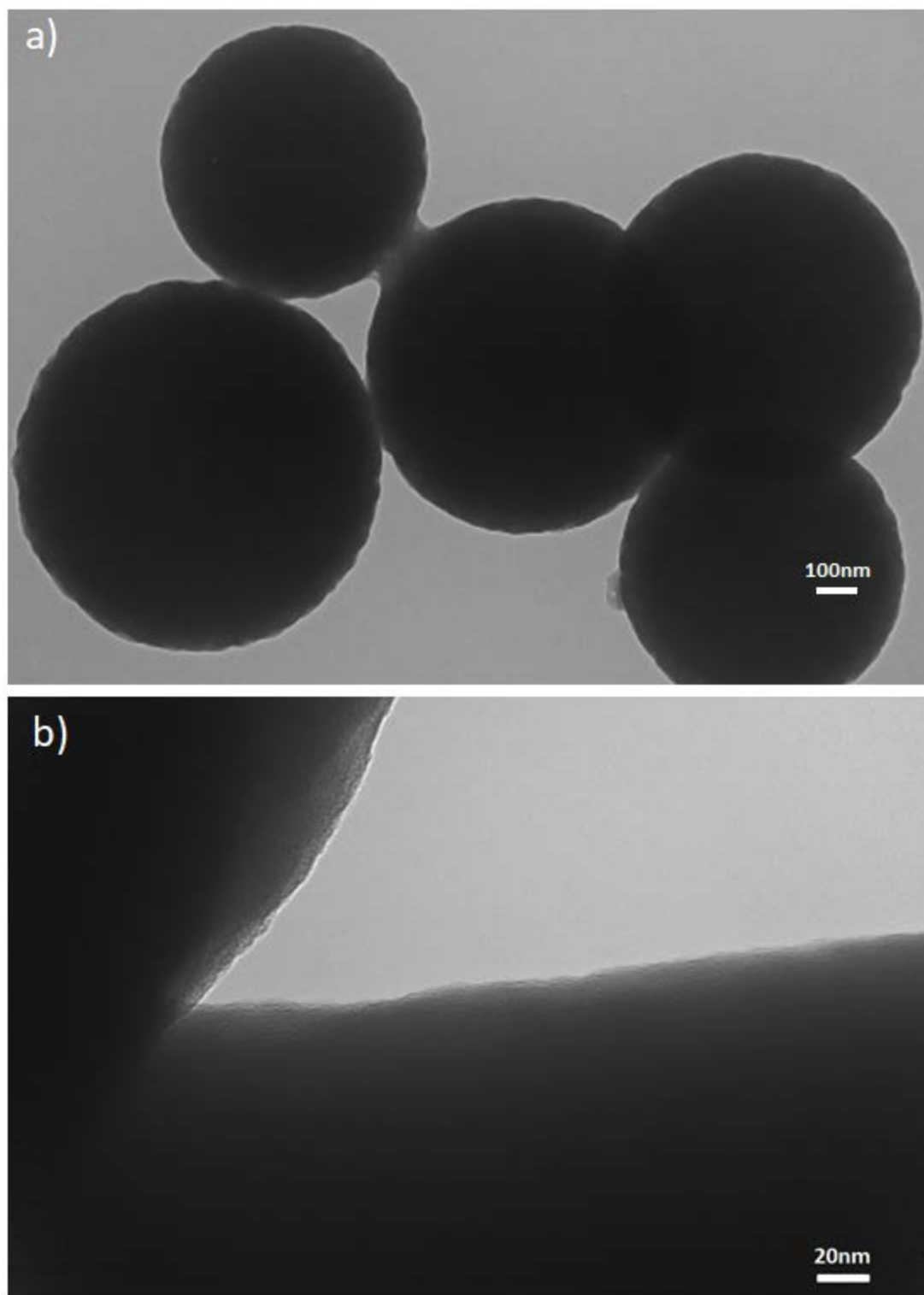


Figure 2.6. (a) Normal and (b) enlarged TEM images of as-synthesized BAC-SiO₂.

A kinetic study of BAC release from BAC-SiO₂ into an aqueous solution in static conditions indicates that the release rate strongly depends on the solution's pH. Controlled release of drugs in physiological conditions (*e.g.*, human body) is of particular interest since the intercellular pH of healthy human tissues is 6.8-7.2, but decreases to a value of *ca.* 5 or lower in presence of inflammation, around tumor sites, or at specific areas of the body (*e.g.*, endosomes, lysosomes, stomach).²⁸

BAC release studies at low pH values (*e.g.*, 1-2) were unsuccessful and a great deal of effort was directed towards identification of an appropriate release medium, as well as BAC concentration measurement. *In situ* concentration measurements using UV-Vis or conductivity instruments failed due to interference from the particles or inability to

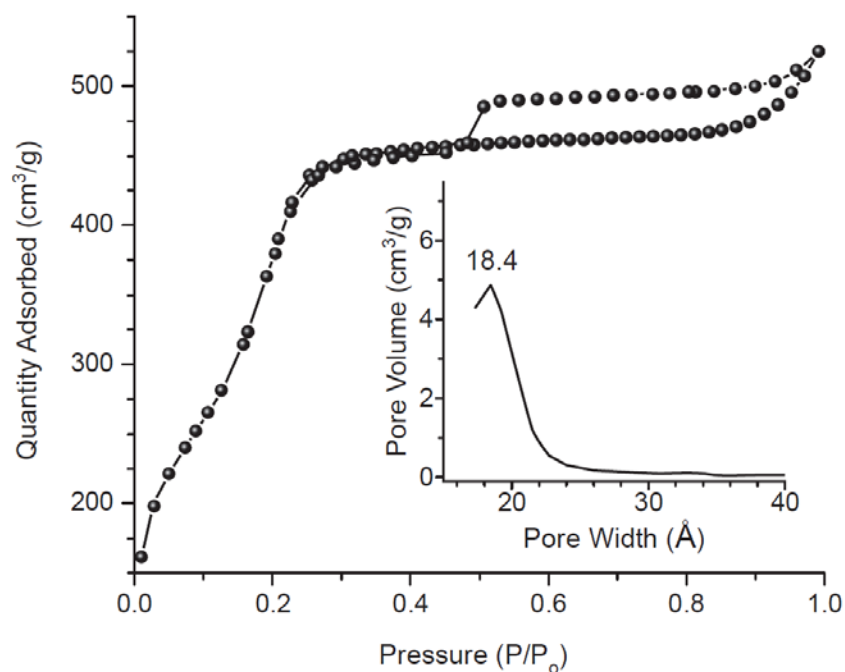


Figure 2.7. Nitrogen (77 K) sorption isotherms of calcined BAC-SiO₂ and pore size distribution shown in inset.

correlate the measurements to free BAC molecules concentration, respectively. It is proposed herein that the dispersion of cleaved framework particles with a size on the order of UV-Vis wavelength (*i.e.*, 300-800 nm) caused elastic scattering and interfered with the UV-Vis measurements. This interference of silica nanoparticles was also reported elsewhere.²⁹ Incorporation of several consecutive centrifugation steps was necessary to accurately measure the concentration at $\lambda_{\text{max}} = 262$ nm. BAC exhibits three predominant UV-Vis absorption peaks in the range of 240-280 nm (Figure 2.8) which are proposed herein to originate from benzene's $\pi \rightarrow \pi^*$ electronic excitations. The $\lambda_{\text{max}} = 262$ nm is reasonable if considering λ_{max} of toluene at 261 nm with a bathochromic effect caused by the apparently weak inductive effect of the relatively distant cationic substituent.

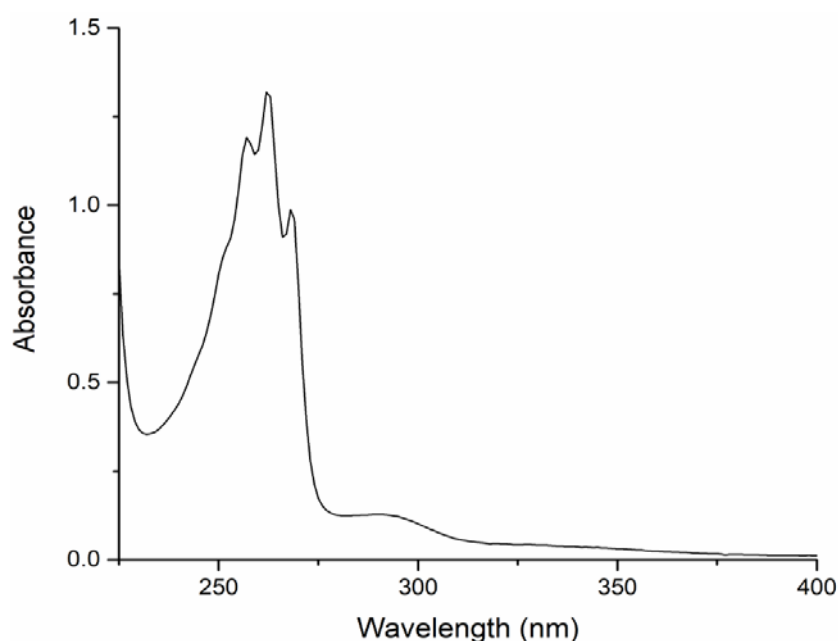


Figure 2.8. UV-Vis spectrum of BAC in a quartz cuvette (shown is a portion of the 200-800 nm scan)

In solutions with pH of 7.4, only 2.5 % of the encapsulated BAC was released from BAC-SiO₂ within 2-3 days (Figure 2.9a). Upon decreasing pH to 4.0, a larger portion of BAC (8.0 %) was released within the same time frame. These findings are in agreement with the drug release kinetics data for MSNs reported in literature.^{9,30,31} The increase in BAC release can be largely attributed to the replacement of cationic BAC with H⁺ ions at the Si-O⁻ sites. Drug release profiles (Figure 2.9a) suggest that the amount of BAC released is pH dependent in pH range of 4.0 – 7.4. It is important to note that although the majority (*ca.* 93 %) of the BAC remained within the particles, a second release profile (not shown) indicated an additional 4.5 % of BAC was released upon placing the particles in a fresh solution with pH 4.0. This suggested that the BAC could be continuously released from BAC-SiO₂ in physiologically-relevant dynamic conditions.

In order to investigate the mechanism of BAC release, the *in vitro* drug release data was analyzed using the power law (Korsmeyer-Peppas) model (Equation 1).^{21,32} This model, based on Fick's second law of diffusion, depicts drug release from with the assumption that the diffusion coefficient is concentration independent and the drug is homogeneously distributed throughout the drug delivery system. The general form is:

$$\frac{M_t}{M_\infty} = kt^n \quad (\text{Equation 2.2})$$

where M_t and M_∞ are the cumulative amounts of released BAC at time t and infinity, respectively; n is the release exponent that characterizes the desorption mechanism; and k is the kinetic constant which correlates directly with the diffusion coefficient, D , if a

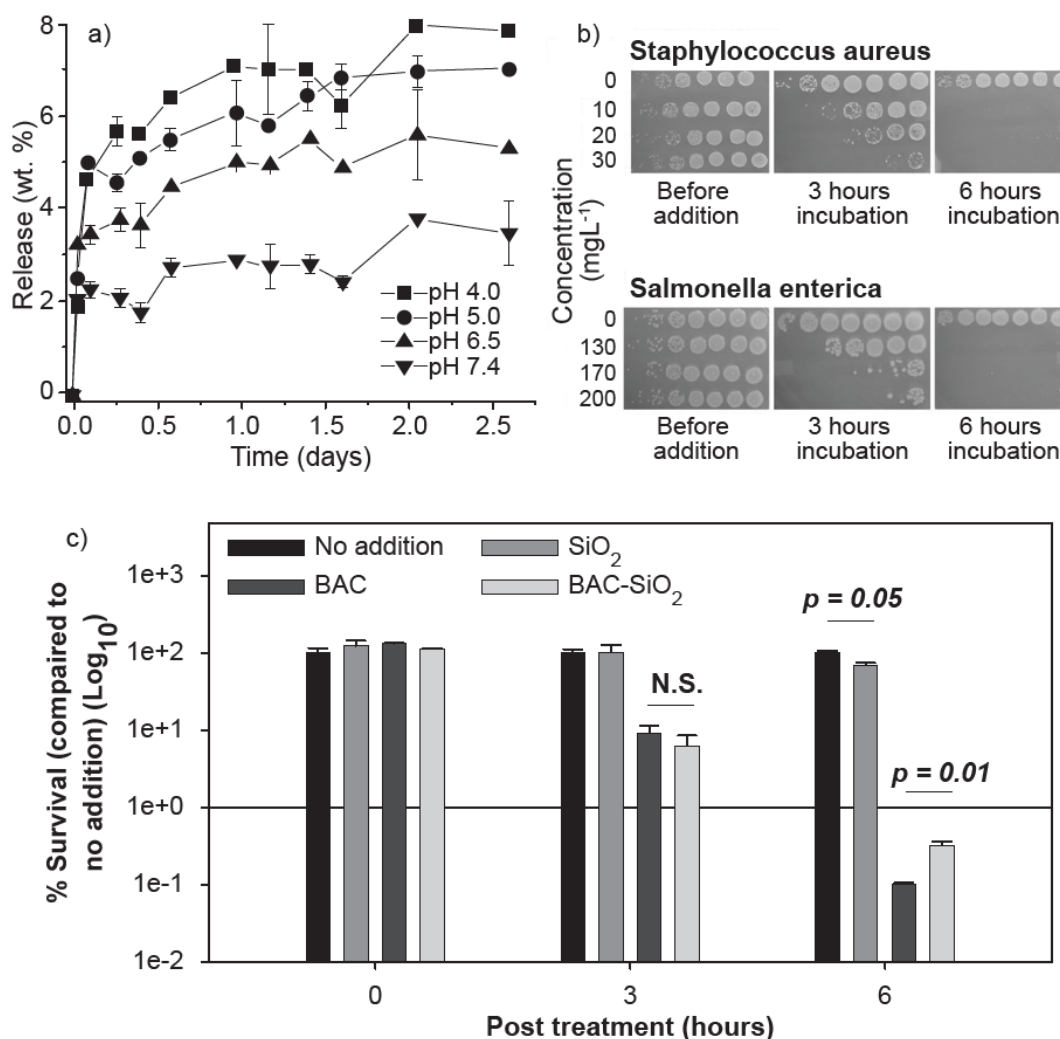


Figure 2.9. (a) Release profile of BAC from BAC-SiO₂ in PBS solution at pH 4.0, 5.0, 6.5, and 7.4 along with the corresponding standard deviation. (b) Time and dose-dependent killing of *S. aureus* and *S. enterica* by BAC-SiO₂. Photograph display of drop plates containing 10-fold serial dilutions (right to left: 10⁰ to 10⁻⁶) of treated cultures. (c) The percentage of *S. aureus* survival upon exposure to 12 mg L⁻¹ SiO₂, 4 mg L⁻¹ BAC, or 10 mg L⁻¹ BAC-SiO₂ for 0, 3, and 6 h is shown. Bacterial killing is monitored in triplicates. The average survival is displayed, in which error bars denote standard deviations. Statistical significance is calculated using a two-tailed t-test with significant p-values shown. “N.S.” denotes “not significant.”

constant thickness of the diffusion path is assumed.^{33,34} Although the values of n are geometry dependent, the same BAC-SiO₂ material was used for the release experiments, eliminating the geometry variable. A plot of $\log(M_t/M_\infty)$ as a function of $\log(t)$, with $t \leq 62$ h in pH 4.0 and 7.4, (Figures 2.10-2.12) yielded n values shown in Table 2.1.

Comparison of n values indicated that there were at least two processes that could govern the release of BAC from the silica particles. In phosphate-buffered saline (PBS) pH 7.4, $n = 0.7$, which is indicative of non-Fickian diffusion with a superposition of framework swelling or erosion.²¹ However, in HCl solution, pH 4.0, $n = 0.2$, which suggests non-Fickian diffusion from disordered pores with respect to shape, length, and size.^{17,21} It is noteworthy that the dependence of n values to the release should, in reality, comprise several superimposed processes. For example, penetration of water into the particles is present in both release media, but it is more profound in PBS.

Kinetic analysis was conducted *via* Power law model (Equations 2.2 – 2.6), which is used widely in the literature.^{17,21,35,36}

$$\rightarrow \log \frac{M_t}{M_\infty} = \log k t^n \quad (\text{Equation 2.3})$$

$$\rightarrow \log \frac{M_t}{M_\infty} = \log k + \log t^n \quad (\text{Equation 2.4})$$

$$\rightarrow \log \frac{M_t}{M_\infty} = \log k + n \log t \quad (\text{Equation 2.5})$$

$$\rightarrow \log \frac{M_t}{M_\infty} (y) = \log k (\text{constant } b) + n \log t (x); [y = nx + b] \quad (\text{Equation 2.6})$$

M_t/M_∞ is a fraction of drug released at time t , k is the release rate constant and n is the release exponent. The n value is used to determine the release mechanism; n and k can be calculated from slope and intercept, respectively.

Table 2.1. Analysis of kinetic data for BAC desorption

Release Media	pH	$\log (M_t/M_\infty)$ vs. $\log (t)$	n	R
PBS	7.4	$y = 0.702x - 1.0$	0.702 ± 0.06	0.95
HCl	4.0	$y = 0.208x - 0.3$	0.208 ± 0.03	0.94

Kinetic modeling of the release data (Figures 2.10-2.12) demonstrated that the release mechanism in a solution with pH 7.4 versus that with pH 4.0 was different. The proposition of different mechanisms responsible for BAC release in the aforementioned media was reasonable due to the vast differences in the release environment. At pH 7.4, an environment representative of extracellular healthy tissues and blood, there is an excess of OH^- relative to H_3O^+ ions. Thus, the excess OH^- ions have the capacity to deprotonate some of the silanol ($-\text{Si}-\text{OH}$) groups and even hydrolyze some of the siloxanes. On the other hand, at pH 4.0 the environment is moderately acidic, and thus, the electrostatically-bound BAC templates can be liberated by ion exchange with another cation (*e.g.*, H^+). Many studies report that the pK_a of silanol groups is *ca.* 4-5.^{37,38} Additionally, acid-catalyzed condensation of two silanol groups, which reduces silanol groups, occurs concomitantly with the release of the cationic BAC surfactants.

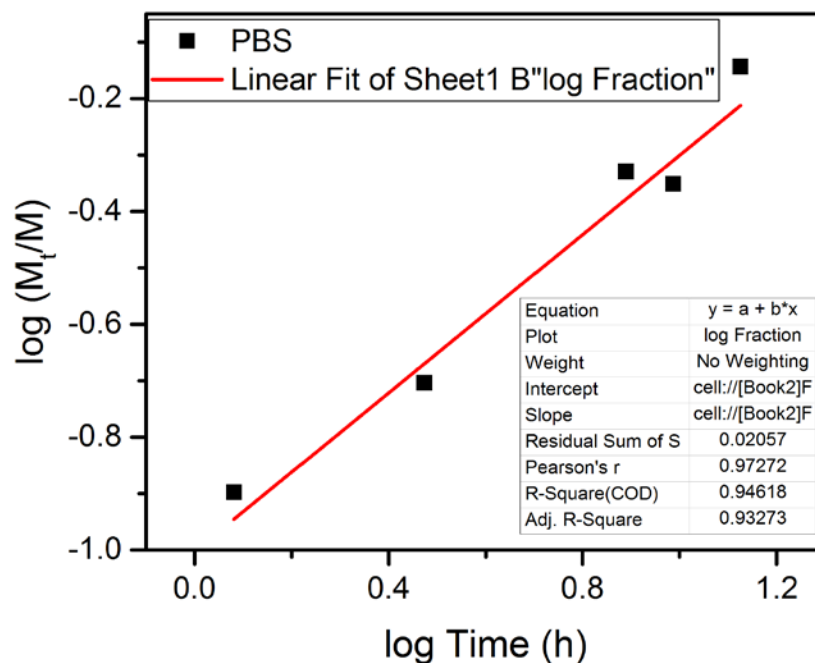


Figure 2.10. Logarithmic variation of BAC fraction released over time in PBS pH 7.4.

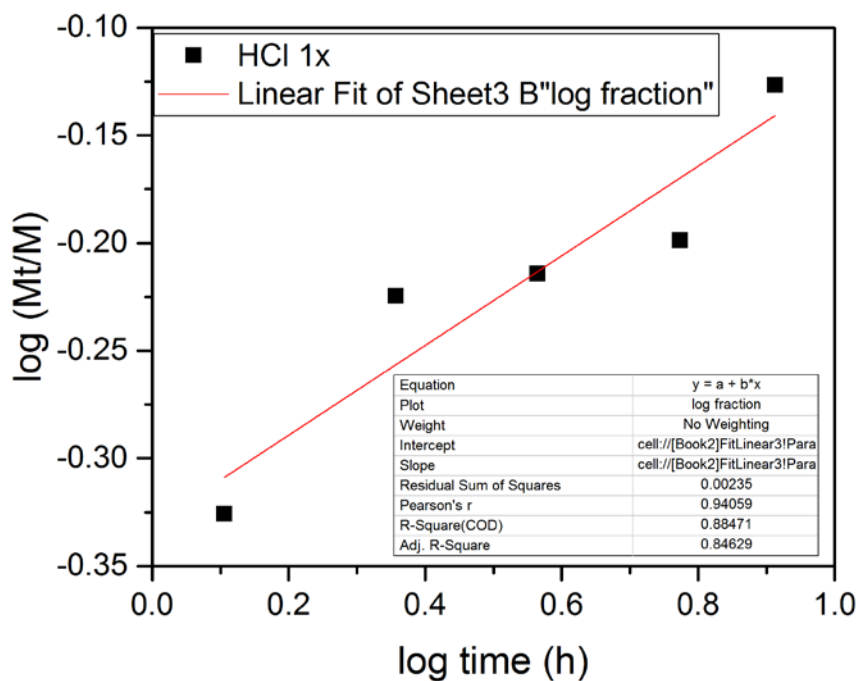


Figure 2.11. Logarithmic variation of BAC fraction released over time in HCl pH 4.0.

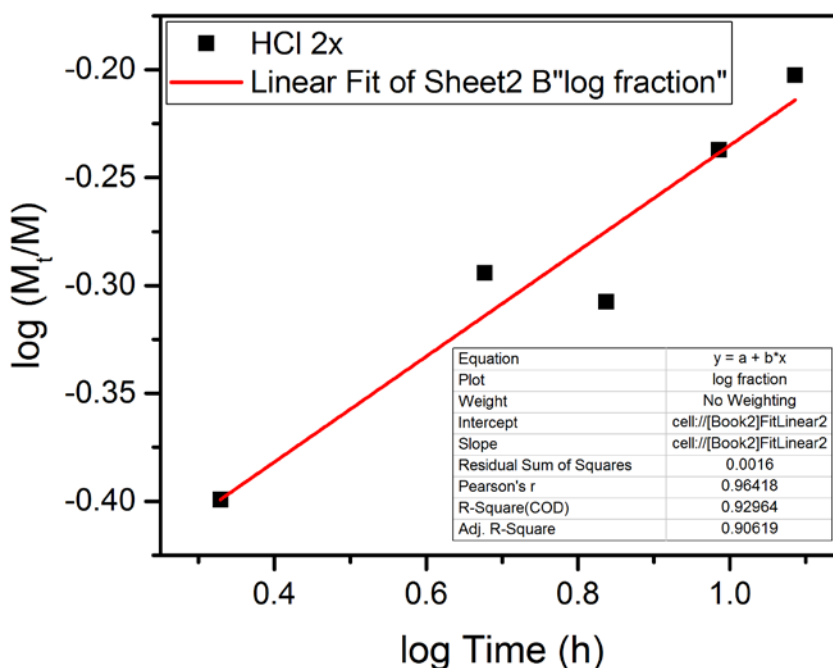


Figure 2.12. Logarithmic variation of BAC fraction released over time for the second release in a fresh solution of HCl pH 4.0.

Since surfactant-extracted MSNs have proven to exhibit a remarkably faster degradation rate in simulated body fluid,³⁹ it is proposed that the materials synthesized herein will continue to release the drug. Additionally, as the material is not calcined, the density of surface silanols is conserved, which can be further modified or otherwise used to help the particles interact with microbes. Indeed, BAC-SiO₂ exposure resulted in a time- and concentration-dependent killing of the gram-positive *S. aureus* and the gram-negative *S. enterica* human bacterial pathogens (Figure 2.9b). Similar findings have been reported for BAC and are most likely the result of the outer membrane of *E. coli* providing additional protection from exposure.^{40,41} Importantly, SiO₂ had no effect on bacterial viability while BAC-SiO₂ displayed similar killing as pure BAC, when the

amount of BAC present in the BAC-SiO₂ was taken into consideration (BAC-SiO₂ was 40% BAC by weight as tested) (Figure 2.9c). These results suggest that a) the addition of BAC-SiO₂ to liquid growth medium results in BAC release leading to bacterial killing and b) BAC-SiO₂ is as effective at killing *S. aureus* as pure BAC.

BAC-SiO₂ showed antibacterial activity against *S. aureus* at concentrations as low as 10 mg L⁻¹ (Figure 2.9b). Taking into account that the amount of BAC within the material is *ca.* 40% and assuming the maximum release within the observed timeframe (*i.e.*, 6 hrs) is 10%, this results in a 10-fold reduction of MIC as compared to literature reported values of *ca.* 40 mg L⁻¹.⁴²

It was postulated that one of the precursors (*e.g.*, NH₄OH) may be remaining in the as-synthesized BAC-SiO₂ material to a significant extent and is causing the observed enhancement of antimicrobial activity. Although the as-synthesized BAC-SiO₂ material was washed with copious amounts of water after the collection of the powder and prior to conducting the antimicrobial assays, it was necessary to exclude the possibility that the additional antimicrobial effect was attributed to chemi- or physisorbed NH₃ which is known to demonstrate cytotoxicity in a variety of biological organisms including animals and plants.⁴³⁻⁴⁵ A series of experiments (Figures 2.13-2.15) were conducted to determine whether any of the chemicals present during the synthesis had any significant effect on the antimicrobial activity.

The concentration of BAC-SiO₂ used for antimicrobial assays illustrated in Figures 2.9b-c ranged between 0-200 mg L⁻¹. Accordingly, aqueous solutions comprising the as-synthesized BAC-SiO₂ material were prepared at concentrations ranging 60-400

mg L⁻¹ in 0.1 M NaCl. The pH measurements of the 0.1 M NaCl solution and BAC-SiO₂ solutions were 6.10 and 5.65 ± 0.22 , respectively (Figure 2.13). The reduction in pH value upon addition of BAC-SiO₂ suggests that the as-synthesized material is overall slightly acidic. It is noteworthy that a strong alkaline effect was not observed in this experiment, which would indicate a reasonable amount of excess NH₃ or its hydrolysate NH₄OH. Notably, based on the reagents used during the synthesis, there are only several major species that can contribute to the pH in these solutions:

1. Deprotonation of Si-OH and hydrolysis of Si-O-Si moieties;
2. Possible residual NH₃ and/or NH₄OH; and
3. Hydrolysis of benzalkonium (RNH₄⁺) ions (which leads to acidic solution as per the following two reactions: $\text{RNH}_4^+ + \text{H}_2\text{O} \rightleftharpoons \text{RNH}_4\text{OH} + \text{HCl}$ and $\text{HCl} + \text{H}_2\text{O} \rightarrow \text{H}_3\text{O}^+(\text{aq}) + \text{Cl}^-(\text{aq})$)

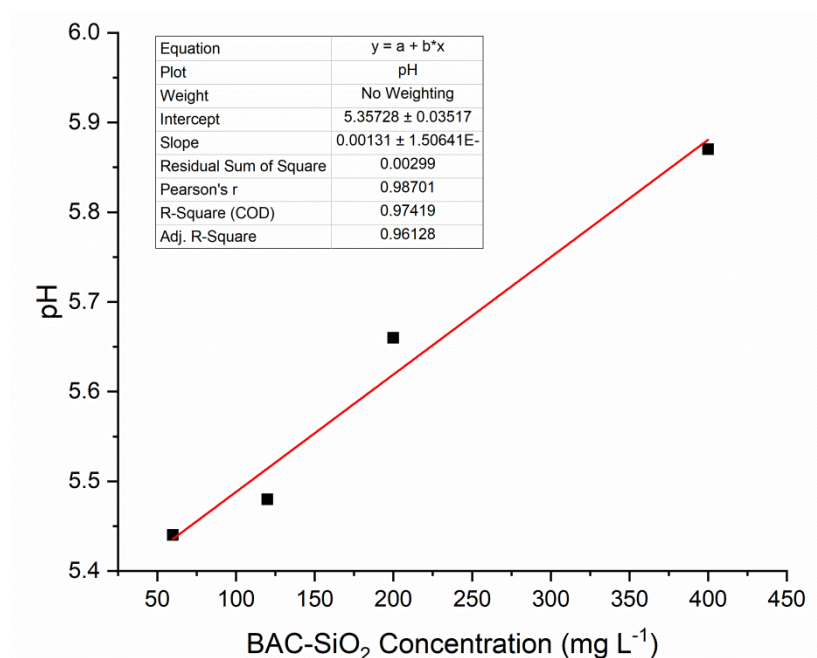


Figure 2.13. pH measurements plotted against the concentration of BAC-SiO₂.

Chloride ions can be ignored due to their negligent alkalinity. In this case, since the pH is less than 7 and the pH is lower than that of the pure solvent environment, it is reasonable to postulate that the acidic species (*e.g.*, benzalkonium cations, NH_4^+ , and Si-OH) overpower the alkaline species (*e.g.*, NH_3 , Si-O-Si) in terms of pH effect. Since the antimicrobial assays were carried out in buffered media, we expect a similar pH effect, but to a lesser extent due to the buffering effect.

Besides pH measurements, additional biological control experiments were conducted using NH_4OH . At the concentrations examined, NH_4OH had no effect on *S. aureus* or *S. enterica* growth (Figure 2.14) and the viability of the microbes (Figure 2.15). As illustrated in the figures, the microbial growth and proliferation rates cannot be discerned from the samples containing 30 or 200 mg L^{-1} NH_4OH and the blank control. The concentrations of 30 and 200 mg L^{-1} NH_4OH were chosen as to demonstrate that even if 100% of the BAC-SiO₂ consisted of NH_4OH , it would not demonstrate any bacteriostatic or bactericidal effect.

These results are also consistent with those previously reported in the literature. As previously mentioned, the cytotoxicity of ammonia has been evaluated on a variety of biological organisms. It was demonstrated that in contrast to animal and plant cells, ammonia was not toxic for various bacteria strains such as *C. glutamicum*, *E. coli*, and *B. subtilis* even in molar concentrations.⁴⁶

Based on these results, it is proposed that the reason for the as-synthesized BAC-SiO₂ to show a significantly enhanced antibacterial effect as compared to free BAC, despite the former having the capability to release less BAC into the solution, is because the as-synthesized BAC-SiO₂ helps make the BAC more accessible to the microbes. It is

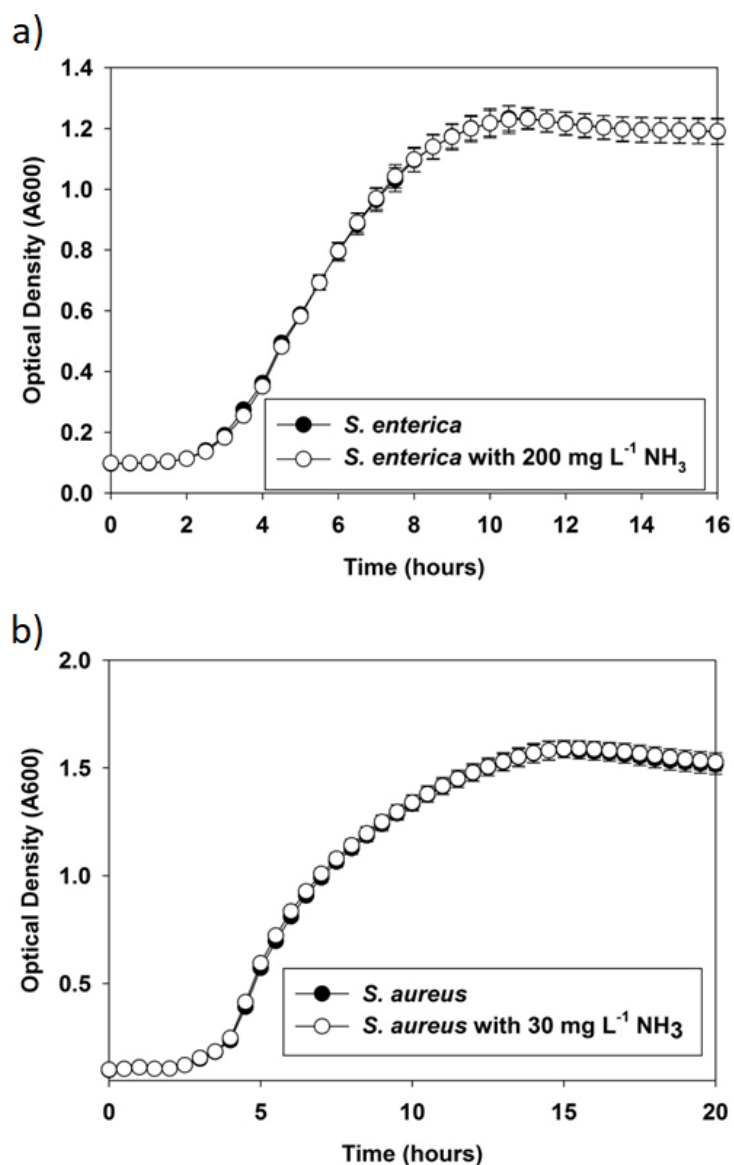
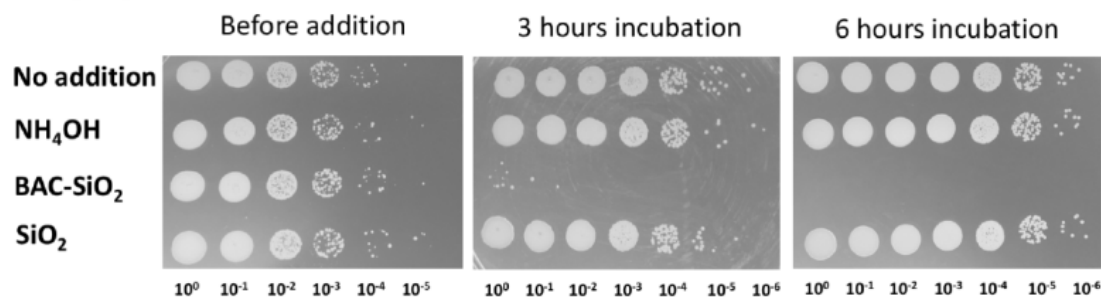


Figure 2.14. Growth analyses of (a) *S. enterica* and (b) *S. aureus* in the presence of NH₄OH. Data represents growth traces. The concentrations of NH₄OH was 200 mg L⁻¹ and 30 mg L⁻¹ for *S. enterica* and *S. aureus*, respectively. Experiments were conducted in triplicate and error bars represent standard deviation. Error bars are shown for all data points, but are sometimes too small to visualize.

Staphylococcus aureus



Salmonella enterica

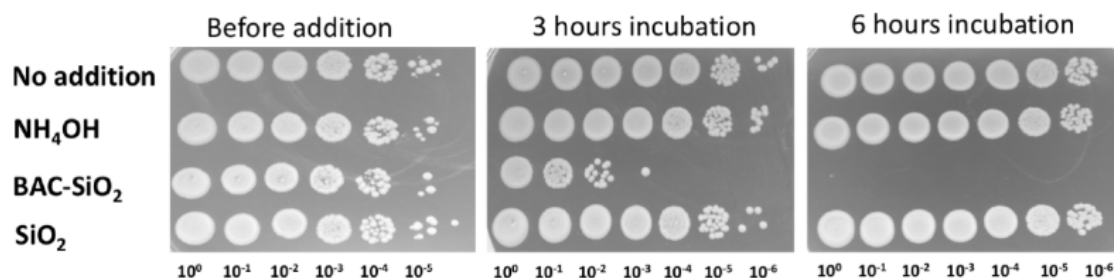


Figure 2.15. Time- and dose-dependent killing of *S. aureus* and *S. enterica* by NH₄OH, BAC-SiO₂, or SiO₂. The concentrations of all additions were 30 mg L⁻¹ and 200 mg L⁻¹ for *S. aureus* and *S. enterica*, respectively. Photographs display drop plates containing 10-fold serial dilutions of treated cultures.

possible that releasing the BAC in a localized manner on the cell surface or a Trojan Horse mode of action (where the silica particles are engulfed by the bacteria with subsequent drug release inside the organism) may result in significantly more efficacious antibacterial effect. This possibility is not unprecedented and it is known that the biological activities (such as antibacterial or anticancer effects) of many small molecules and ions are enhanced by nanoparticles. For example, related bioactive-loaded silica-based nanoporous materials (*e.g.*, xerogels) are reported to show higher antibacterial

potency than the same amount of free bioactive molecules.^{47,48} This has also been previously reported for anticancer drugs.⁴⁹

2.5. Conclusion

The development of novel bioactive advanced functional materials is imperative to support the innovation of the global healthcare industry. As antimicrobial resistance continues to threaten the effective prevention and treatment of bacteria, parasites, viruses and fungi, the need for more efficient and advanced treatments warrants significant research. Quaternary ammonium surfactants are a class of antimicrobial agents with a good affinity for microbial cell membrane lipid bilayer and exhibit low minimum bactericidal concentrations (MBC). However, controlled drug delivery of these molecules to targeted cells is required to prevent the inadvertent inactivation thereof in the presence of suitable anionic molecules, phospholipids, and other molecules that either neutralize the bactericide or protect the microbes. It is therefore highly desirable to develop novel technologies to enhance the selectiveness and reduce unwanted inactivation of bactericidal quaternary ammonium compounds (QACs).

In the current work, we report a novel organic-inorganic hybrid material demonstrating prolonged and pH-triggered release of benzalkonium chloride (BAC), an antimicrobial agent. The synthetic route combines the advantages of incorporating the drug into the host without post-treatment, targeted pH-responsive controlled release of the drug, and fabrication of high surface area mesoporous silica, upon removal of the template, suitable as an inorganic host material for a broad range of applications.

Moreover, a thermal degradation pathway of the template within the framework was proposed, which was found to significantly differ from that of the free template molecule.

Utilization of a wide array of analytical instruments indicated that the synthesized material comprises a high density (0.56 g per 1 g SiO₂) of BAC and a relatively high surface area ($> 1500 \text{ m}^2 \text{ g}^{-1}$) upon removal of the drug template. Thermal degradation of the drug within the framework follows a different pathway than the free drug molecule. Analytical results demonstrated an additional degradation step, which comprises the aliphatic moieties exclusively at 300-340 °C. Drug release measurements indicate that BAC release is preferential to environments with a high density of hydronium ions, which presumably displace the drug from the anionic silanol sites. In the best case scenario, the synthesized material exhibited a bactericidal effect just three hours after incubation for both strains of bacteria. Moreover, a correlation of drug release profiles with the time-dependent antimicrobial assay indicates BAC can kill *S. aureus* at sub-ppm concentrations, which is lower than the reported MIC and MBC values in the literature. This observed phenomenon supports previously reported theories that the drug may not need to completely release into the bulk solution in order to interact with microbes. The synthetic approach can be extended to a variety of drugs to realize advanced functional biomaterials.

2.6. References

- (1) Wan, Y.; Zhao, On the controllable soft-templating approach to mesoporous silicates. *Chem. Rev.* **2007**, *107* (7), 2821-2860.
- (2) Tang, F.; Li, L.; Chen, D., Mesoporous silica nanoparticles: Synthesis, biocompatibility and drug delivery. *Adv. Mater.* **2012**, *24* (12), 1504-1534.
- (3) Joo, S. H.; Park, J. Y.; Tsung, C.-K.; Yamada, Y.; Yang, P.; Somorjai, G. A., Thermally stable Pt/mesoporous silica core-shell nanocatalysts for high-temperature reactions. *Nat. Mater.* **2009**, *8* (2), 126-131.
- (4) Feng, X.; Fryxell, G. E.; Wang, L. Q.; Kim, A. Y.; Liu, J.; Kemner, K. M., Functionalized monolayers on ordered mesoporous supports. *Science* **1997**, *276* (5314), 923.
- (5) Yantasee, W.; Fryxell, G. E.; Conner, M. M.; Lin, Y., Nanostructured electrochemical sensors based on functionalized nanoporous silica for voltammetric analysis of lead, mercury, and copper. *J. Nanosci. Nanotechnol.* **2005**, *5* (9), 1537-40.
- (6) Wen, J.; Yang, K.; Liu, F.; Li, H.; Xu, Y.; Sun, S., Diverse gatekeepers for mesoporous silica nanoparticle based drug delivery systems. *Chem. Soc. Rev.* **2017**, *46* (19), 6024-6045.
- (7) Zhaowei, C.; Chuanqi, Z.; Enguo, J.; Haiwei, J.; Jinsong, R.; P., B. B.; Xiaogang, Q., Design of surface-active artificial enzyme particles to stabilize pickering emulsions for high-performance biphasic biocatalysis. *Adv. Mater.* **2016**, *28* (8), 1682-1688.
- (8) Yu, T.; Enguo, J.; Jinsong, R.; Xiaogang, Q., Bifunctionalized mesoporous silica-supported gold nanoparticles: Intrinsic oxidase and peroxidase catalytic activities for antibacterial applications. *Adv. Mater.* **2015**, *27* (6), 1097-1104.
- (9) Vallet-Regi, M.; Rámila, A.; del Real, R. P.; Pérez-Pariente, J., A new property of MCM-41: Drug delivery system. *Chem. Mater.* **2001**, *13* (2), 308-311.
- (10) Lu, J.; Liong, M.; Li, Z.; Zink, J. I.; Tamanoi, F., Biocompatibility, biodistribution, and drug-delivery efficiency of mesoporous silica nanoparticles for cancer therapy in animals. *Small* **2010**, *6* (16), 1794-1805.
- (11) Zhao, Y.; Trewyn, B. G.; Slowing, I. I.; Lin, V. S., Mesoporous silica nanoparticle-based double drug delivery system for glucose-responsive controlled release of insulin and cyclic AMP. *J. Am. Chem. Soc.* **2009**, *131* (24), 8398-8400.
- (12) Moulari, B.; Pertuit, D.; Pellequer, Y.; Lamprecht, A., The targeting of surface modified silica nanoparticles to inflamed tissue in experimental colitis. *Biomaterials* **2008**, *29* (34), 4554-4560.
- (13) Wen, J.; Yang, K.; Xu, Y.; Li, H.; Liu, F.; Sun, S., Construction of a triple-stimuli-responsive system based on cerium oxide coated mesoporous silica nanoparticles. *Sci. Rep.* **2016**, *6*, 38931.
- (14) Wen, J.; Yan, H.; Xia, P.; Xu, Y.; Li, H.; Sun, S., Mesoporous silica nanoparticles-assisted ruthenium(II) complexes for live cell staining. *Sci China: Chem.* **2017**, *60* (6), 799-805.
- (15) Dement'eva, O. V.; Frolova, L. V.; Rudoy, V. M.; Kuznetsov, Y. I., Sol-gel synthesis of silica containers using a corrosion inhibitor, catamine AB, as a templating agent. *Colloid J.* **2016**, *78* (5), 596-601.

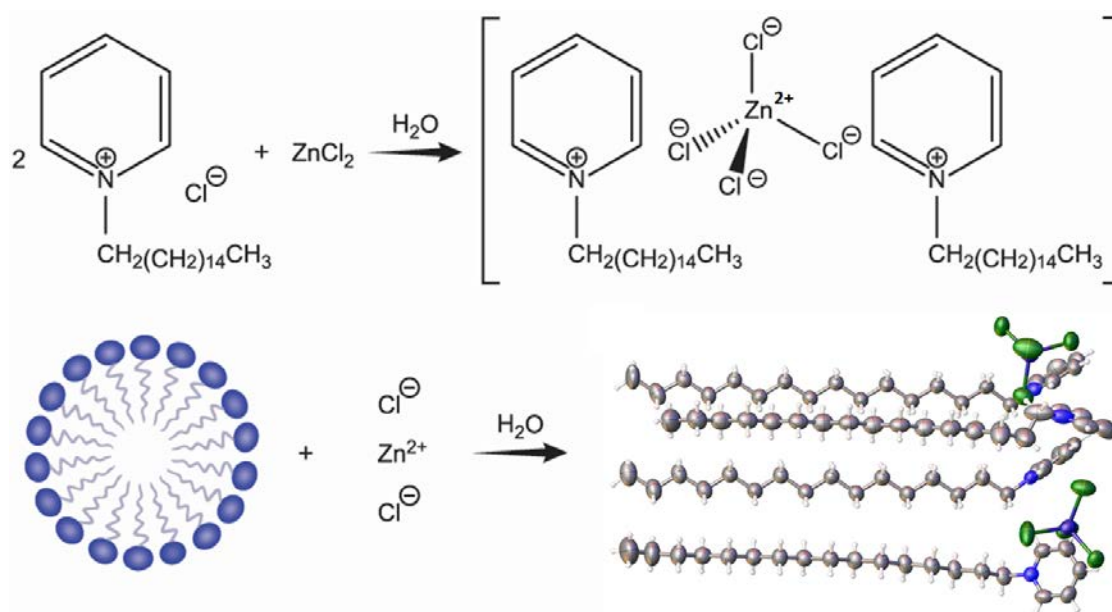
- (16) Dement'eva, O. V.; Roumyantseva, T. B.; Rudoy, V. M., The first example of silica nanoshell synthesis on vesicles of a cationic glycerolipid—potential antitumor drug. *Colloid J.* **2016**, 78 (2), 281-284.
- (17) Dement'eva, O. V.; Senchikhin, I. N.; Kartseva, M. E.; Ogarev, V. A.; Zaitseva, A. V.; Matushkina, N. N.; Rudoy, V. M., A new method for loading mesoporous silica nanoparticles with drugs: Sol–gel synthesis using drug micelles as a template. *Colloid J.* **2016**, 78 (5), 586-595.
- (18) Nandni, D.; Mahajan, R. K., Micellar and interfacial behavior of cationic benzalkonium chloride and nonionic polyoxyethylene alkyl ether based mixed surfactant systems. *J. Surfactants Deterg.* **2013**, 16 (4), 587-599.
- (19) Russel, A. D.; Hugo, W. B.; Ayliffe, G. A. J., *Principles and practice of disinfection, preservation, and sterilization*. 3rd ed.; Blackwell Science, University Press: Cambridge, United Kingdom, 1999.
- (20) Dement'eva, O. V.; Rudoy, V. M., One-pot synthesis and loading of mesoporous SiO₂ nanocontainers using micellar drugs as a template. *RSC Adv.* **2016**, 6 (42), 36207-36210.
- (21) Fidalgo, A.; Lopez, T. M.; Ilharco, L. M., Wet sol–gel silica matrices as delivery devices for phenytoin. *J. Sol-Gel Sci. Technol.* **2009**, 49 (3), 320-328.
- (22) Dement'eva, O. V.; Vinogradova, M. M.; Frolova, L. V.; Ogarev, V. A.; Kuznetsov, Y. I.; Rudoy, V. M., SiO₂-based nanocontainers of a novel type: If the template micelles are functional, why remove them. *Colloid J.* **2014**, 76 (1), 19-24.
- (23) Scherrer, P., *Nachr. Ges. Wiss. Gottingen* **1918**, 26, 98-100.
- (24) Langford, J. I.; Wilson, A. J. C., Scherrer after sixty years: A survey and some new results in the determination of crystallite size. *J. Appl. Crystallogr.* **1978**, 11 (2), 102-113.
- (25) Brunauer, S.; Emmett, P. H.; Teller, E., Adsorption of gases in multimolecular layers. *J. Am. Chem. Soc.* **1938**, 60 (2), 309-319.
- (26) Barrett, E. P.; Joyner, L. G.; Halenda, P. P., The determination of pore volume and area distributions in porous substances. I. Computations from nitrogen isotherms. *J. Am. Chem. Soc.* **1951**, 73 (1), 373-380.
- (27) Kruk, M.; Jaroniec, M., Gas adsorption characterization of ordered organic–inorganic nanocomposite materials. *Chem. Mater.* **2001**, 13 (10), 3169-3183.
- (28) Nazir, S.; Hussain, T.; Ayub, A.; Rashid, U.; MacRobert, A. J., Nanomaterials in combating cancer: Therapeutic applications and developments. *Nanomedicine* **2014**, 10 (1), 19-34.
- (29) Selvaggi, R.; Tarpani, L.; Santuari, A.; Giovagnoli, S.; Latterini, L., Silica nanoparticles assisted photodegradation of acridine orange in aqueous suspensions. *Appl. Catal. B Environ.* **2015**, 168 (Supplement C), 363-369.
- (30) Song, S. W.; Hidajat, K.; Kawi, S., Functionalized SBA-15 materials as carriers for controlled drug delivery: Influence of surface properties on matrix–drug interactions. *Langmuir* **2005**, 21 (21), 9568-9575.
- (31) Ng, J. B. S.; Kamali-Zare, P.; Brismar, H.; Bergström, L., Release and molecular transport of cationic and anionic fluorescent molecules in mesoporous silica spheres. *Langmuir* **2008**, 24 (19), 11096-11102.

- (32) Qu, F.; Zhu, G.; Lin, H.; Sun, J.; Zhang, D.; Li, S.; Qiu, S., Drug self-templated synthesis of ibuprofen/mesoporous silica for sustained release. *Eur. J. Inorg. Chem.* **2006**, (19), 3943-3947.
- (33) Peppas, N., *Pharm. Acta Helv.* **1985**, 60.
- (34) Peppas, N.; Korsmeyer, R.W., *Hydrogels in medicine and pharmacy*. CRC Press: Boca Raton, 1986; Vol. 3.
- (35) Dash, S.; Murthy, P. N.; Nath, L.; Chowdhury, P., Kinetic modeling on drug release from controlled drug delivery systems. *Acta Pol. Pharm.* **2010**, 67 (3), 217-23.
- (36) Costa, P.; Sousa Lobo, J. M., Modeling and comparison of dissolution profiles. *Eur. J. Pharm. Sci.* **2001**, 13 (2), 123-133.
- (37) Leung, K.; Nielsen, I. M. B.; Criscenti, L. J., Elucidating the bimodal acid–base behavior of the water–silica interface from first principles. *J. Am. Chem. Soc.* **2009**, 131 (51), 18358-18365.
- (38) Sulpizi, M.; Gaigeot, M.-P.; Sprik, M., The silica–water interface: How the silanols determine the surface acidity and modulate the water properties. *J. Chem. Theory Comput.* **2012**, 8 (3), 1037-1047.
- (39) He, Q.; Shi, J.; Zhu, M.; Chen, Y.; Chen, F., The three-stage in vitro degradation behavior of mesoporous silica in simulated body fluid. *Micropor. Mesopor. Mat.* **2010**, 131 (1), 314-320.
- (40) Morrissey, I.; Oggioni, M. R.; Knight, D.; Curiao, T.; Coque, T.; Kalkanci, A.; Martinez, J. L.; B. C., Evaluation of epidemiological cut-off values indicates that biocide resistant subpopulations are uncommon in natural isolates of clinically-relevant microorganisms. *PLOS ONE* **2014**, 9 (1), e86669.
- (41) Furi, L.; Ciusa, M. L.; Knight, D.; Di Lorenzo, V.; Tocci, N.; Cirasola, D.; Aragonés, L.; Coelho, J. R.; Freitas, A. T.; Marchi, E.; Moce, L.; Visa, P.; Northwood, J. B.; Viti, C.; Borghi, E.; Orefici, G.; Consortium, B.; Morrissey, I.; Oggioni, M. R., Evaluation of reduced susceptibility to quaternary ammonium compounds and bisbiguanides in clinical isolates and laboratory-generated mutants of *Staphylococcus aureus*. *Antimicrob. Agents Chemother.* **2013**, 57 (8), 3488-3497.
- (42) Fazlara, A.; Ekhtelat, M., The disinfectant effects of benzalkonium chloride on some important foodborne pathogens. *Am. Eurasian J. Agric. Environ. Sci.* **2012**, 12 (1), 23-29.
- (43) Martinelle, K.; Haggstrom, L., Mechanisms of ammonia and ammonium ion toxicity in animal cells: Transport across cell membranes. *J. Biotechnol.* **1993**, 30 (3), 339-350.
- (44) Rogato, A.; D'Apuzzo, E.; Chiurazzi, M., The multiple plant response to high ammonium conditions: the Lotus japonicas AMT1; 3 protein acts as a putative transceptor. *Plant Signal. Behav.* **2010**, 5 (12), 1594-1596
- (45) Wang, T.; Suzuki, K.; Kakisaka, K.; Onodera, M.; Sawara, K.; Takikawa, Y., L-carnitine prevents ammonia-induced cytotoxicity and disturbances in intracellular amino acid levels in human astrocytes. *J. Gastroenterol. Hepatol.* **2019**, 34 (7), 1249-1255.
- (46) Muller, T.; Walter, B.; Wirtz, A.; Burkovski, A., Ammonium toxicity in bacteria. *Curr. Microbiol.* **2006**, 52, 400-406

- (47) Seleem, M. N.; Munusamy, P.; Ranjan, A.; Alqublan, H.; Pickrell, G.; Sriranganathan, N., Silica-antibiotic hybrid nanoparticles for targeting intracellular pathogens. *Antimicrob. Agents Chemother.* **2009**, *53* (10), 4270-4274
- (48) Miller, K.; Wang, L.; Benicewicz, B.; Decho, A., Inorganic nanoparticles engineered to attack bacteria. *Chem. Soc. Rev.* **2015**, *44*, 7787-7807
- (49) Tao, Z.; Toms, B.; Goodisman, J.; Asefa, T., Mesoporous silica microparticles enhance the cytotoxicity of anticancer platinum drugs. *ACS Nano* **2010**, *4* (2), 789-794

CHAPTER 3

Synthesis, Characterization, and Investigation of the Antimicrobial Activity of Cetylpyridinium Tetrachlorozincate



3.1. Overview

Cetylpyridinium tetrachlorozincate (referred to herein as $(\text{CP})_2\text{ZnCl}_4$) was synthesized and its solid-state structure was elucidated *via* single crystal X-ray diffraction (SC-XRD) revealing a stoichiometry of $\text{C}_{42}\text{H}_{76}\text{Cl}_4\text{N}_2\text{Zn}$ with two cetylpyridinium (CP) cations per $[\text{ZnCl}_4]^{2-}$ tetrahedra. Crystal structures at 100 K and 298 K exhibited a zig-zag pattern with alternating alkyl chains and zinc units. The material showed potential for application as a broad spectrum antimicrobial agent, to reduce volatile sulfur compounds (VSCs) generated by bacteria, and in the fabrication of advanced functional materials. Minimum inhibitory concentration (MIC) of $(\text{CP})_2\text{ZnCl}_4$ was 60, 6, and 6 $\mu\text{g mL}^{-1}$ for *Salmonella enterica*, *Staphylococcus aureus*, and *Streptococcus mutans*, respectively.

The MIC values of $(\text{CP})_2\text{ZnCl}_4$ were comparable to that of pure cetylpyridinium chloride (CPC), despite the fact that approximately 16% of the bactericidal CPC is replaced with bacteriostatic ZnCl_2 in the structure. A modified layer-by-layer deposition technique was implemented to synthesize mesoporous silica (*i.e.*, SBA-15) loaded with approximately 9.0 wt.% CPC and 8.9 wt.% Zn.

3.2. Introduction

Cetylpyridinium chloride is a quaternary ammonium compound with broad spectrum antimicrobial activity. Its antimicrobial properties render it useful in a variety of applications including cosmetics, pharmaceuticals, and water treatment.^{1,2} CPC is recognized as safe for dermal and oral applications by the Food and Drug Administration (FDA), and is commonly known for its role in the prevention and treatment of dental plaque, gingivitis, halitosis and calculus in oral care products.^{1,3-7} Zinc (Zn) is utilized in a wide array of industries including food, pharmaceuticals, energy production, material science, physiology, and organic chemistry.⁸⁻¹¹ Existing exclusively as the divalent Zn cation, Zn is an essential nutrient for virtually all living organisms.¹² However, at concentrations higher than those that are physiologically useful, Zn exhibits a bacteriostatic effect on many microorganisms.¹³

The antibacterial property of Zn^{2+} ions has been attributed to five main mechanisms: (1) the disruption of cell membrane integrity, (2) the denaturation of proteins, (3) the production of reactive oxygen species resulting in cellular damage, (4) the interaction with nucleic acids, and (5) the inactivation of iron-sulfur proteins and/or inhibition of the iron-sulfur protein maturation machinery.¹⁴⁻¹⁸ When CPC disrupts the

microbial cell membrane, the positively charged region of CPC binds directly to the polar negatively-charged phosphate groups of phospholipids while the non-polar portion of CPC interacts with non-polar phospholipid tails.^{3,19} This results in permeability of the cell membrane, membrane depolarization, leakage of intracellular components and ultimately death.³ Recent experiments from our group suggest that loading quaternary ammonium compounds (QACs) into mesoporous silica nanoparticles (MSNs) yields a material with excellent antimicrobial activity and a pH-responsive controlled release of the antimicrobial drug.²⁰

Previously, a number of studies have focused on elucidating the interaction between divalent metal (*e.g.*, Cd, Cu, Zn) ions and pyridine analogues; however, these studies were not successful in identifying and realizing an antibacterial technology that is viable, safe, and effective for widespread healthcare use. In 2002, Neve *et al.* synthesized and solved the crystal structure of [C16-Py]₂[CdCl₄].²¹ Application of the material was not evaluated or mentioned beyond their potential to be used as a liquid-crystalline precursor. Furthermore, attempts to crystallize the Zn analogue were futile. Hilp *et al.* proposed the use of cetylpyridinium tetrachlorozincate as titrant for analysis of anionic surfactants.^{22,23} In 2015, Kaur *et al.* synthesized (CP)₂CuCl₄ and (CP)CuCl₃ and demonstrated that the insertion of copper into the CPC moiety enhanced the antibacterial activity as compared to pure CPC.²⁴ Although the antimicrobial properties of copper (Cu) have long been known, the realization of the Cu-cetylpyridinium conjugate technology for healthcare applications would be extremely challenging due to the potential for blue (*e.g.*, Cu²⁺) or yellow (*e.g.*, [CP][CuCl₃] or [CP]₂[CuCl₄]) staining associated with the d-orbital splitting of the copper ion.

In the current work, we report the synthesis and characterization of cetylpyridinium tetrachlorozincate as well as its application to reduce volatile sulfur compounds, as an antibacterial active pharmaceutical ingredient (API), and to fabricate advanced functional materials. Work presented suggests that cetylpyridinium tetrachlorozincate is a viable and effective antimicrobial agent to combat the global healthcare issues associated with oral and dermal disease (*e.g.*, hospital infections, medical device biofilms, and antibiotic resistance).

3.3. Experimental Section

3.3.1. Materials, Reagents, and Synthesis of Cetylpyridinium Tetrachlorozincate

Reagent grade anhydrous zinc chloride (ZnCl_2) and CPC were supplied by Sigma-Aldrich (St. Louis, MO). CPC was used in the monohydrate form without further purification. The synthesis entailed preparation of fresh 25 wt.% CPC and 75 wt.% zinc chloride solutions in deionized water. Subsequently, the ZnCl_2 solution was added dropwise to the CPC solution under magnetic stirring. Vacuum filtration and drying of the precipitate yielded an off-white solid which was further purified using acetone extraction. Single crystal was obtained by recrystallizing from acetone.

3.3.2. Instrumentation

X-ray photoemission spectroscopy (XPS) analysis was carried out using a PHI 5000 VersaProbe II scanning XPS microprobe instrument with a monochromatic Al $K\alpha$

X-ray source (1486.6 eV) and 200 μm beam diameter. PHI MultiPak software was used for subsequent data analysis. Fourier-transform infrared (FTIR) spectra were collected using a Bruker Vertex 70 FTIR spectrometer (Bruker Optics, Billerica, MA) equipped with a GladiATR diamond ATR accessory (Pike technologies, Madison, WI). The spectral range was 80-4000 cm^{-1} and a resolution of 4 cm^{-1} was used. All measurements were carried out at room temperature, by spreading several milligrams of as-prepared powder samples, without any additional sample preparation procedures. The single crystal X-ray diffraction (SC-XRD) data were collected using Bruker D8 Venture PHOTON 100 CMOS system equipped with a Cu $K\alpha$ INCOATEC ImuS micro-focus source ($\lambda = 1.54178 \text{ \AA}$). Indexing was performed using *APEX3* (Difference Vectors method).²⁵ Data integration and reduction were performed using SaintPlus 6.01.²⁶ Absorption correction was performed by multi-scan method implemented in SADABS.²⁷ Space group was determined using XPREP implemented in APEX3.²⁵ The structure was solved using SHELXT (direct methods) and was refined using SHELXL-2017²⁸⁻³⁰ (full-matrix least-squares on F^2) through OLEX2³¹ interface program. All non-hydrogen atoms were refined anisotropically. Hydrogen atoms were placed in geometrically calculated positions and were included in the refinement process using riding model. Crystal data and refinement conditions for the as synthesized crystals and the ones collected at room temperature are shown in Table 3.1 and Table 3.2, respectively.

Powder X-ray diffraction (PXRD) data were collected at room temperature using a Bruker D8 Advance theta-2theta diffractometer with copper radiation (Cu $K\alpha$, $\lambda = 1.5406 \text{ \AA}$) and a secondary monochromator operating at 40 kV and 40 mA, whereby samples were measured between 2θ of 2° and 40° at 0.5 s/step and step size of 0.02° .

Small angle X-ray scattering (SAXRD) patterns were obtained by using a Bruker Vantec-500 area detector and a Bruker FR571 rotating-anode X-ray generator operating at 40 kV and 50 mA. The diffraction system was equipped with a 3-circle Azlan goniometer, but the sample was not moved during X-ray data collection. The system used 0.25 mm pinhole collimation and a Rigaku Osmic parallel-mode (*e.g.*, primary beam dispersion less than 0.01° in 2θ) mirror monochromator (Cu K α ; $\lambda = 1.5418\text{\AA}$). Data were collected at room temperature (*ca.* 20 °C) with a sample to detector distance of 26.25 cm. Spatial calibration and flood-field correction for the area detector were performed at this distance prior to data collection. The 2048x2048 pixel images were collected at the fixed detector (2θ) angle of 50 deg for 600 sec with ω step of 0.00 deg. For the intensity versus 2θ plot, a 0.02° step, bin-normalized χ integration was performed on the GADDS frame image.

3.3.3. *In-vitro* Bacteria-generated Volatile Sulfur Compound (VSC) Reduction Experiments

Methyl mercaptan is a representative ingredient of volatile sulfur compound (VSC), which can be used as the marker for the quantitative measurement of mouth odor through gas chromatography-flame photometric detector technology.³² Sample preparation entailed dissolution of the ZnCl₂, CPC, and (CP)₂ZnCl₄ powders to a final concentration of 0.75 wt.%. Hydroxyapatite (HAP) disks were incubated with whole saliva to develop pellicles, followed by the treatment of prepared solutions. After rinsing, the treated disks were transferred to headspace vials and incubated with VSC solution to mimic mouth odor VSC generation. The methyl mercaptan in headspace was measured

through gas chromatography, equipped with a flame photometric detector (GC-FPD) and the results would determine the product efficacy in mouth odor reduction.

3.3.4. Antimicrobial Assays

The bacterial strains used for the study were *Salmonella enterica* Serovar typhimurium LT2,³³ *Staphylococcus aureus* USA300_LAC,³⁴ and *Streptococcus mutans* Clark (ATCC). *S. enterica* and *S. aureus* were cultured in Muller Hinton media (Sigma-Aldrich) and *S. mutans* was cultured in Reinforced Clostridial Media (Oxoid). Stock solutions for ZnCl_2 (500 mg mL^{-1}), CPC (1 mg mL^{-1}), and cetylpyridinium tetrachlorozincate ($(\text{CP})_2\text{ZnCl}_4$; 1 mg mL^{-1}) were prepared by dissolving the compounds in distilled deionized water and filter sterilization prior to use.

Growth analyses were conducted as previously described with slight alterations.²⁰ Single bacterial colonies were inoculated into 2 mL of medium in 10 mL capacity culture tubes. Inoculated cultures of *S. aureus* and *S. enterica* were grown aerobically at 37 °C with shaking at 200 rpm for 24 hours. *S. mutans* was cultured statically for 48 h. End-point Minimum Inhibitory Concentrations (MICs) were determined for ZnCl_2 , CPC and $(\text{CP})_2\text{ZnCl}_4$ using Broth Microdilution Method standard protocol from Clinical and Laboratory Standards Institute.³⁵ Biological triplicate overnight cultures were standardized to 0.5 McFarland standard ($\text{OD}_{600} = 0.1$). MICs were determined in cultures grown in 96 well microtiter plates. One-hundred μL of the standardized culture was sub-cultured into wells containing 100 μL of medium containing antimicrobial compound. Control wells containing 200 μL of media only or media with antimicrobial compound

were used to standardize the data. The microtiter plates were aerobically incubated statically at 37 °C. The optical densities of the *S. aureus* and *S. enterica* cultures were determined after 20 h and *S. mutans* was analyzed after 48 h. Culture optical densities (A_{600}) were determined using Biotek® EPOCH 2 microplate reader.

3.3.5. Synthesis and Loading of Mesoporous Silica Nanoparticles (MSNs)

Pluronic P123, 34% hydrochloric acid, and tetraethyl orthosilicate (TEOS) were supplied by BASF (Ludwigshafen, Germany), Avantor (Allentown, PA), and Sigma-Aldrich (St. Louis, MO), respectively. All materials were used as received without further purification. Santa Barbara Amorphous (SBA-15) type material was synthesized according to conventional methods. Specifically, 4 g of Pluronic P123 was mixed with 104 mL of water and 24 mL of concentrated hydrochloric acid. To this clear solution, 8.53 g of TEOS was added dropwise and subsequently stirred at 40 °C for 24 h. The resulting white powder was filtered, washed with copious amounts of deionized water, and dried at 50 °C overnight. Calcination of the as-synthesized SBA-15 was conducted in air at 550 °C for 6 h with 10 °C/min.

Cetylpyridinium chloride tetrachlorozincate was incorporated into the SBA-15 framework *via* a modified immersion layer-by-layer deposition technique.³⁶ After outgassing the SBA-15 at 100 °C for 2 h under vacuum, 800 mg of the powder was added to 100 g of 10 wt.% aqueous CPC solution with subsequent magnetic stirring for over 1 h to allow diffusion throughout porous framework. The CPC-adsorbed SBA-15 was centrifuged, filtered, and washed with 150 mL of deionized water. Lastly, the powder was washed with 100 g of 10 wt.% $ZnCl_2$ aqueous solution, washed with 150 mL of

deionized water, and dried at 40 °C under vacuum for several days. It is noteworthy that utilization of higher concentrations of CPC and ZnCl_2 solutions failed to yield homogeneous CPC-Zn@SBA-15 powders. SBA-15 was chosen as the porous framework since its pore width can easily accommodate a CPC molecule.

BET surface area and porosity measurements of the SBA-15 mesoporous silica nanoparticles (MSNs) were evaluated using a Surface Area and Porosity Analyzer (Gemini VII, Micromeritics, USA).³⁷ Samples were outgassed at 100 °C overnight under a constant flow of N_2 . Subsequent adsorption measurements were done at 77 K. BJH analysis was used to determine pore size distribution.³⁸

3.4. Results and Discussion

Initial observation of an interaction between CPC and ZnCl_2 was made while attempting to synthesize a deep eutectic solvent *via* anhydrous route. In particular, monohydrate CPC and anhydrous ZnCl_2 powders were combined, mixed, and heated at 90 °C for 24 h. Under these conditions, a translucent, yellow-colored gel material was formed in samples with Zn/CPC ratio of 2 and higher. The material would undergo a phase change below *ca.* 50 °C to form an off-white opaque solid material. In order to improve the homogeneity of the samples, the synthesis was repeated with the addition of 15% water. Subsequent experiments, aimed to develop an aqueous route for the synthesis, demonstrated that a sparingly water-soluble precipitate is formed upon combination of aqueous CPC and ZnCl_2 solutions above a certain threshold concentration. The solubility of the precipitate in water was <1 wt.% at room temperature. The precipitate was collected, washed with copious amounts of water, and

recrystallized from acetone to yield a single crystal adequate for SC-XRD analysis. Dynamic scanning calorimetry (DSC) experiments (Figure 3.1) demonstrated *ca.* 20 °C reduction in the onset temperature of the endothermic melting peak in the synthesized material as compared to pure CPC. These results are consistent with the observed phase transition below *ca.* 50 °C in the gel samples synthesized *via* anhydrous route.

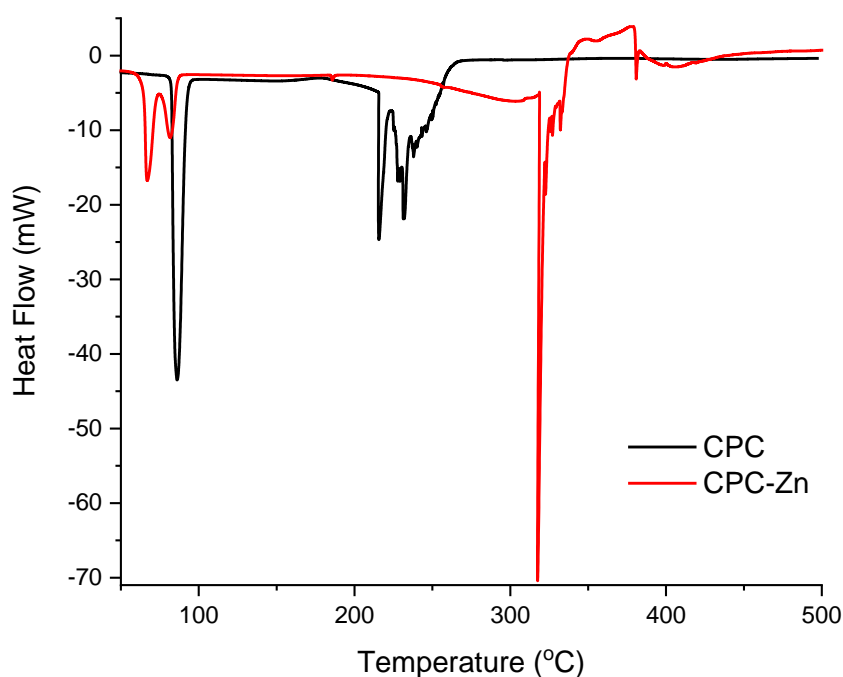


Figure 3.1. DSC plot of CPC and CPC-Zn material.

XPS and FTIR were used to confirm complex formation prior to SC-XRD analyses and therefore referred to as CPC-Zn material. The XPS results (Figures 3.2-3.3) indicate that there is a slight shift in the N^+ peak for CPC-Zn (402.2 eV) material as compared to the CPC (401.8 eV) reference. This may indicate that the electronic environment around the cationic N in the CPC part of the sample has changed compared

to that in CPC alone. It is noteworthy that anhydrous ZnCl_2 cannot easily be analyzed by conventional XPS due to its extreme hygroscopic property.

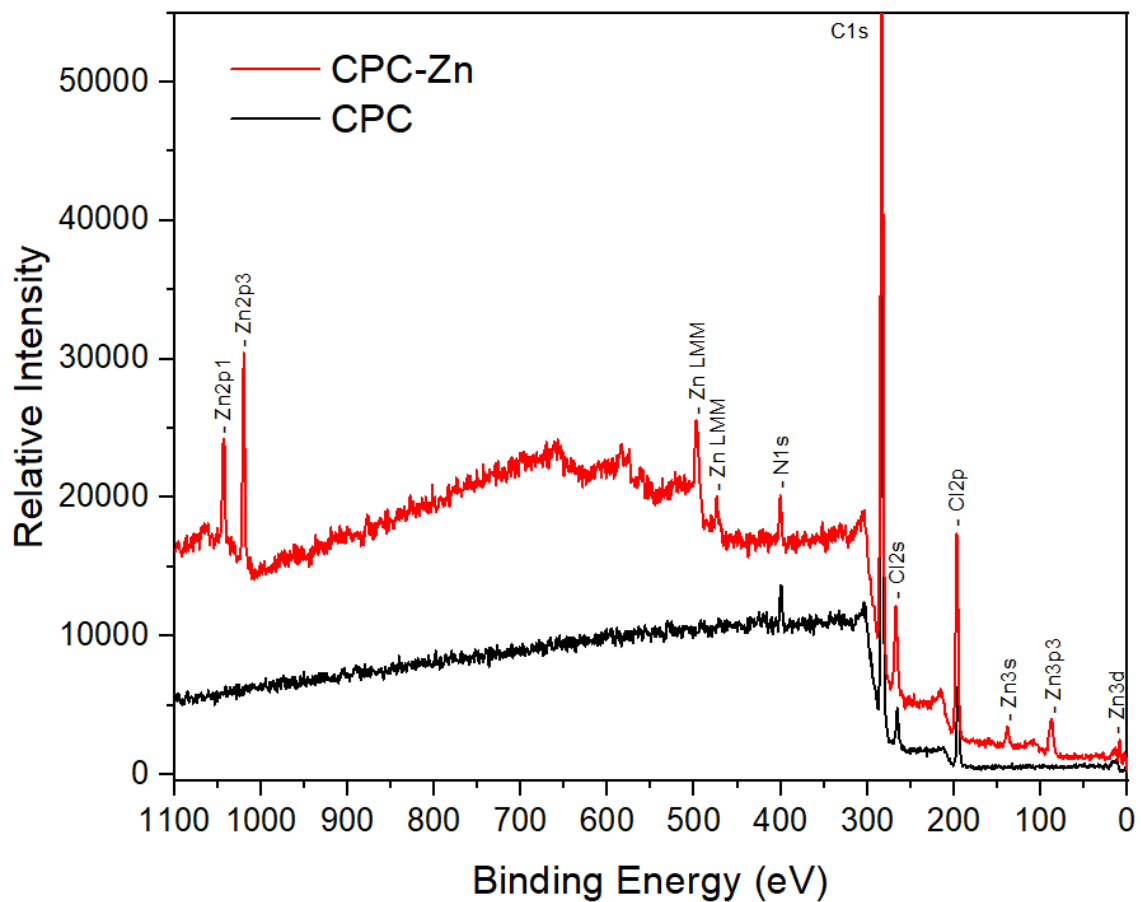


Figure 3.2. XPS survey spectra of CPC and CPC-Zn material.

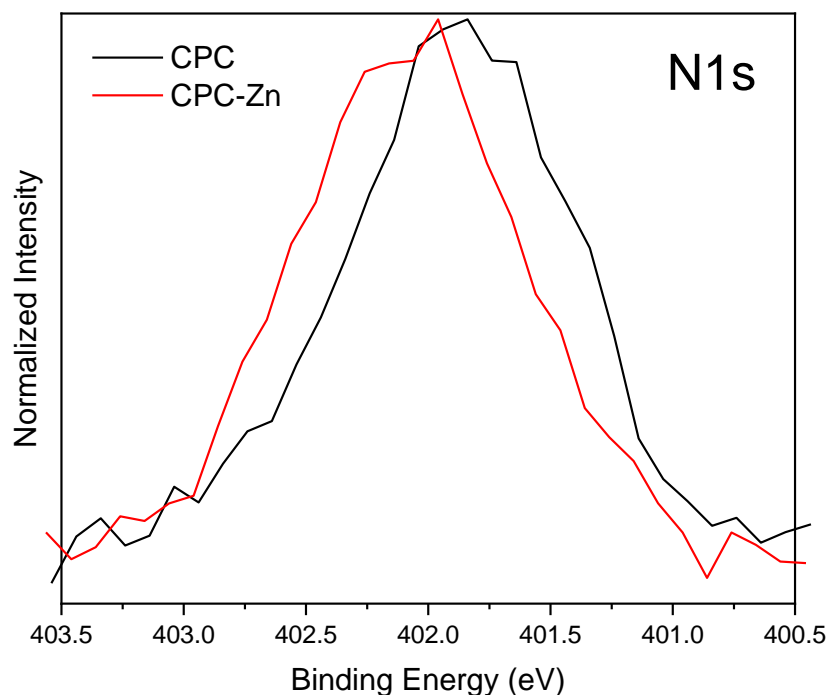


Figure 3.3. Enlarged and normalized XPS spectra of the CPC and CPC-Zn material N1s peaks.

The FTIR spectra of CPC·H₂O, ZnCl₂, and as-synthesized CPC-Zn material are shown in Figure 3.4. The spectrum of CPC-Zn sample clearly shows the fingerprint of the cetylpyridinium confirming its presence in the sample. A close inspection of the spectrum demonstrates, however, that the bands of cetylpyridinium in the CPC-Zn material do not match the pure CPC·H₂O compound. The majority of the bands related to C-H, CH₂, C-C, C=C, and C=N stretching and bending vibrations of cetylpyridinium display shifted peak positions compared to CPC·H₂O raw material.^{39,40} The ν(OH) peak at 3372 cm⁻¹ as well as another broad H₂O related band near 550 cm⁻¹ seen in CPC·H₂O starting compound have also disappeared in the presence of Zn. Furthermore, a distinguishable

new peak at 272 cm^{-1} is evident in the CPC-Zn sample, likely originating from the Zn-Cl related vibration. Taken together, the FTIR data indicate that the interaction of cetylpyridinium chloride with ZnCl_2 formed a different complex.

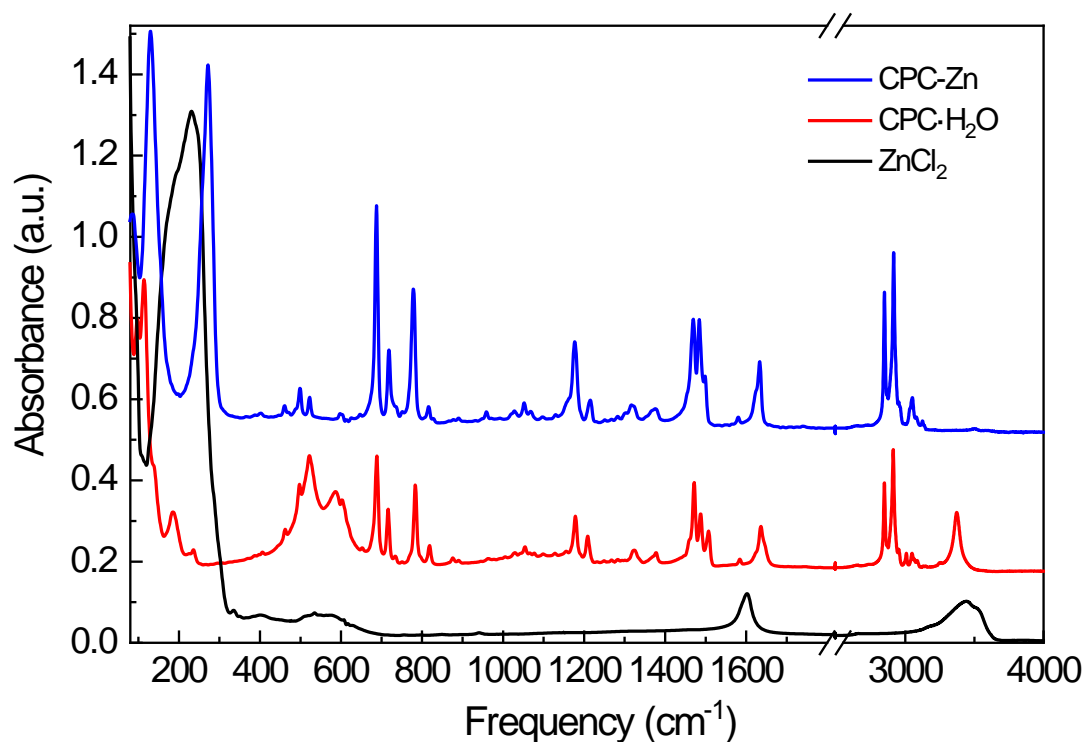


Figure 3.4. Infrared absorption spectra of synthesized CPC-Zn material as well as $\text{CPC}\cdot\text{H}_2\text{O}$ and ZnCl_2 precursors. The spectra are offset for clarity. Note, ZnCl_2 is highly hygroscopic, so the presence of water and its associated absorption bands are difficult to avoid during sample measurements.

The single crystal X-ray diffraction (SCXRD) analysis shows that the coordination complex crystallizes in orthorhombic *Pbca* space group (Tables 3.1-3.2). The structural formula can be described as $[(\text{C}_{21}\text{H}_{38}\text{N})_2][\text{ZnCl}_4]$, or $(\text{CP})_2\text{ZnCl}_4$ for short, where four cetylpyridinium ions are surrounded by two ZnCl_4^{2-} units (Figure 3.5). The

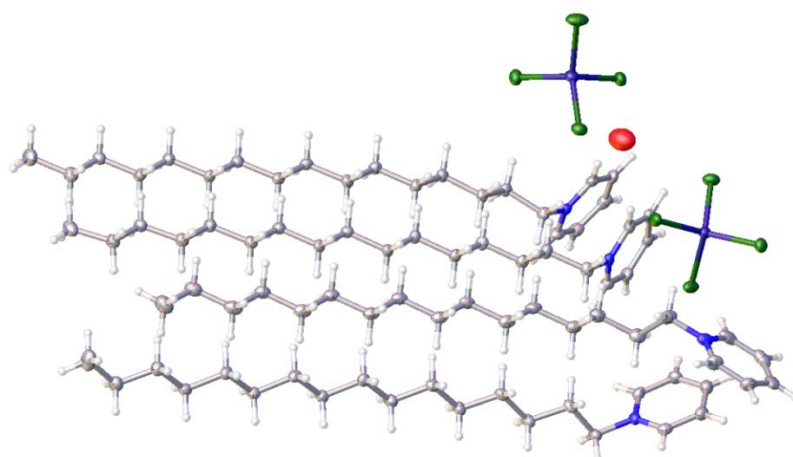
packing behavior is depicted in Figure 3.6. As seen from the structure, the alkyl chain units and the Zn units pack in a zig-zag manner, with each unit present at alternating ends.

Table 3.1. Crystal data and structure refinement for (CP)₂ZnCl₄ at 100 K.

Empirical formula	C ₄₂ H ₇₆ Cl ₄ N ₂ O _{0.13} Zn
Formula weight	818.34
Temperature/K	100(2)
Crystal system	orthorhombic
Space group	Pbca
a/Å	14.0801(3)
b/Å	20.5166(4)
c/Å	62.5674(12)
α/°	90
β/°	90
γ/°	90
Volume/Å ³	18074.2(6)
Z	16
ρ _{calc} /g/cm ³	1.203
μ/mm ⁻¹	3.139
F(000)	7057.0
Crystal size/mm ³	0.129 × 0.106 × 0.042
Radiation	CuKα (λ = 1.54178)
2θ range for data collection/°	5.65 to 138.264
Index ranges	-16 ≤ h ≤ 16, -23 ≤ k ≤ 24, -74 ≤ l ≤ 73
Reflections collected	89945
Independent reflections	16573 [R _{int} = 0.0803, R _{sigma} = 0.0515]
Data/restraints/parameters	16573/0/897
Goodness-of-fit on F ²	1.043
Final R indexes [I ≥ 2σ (I)]	R ₁ = 0.0481, wR ₂ = 0.0900
Final R indexes [all data]	R ₁ = 0.0772, wR ₂ = 0.0997
Largest diff. peak/hole / e Å ⁻³	0.32/-0.42

Table 3.2. Crystal data and structure refinement for (CP)₂ZnCl₄ at 298 K.

Empirical formula	C ₄₂ H ₇₆ Cl ₄ N ₂ Zn
Formula weight	816.21
Temperature/K	297.58
Crystal system	orthorhombic
Space group	Pbca
a/Å	14.6776(5)
b/Å	20.6265(7)
c/Å	62.330(2)
α/°	90
β/°	90
γ/°	90
Volume/Å ³	18870.4(11)
Z	16
ρ _{calc} /cm ³	1.149
μ/mm ⁻¹	3.003
F(000)	7040.0
Crystal size/mm ³	0.129 × 0.106 × 0.042
Radiation	CuKα (λ = 1.54178)
2θ range for data collection/°	5.672 to 96.904
Index ranges	-14 ≤ h ≤ 14, -16 ≤ k ≤ 20, -56 ≤ l ≤ 60
Reflections collected	50657
Independent reflections	9038 [R _{int} = 0.0907, R _{sigma} = 0.0582]
Data/restraints/parameters	9038/0/887
Goodness-of-fit on F ²	1.028
Final R indexes [I ≥ 2σ (I)]	R ₁ = 0.0553, wR ₂ = 0.0969
Final R indexes [all data]	R ₁ = 0.1140, wR ₂ = 0.1180
Largest diff. peak/hole / e Å ⁻³	0.26/-0.29

**Figure 3.5.** Crystal structure of [(C₂₁H₃₈N)₂][ZnCl₄].

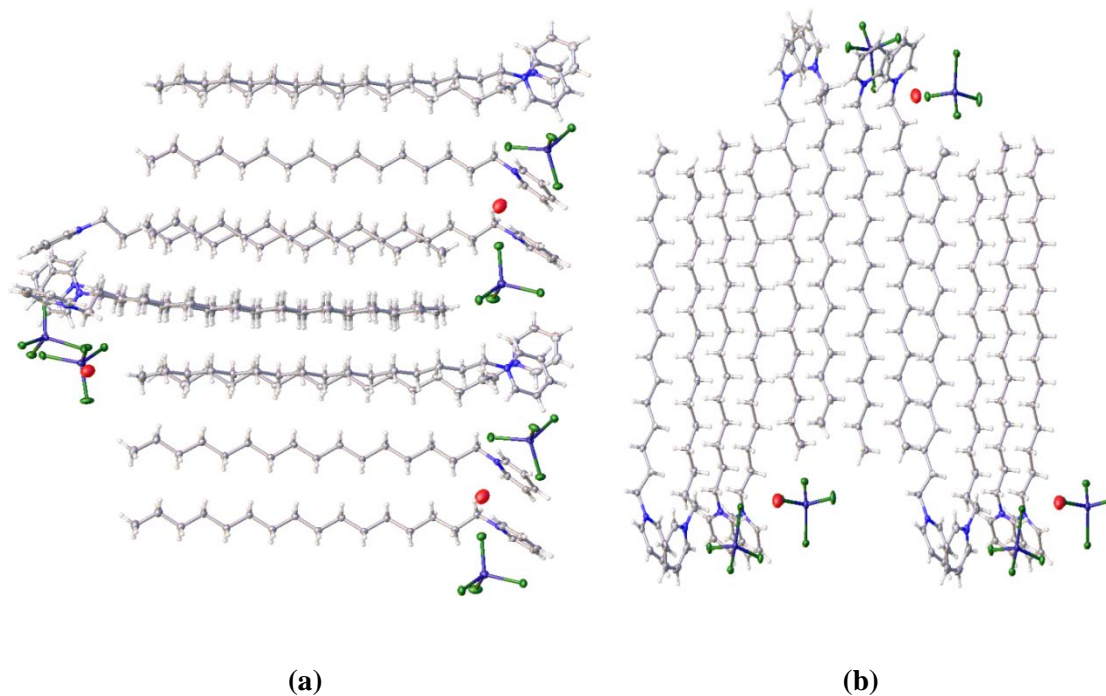


Figure 3.6. Packing of $[(C_{21}H_{38}N)_2][ZnCl_4]$ along (a) 110 plane and (b) 100 plane at 100K.

The crystals contain disordered solvent that was modeled as a H_2O molecule (atom O1). It was not possible to locate hydrogen atoms of H_2O . The occupancy of the H_2O molecule is ~ 0.25 and it is not present in the crystals collected at room temperature. There is a structural change with the increase in temperature and the loss of solvent H_2O molecule. The distance between the Zn(II) centers (Zn01-Zn02) increases from 8.73 Å (at 100 K) to 9.05 Å (at 298 K). The packing behavior at room temperature however remains similar in a zig-zag manner (Figure 3.7). PXRD analysis of the bulk sample recrystallized in acetone showed that it is in good agreement with the calculated structure both at 100 and 298 K (Figure 3.8), confirming phase purity.

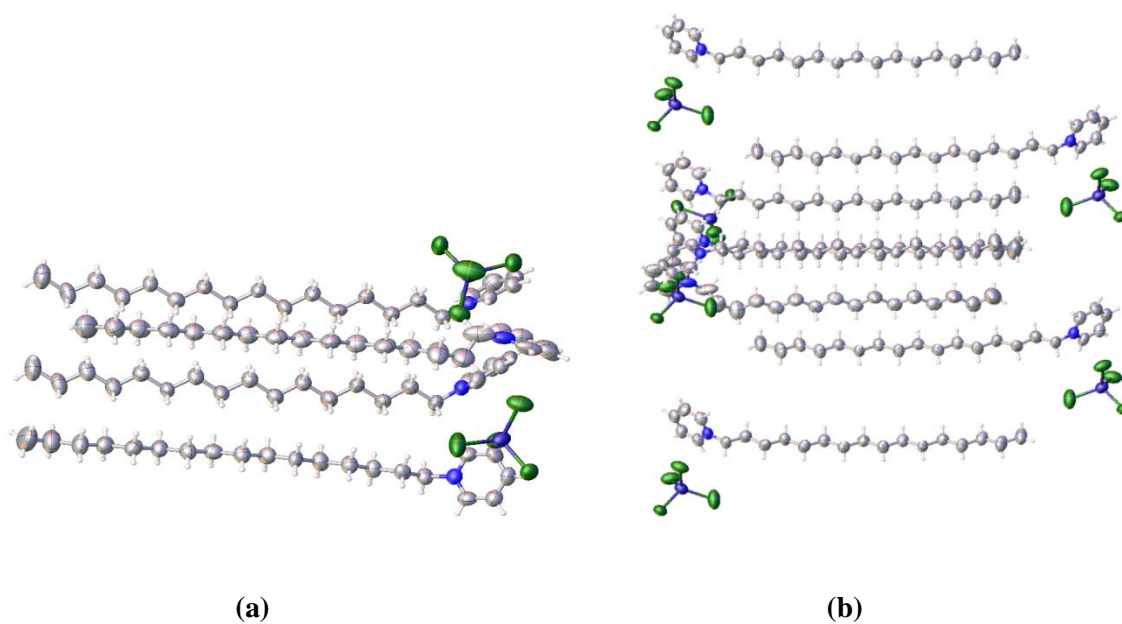


Figure 3.7. (a) Structure of $[(C_{21}H_{38}N)_2][ZnCl_4]$ at 298 K and (b) packing arrangement.

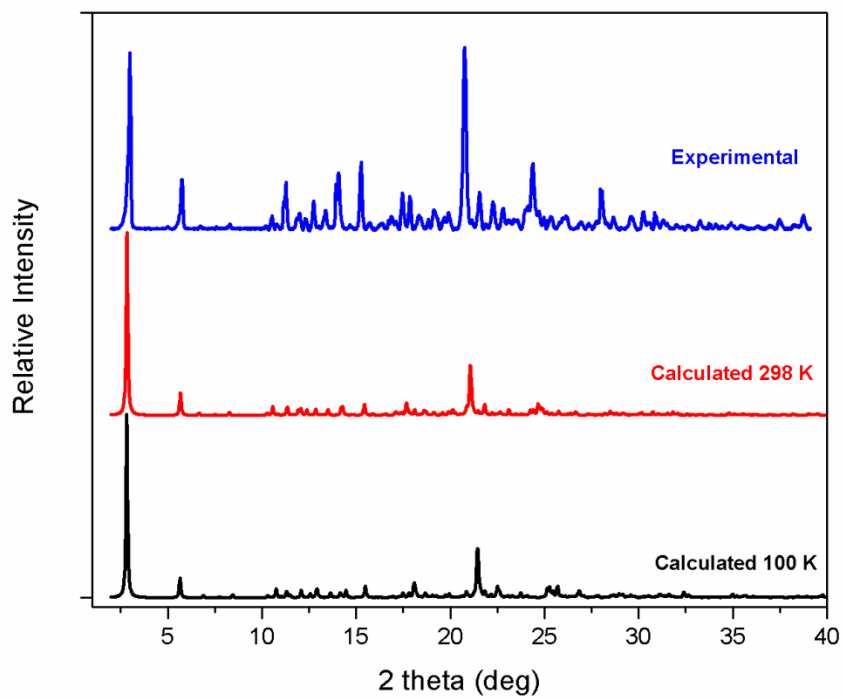


Figure 3.8. A comparison of the PXRD patterns of the bulk sample, the calculated pattern at 298 K and the calculated pattern at 100 K.

In-vitro VSC reduction of ZnCl_2 , $(\text{CP})_2\text{ZnCl}_4$, and CPC, conducted by methyl mercaptan GC headspace measurement, is illustrated in Figure 3.9d. Statistical grouping (Table 3.3), calculated using Tukey method and 95.0% confidence interval, indicates that CPC and $(\text{CP})_2\text{ZnCl}_4$ exhibit parity efficacy for malodor-causing VSC.⁴¹ ZnCl_2 exhibits a weak VSC reduction effect at the measured concentration compared to CPC and $(\text{CP})_2\text{ZnCl}_4$.

Elemental composition of the evaluated powders is shown in Table 3.4. The concentration of ZnCl_2 (*i.e.*, 16.22%) in the $(\text{CP})_2\text{ZnCl}_4$ is in decent agreement with the theoretical value (*i.e.*, 16.70%) which implies adequate purity of the sample as a result of the acetone extraction process.

Table 3.3. Statistical grouping information using Tukey method and 95.0% confidence.

Treatment	N	Mean*	Grouping
Zinc Chloride Anhydrous	3	10.9458	A
CPC- ZnCl_2	3	7.5214	C
Cetylpyridinium chloride	3	7.5193	C

*Average $\log(\text{Integrated Methyl Mercaptan Area})$ of triplicate samples

Table 3.4. Elemental composition of powders used to prepare VSC reduction samples.

Sample	Zn (%)	CPC (%)
H_2O	-	-
ZnCl_2	44.81	-
$(\text{CP})_2\text{ZnCl}_4$	7.78	86.02
CPC	-	97.95

*Zn and CPC concentrations were obtained via AAS and HPLC, respectively.

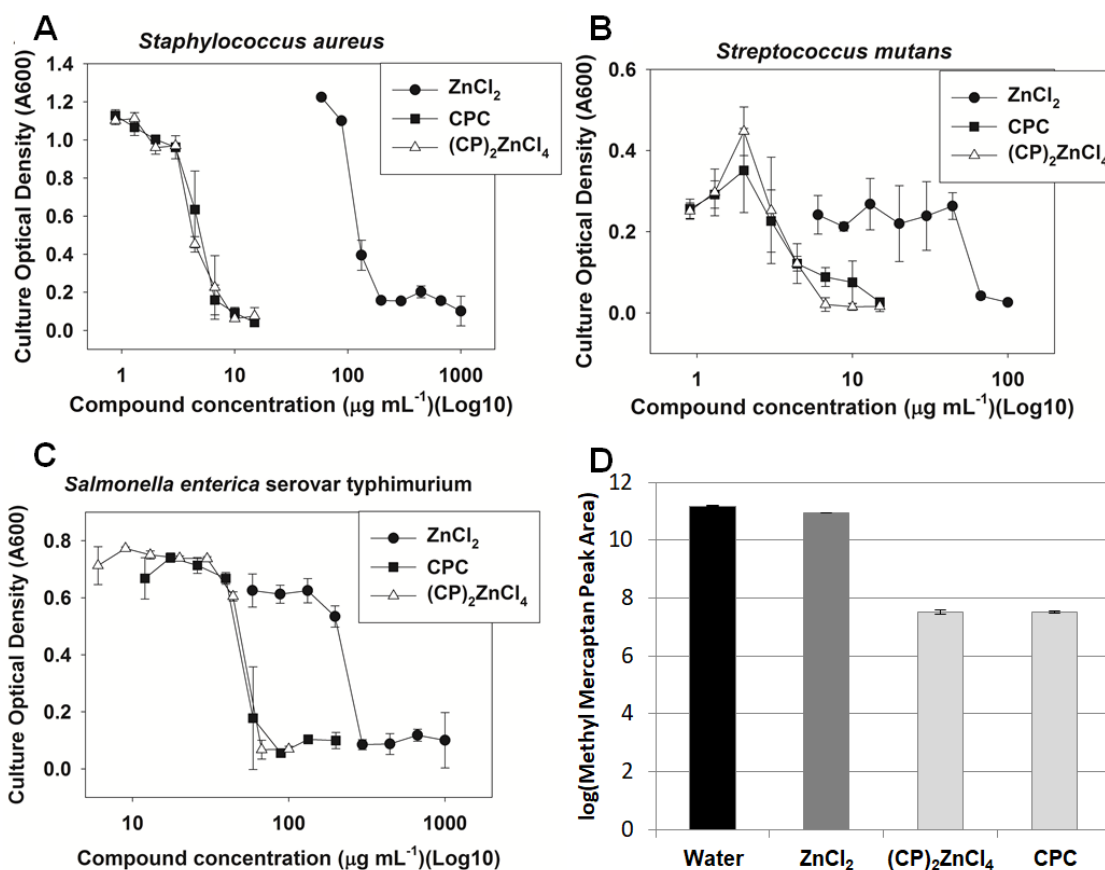


Figure 3.9. Inhibition of *S. aureus* (a), *S. mutans* (b), and *S. enterica* (c) with ZnCl_2 , CPC and $(\text{CP})_2\text{ZnCl}_4$. Culture optical densities were determined after static growth. VSC reduction efficacy (d) of methyl mercaptan *via* GC with color shading corresponding to statistical group (Table 3.3).

We examined the ability of CPC, Zn, and $(\text{CP})_2\text{ZnCl}_4$ to inhibit the growth of bacterial pathogens. The effects of the compounds were determined using the following bacterial pathogens: *Staphylococcus aureus* LAC, *Streptococcus mutans*, and *Salmonella enterica* Serovar typhimurium. *S. aureus* LAC is a gram-positive community-associated methicillin-resistant CA-MRSA strain and a representative strain of the USA300 clone,

which is a leading cause of skin and soft tissue infections in North America.⁴² *S. mutans* is also gram-positive and the leading causes of dental caries.⁴³ *Salmonella enterica* Serovar typhimurium is a gram-negative and a primary enteric pathogen affecting humans.⁴⁴

The minimal inhibitory concentrations of CPC, Zn, and $(\text{CP})_2\text{ZnCl}_4$ were determined in liquid culture after static growth. All the three bacteria displayed typical dose-responses to the compounds utilized (Figure 3.9a-c). The MICs for Zn for *S. aureus*, *S. enterica*, and *S. mutans* were approximately 200, 300, and 65 $\mu\text{g mL}^{-1}$, respectively. The MICs for $(\text{CP})_2\text{ZnCl}_4$ for *S. aureus*, *S. enterica*, and *S. mutans* were 6, 60, and 6 $\mu\text{g mL}^{-1}$, respectively. The MICs for CPC were similar to those for $(\text{CP})_2\text{ZnCl}_4$ in the case of *S. aureus* and *S. enterica*. In the case of *S. mutans*, a slight improvement in antimicrobial activity was demonstrated for $(\text{CP})_2\text{ZnCl}_4$, however, the results were not statistically significant.

Previous work demonstrated that the utilization of MSNs as drug delivery vehicles for QACs yields a material with a pH-responsive controlled drug release as well as excellent antimicrobial activity.²⁰ Herein, the feasibility of incorporating $(\text{CP})_2\text{ZnCl}_4$ into such drug delivery systems (DDSs), where the surface of MSNs can further be modified to impart selectivity or other advantages, were explored.⁴⁵ BET measurements (Figures 3.10-3.11 and Table 3.5) indicated successful loading of the material within SBA-15 as evidenced by a reduction in available surface area and pore width. Additionally, SAXRD patterns (Figure 3.12) suggest the mesoporous silica framework remains intact throughout the loading process. The material where $(\text{CP})_2\text{ZnCl}_4$ was loaded into SBA-15 MSNs is referred to as CPC-Zn@SBA-15 henceforth due to a certain

amount of uncertainty whether all CPC-Zn moieties within the MSNs are in fact $(\text{CP})_2\text{ZnCl}_4$. Actually, elemental composition suggests an excess of Zn, which is likely chemisorbed to the silanol groups. Bulk elemental composition measurements of CPC-Zn@SBA-15 was conducted using TGA and ICP-OES for CPC (9.0 wt.%) and Zn (8.9 wt.%), respectively. XPS analysis was conducted on mesoporous SBA-15, CPC@SBA-15, and CPC-Zn@SBA-15 to probe the elemental composition near the surface of the MSNs. Calcined SBA-15 is consistent with composition of silica with a surface that is essentially free (1.1 wt.% C) from organic contamination. The N^+/Cl ratio (1.29) of the CPC@SBA-15 sample suggests that a portion of the cetylpyridinium cations have adsorbed onto the negative silanol groups of the silica. The N^+ binding energy is shifted slightly relative to the CPC reference, while the Cl binding energy is significantly shifted relative to CPC. This implies that both N^+ and Cl are in different chemical bonding environments on the silica surface, compared to bulk CPC. The surface of CPC-Zn@SBA-15 material exhibited 3.36 wt.% Zn, 1.01 wt.% CPC, and a Zn/CPC ratio of 3.33. The Zn/CPC ratio indicates that $(\text{CP})_2\text{ZnCl}_4$ is present on the surface with excess ZnCl_2 . Since the sample was washed with water after preparation, it is possible that the $(\text{CP})_2\text{ZnCl}_4$ recrystallized on the surface or dissolved into its ionic constituents and precipitated onto the surface of MSNs.

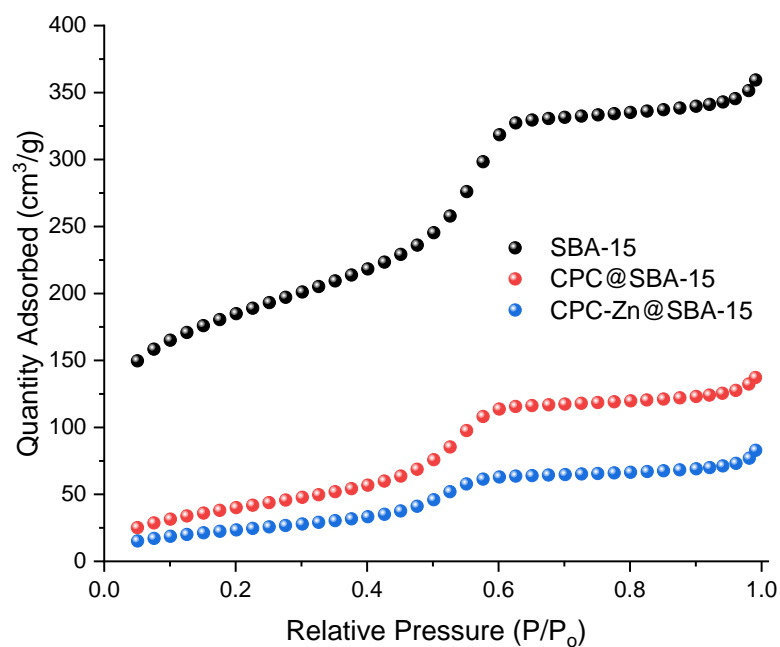


Figure 3.10. N₂ adsorption isotherms (77 K) for SBA-15, CPC@SBA-15 and CPC-Zn@SBA-15.

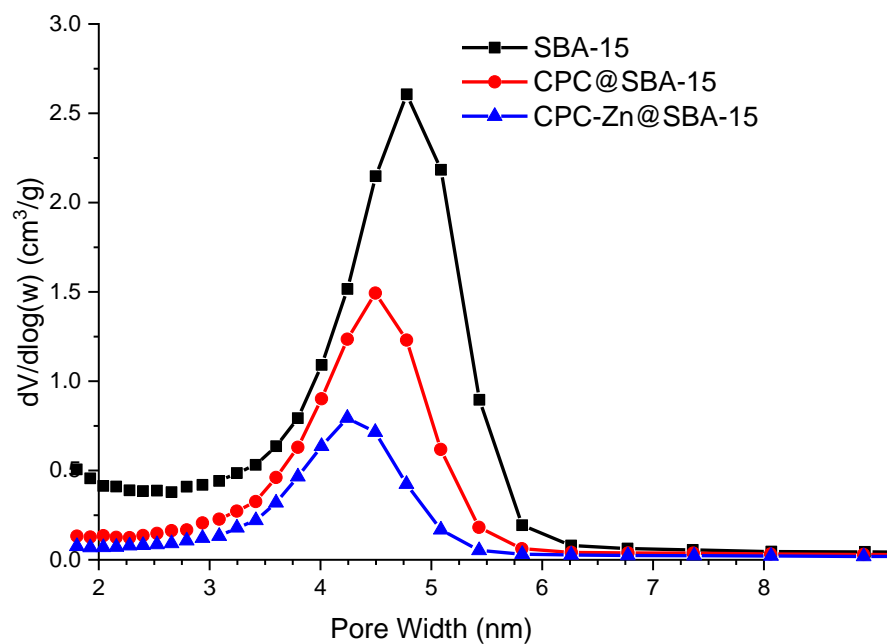
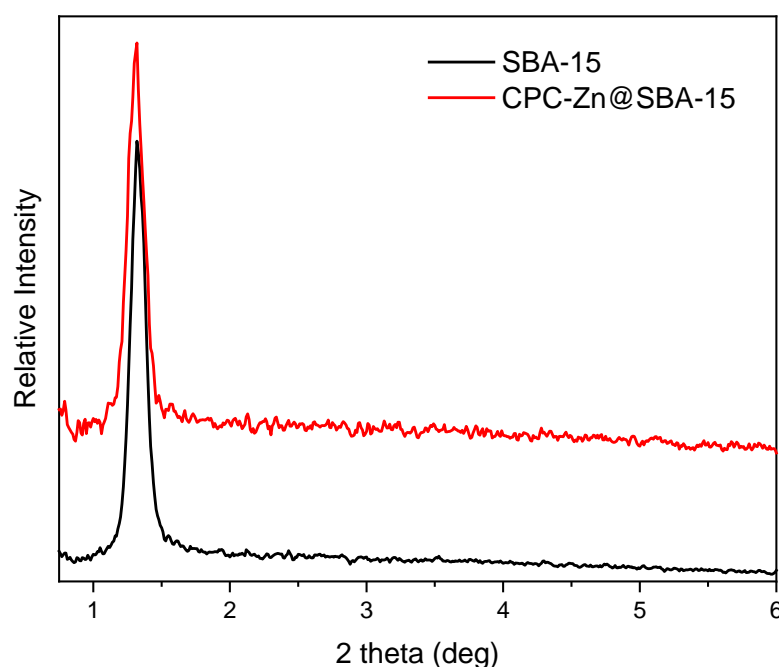


Figure 3.11. BJH pore size distribution corresponding to the isotherms in Figure 3.10.

Table 3.5. Porosimetry results and SAXRD data.

Sample	BET Surface Area ($m^2 g^{-1}$)	Pore Width (\AA)	Pore Wall Thickness (\AA)	2 θ	Crystal Size* (nm)
SBA-15	626.7	48	18	1.328	77
CPC@SBA-15	153.0	45			
CPC-Zn@SBA-15	89.6	43		1.311	66

* Crystallite size obtained using Scherrer equation^{46,47}

**Figure 3.12.** SAXRD pattern of SBA-15 and $(CP)_2ZnCl_4@SBA-15$.

As previously discussed, ICP-OES, TGA, and XPS analyses demonstrate significant amounts of cetylpyridinium and Zn in the CPC-Zn@SBA-15 sample. FTIR was further used to investigate the presence of $(CP)_2ZnCl_4$ within the silica framework. Figure 3.13 shows the spectrum of CPC-Zn@SBA-15 sample in comparison to CPC@SBA-15 control and SBA-15 mesoporous silica. SBA-15 displays a typical silica spectrum with Si-O asymmetric and symmetric vibrations near 1060 and 800 cm^{-1}

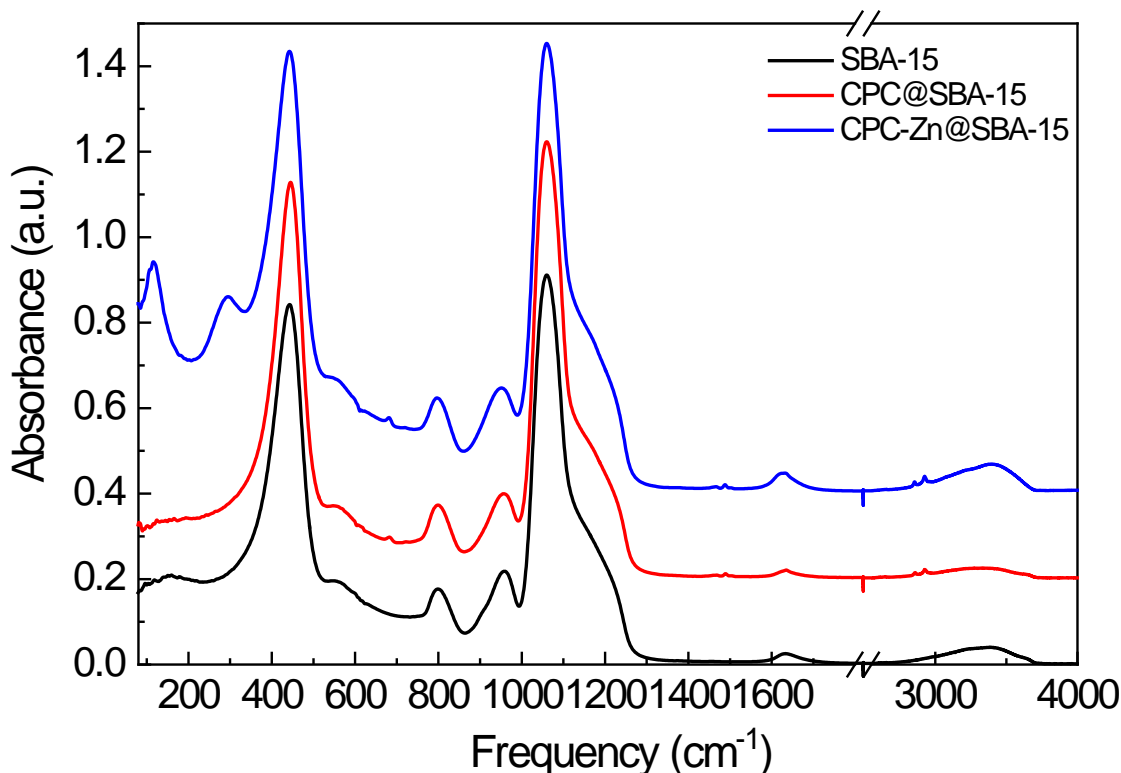


Figure 3.13. Infrared absorption spectrum of CPC-Zn@SBA-15 in comparison to CPC@SBA-15 and SBA-15. Spectra are offset for clarity.

respectively, non-bridging Si-O stretching vibration and/or Si-OH vibration of silanol groups near 955 cm^{-1} and O-Si-O bending modes around 440 cm^{-1} . The absorption spectra of CPC-Zn@SBA-15 and CPC@SBA-15 support the presence of cetylpyridinium in both samples as evident from its characteristic vibrations near 1500 cm^{-1} region as well as near the C-H stretching band region where two peaks around 2855 and 2925 cm^{-1} corresponding to symmetric and asymmetric CH_2 vibrations are clearly observed.⁴⁸ Importantly, in addition to cetylpyridinium bands, the CPC-Zn@SBA-15 sample exhibits two distinct peaks near 115 and 295 cm^{-1} , in line with the pure $(\text{CP})_2\text{ZnCl}_4$ fingerprint that displays two strong bands below 300 cm^{-1} (Figure 3.4). This finding suggest

presence of $(\text{CP})_2\text{ZnCl}_4$ complex on the silica surface. Note, the peak positions of cetylpyridinium and $(\text{CP})_2\text{ZnCl}_4$ incorporated into silica are shifted compared to their bulk constituents. The latter can be attributed to adsorption and/or confinement effects.

3.5. Conclusion

An interesting CPC analogue, cetylpyridinium tetrachlorozincate, was synthesized and unambiguously characterized *via* single crystal X-ray diffraction measurements indicating a stoichiometry of $\text{C}_{42}\text{H}_{76}\text{Cl}_4\text{N}_2\text{Zn}$ with two cetylpyridinium cations per $[\text{ZnCl}_4]^{2-}$ tetrahedra. The material was evaluated and shows promising characteristics for application as a broad-spectrum antimicrobial agent, to reduce volatile sulfur compounds (VSCs) generated by bacteria, and in the synthesis of advanced functional materials. VSC experiments and antimicrobial assays demonstrate that $(\text{CP})_2\text{ZnCl}_4$ exhibits at least parity efficacy to pure CPC while comprising *ca.* 16% of the significantly less efficacious and expensive zinc chloride material. An advanced functional material was prepared by successfully loading $(\text{CP})_2\text{ZnCl}_4$ into SBA-15, which is a promising candidate for a highly efficient drug delivery system (DDS) for stimulated-release antimicrobial applications.^{20,49} This new technology paves the way for development of next generation and highly efficacious healthcare treatments with potentially reduced risk of exacerbating the problem of antibiotic resistance.

3.6. References

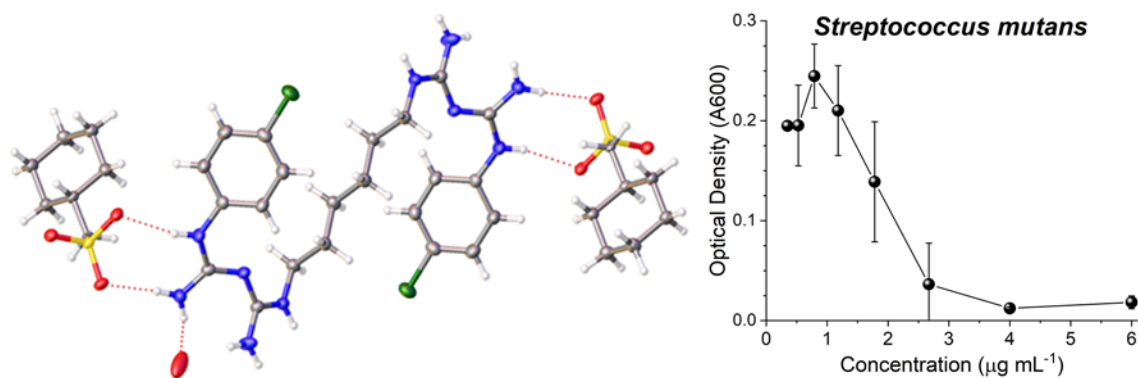
- (1) Ash, M.; Ash, I., *Handbook of Preservatives*. Synapse information resources: 2004.
- (2) Imai, H.; Kita, F.; Ikesugi, S.; Abe, M.; Sogabe, S.; Nishimura-Danjobara, Y.; Miura, H.; Oyama, Y., Cetylpyridinium chloride at sublethal levels increases the susceptibility of rat thymic lymphocytes to oxidative stress. *Chemosphere* **2017**, *170*, 118-123.
- (3) Food and Drug Administration, Oral health care drug products for over-the-counter human use; antigingivitis/antiplaque drug products; establishment of a monograph; proposed rules. Federal Register: 2003; Vol. 68, p 32247.
- (4) Sreenivasan, P. K.; Haraszthy, V. I.; Zambon, J. J., Antimicrobial efficacy of 0.05% cetylpyridinium chloride mouthrinses. *Lett. Appl. Microbiol.* **2013**, *56* (1), 14-20.
- (5) Liu, J.; Ling, J. Q.; Wu, C. D., Cetylpyridinium chloride suppresses gene expression associated with halitosis. *Arch. Oral Biol.* **2013**, *58*, 1686-1691.
- (6) Gibb, R.; Dunavent, J.; Flood, J.; Barnes, J.; Witt, J.; Ramji, N., Antibacterial and antiplaque effects of a novel, alcohol-free oral rinse with cetylpyridinium chloride. *J. Contemp. Dent. Pract.* **2005**, *6* (1), 001-009.
- (7) Rahardjo, A.; Ramadhani, A.; Adiatman, M.; Wimardhani, Y. S.; Maharani, D. A., Efficacy of mouth rinse formulation based on cetyl pyridinium chloride in the control of plaque as an early onset of dental calculus built up. *J. Int. Dent. Med. Res.* **2016**, *9* (3), 184-188.
- (8) Crans, D. C.; Meade, T. J., Preface for the forum on metals in medicine and health: new opportunities and approaches to improving health. *Inorg. Chem.* **2013**, *52*, 12181-12183
- (9) Martin, D. P.; Hann, Z. S.; Cohen, S. M., Metallo-protein-inhibitor binding: human carbonic anhydrase II as a model for probing metal-ligand interactions in a metalloprotein active site. *Inorg. Chem.* **2013**, *52*, 12207-12215.
- (10) Wu, X.-F.; Neumann, H., Zinc-catalyzed organic synthesis: C-C, C-N, C-O bond formation reactions. *Adv. Synth. Catal.* **2012**, *354* (17), 3141-3160.
- (11) Mainar, A. R.; Iruin, E.; Colmenares, L. C.; Kvasa, A.; de Meatza, I.; Bengoechea, M.; Leonet, O.; Boyano, I.; Zhang, Z.; Blazquez, J. A., An overview of progress in electrolytes for secondary zinc-air batteries and other storage systems based on zinc. *J. Energy Storage* **2018**, *15*, 304-328.
- (12) Ma, L.; Terwilliger, A.; Maresso, A. W., Iron and zinc exploitation during bacterial pathogenesis. *Metallomics* **2015**, *7* (12), 1541-1554.
- (13) Chandrangu, P.; Rensing, C.; Helmann, J. D., Metal homeostasis and resistance in bacteria. *Nature reviews. Microbiology* **2017**, *15* (6), 338-350.
- (14) Stanić, V.; Dimitrijević, S.; Antić-Stanković, J.; Mitrić, M.; Jokić, B.; Plečaš, I. B.; Raičević, S., Synthesis, characterization and antimicrobial activity of copper and zinc-doped hydroxyapatite nanopowders. *Appl. Surf. Sci.* **2010**, *256* (20), 6083-6089.
- (15) Zhang, J.; Qin, X.; Wang, B.; Xu, G.; Qin, Z.; Wang, J.; Wu, L.; Ju, X.; Bose, D. D.; Qiu, F.; Zhou, H.; Zou, Z., Zinc oxide nanoparticles harness autophagy to induce cell death in lung epithelial cells. *Cell Death Dis.* **2017**, *8* (7), e2954.

- (16) Pasquet, J.; Chevalier, Y.; Pelletier, J.; Couval, E.; Bouvier, D.; Bolzinger, M.-A., The contribution of zinc ions to the antimicrobial activity of zinc oxide. *Colloids Surf. A Physicochem. Eng. Asp.* **2014**, *457*, 263-274.
- (17) Li, J.; Ren, X.; Fan, B.; Huang, Z.; Wang, W.; Zhou, H.; Lou, Z.; Ding, H.; Lyu, J.; Tan, G., Zinc toxicity and iron-sulfur cluster biogenesis in *Escherichia coli*. *Appl. Environ. Microbiol.* **2019**, *85* (9), e01967-18.
- (18) Xu, F. F.; Imlay, J. A., Silver(I), mercury(II), cadmium(II), and zinc(II) target exposed enzymic iron-sulfur clusters when they toxify *Escherichia coli*. *Appl. Environ. Microbiol.* **2012**, *78* (10), 3614-3621.
- (19) Arrigler, V.; Kogej, K.; Majhenc, J.; Svetina, S., Interaction of cetylpyridinium chloride with giant lipid vesicles. *Langmuir* **2005**, *21*, 7653-7661.
- (20) Dubovoy, V.; Ganti, A.; Zhang, T.; Al-Tameemi, H.; Cerezo, J. D.; Boyd, J. M.; Asefa, T., One-pot hydrothermal synthesis of benzalkonium-templated mesostructured silica antibacterial agents. *J. Am. Chem. Soc.* **2018**, *140* (42), 13534-13537.
- (21) Neve, F.; Francescangeli, O.; Crispini, A., Crystal architecture and mesophase structure of long-chain N-alkylpyridinium tetrachlorometallates. *Inorganica Chim. Acta* **2002**, *338*, 51-58.
- (22) Hilp, M.; Zembatova, S., Cetylpyridinium tetrachlorozincate as standard for tenside titration. Analytical methods with 1,3-dibromo-5,5-dimethylhydantoin (DBH) in respect to environmental and economical concern, part 19. *Die Pharmazie* **2004**, *59* (8), 615-7.
- (23) Hilp, M., Determination of anionactive tensides using cetylpyridinium tetrachlorozincate as titrant. Analytical methods in respect to environmental and economical concern, part 20. *Die Pharmazie* **2004**, *59* (9), 676-7.
- (24) Kaur, G.; Kumar, S.; Dilbaghi, N.; Bhanjana, G.; Guru, S. K.; Bhushan, S.; Jaglan, S.; Hassan, P. A.; Aswal, V. K., Hybrid surfactants decorated with copper ions: aggregation behavior, antimicrobial activity and anti-proliferative effect. *Phys. Chem. Chem. Phys.* **2016**, *18* (34), 23961-23970.
- (25) Bruker APEX3 (Version 2015.9), Bruker AXS Inc.: Madison, Wisconsin, USA, 2016.
- (26) Bruker SAINT-V8.35A. *Data Reduction Software*, Madison, Wisconsin, USA, 2016.
- (27) Sheldrick, G. M. *SADABS. Program for Empirical Absorption Correction*, University of Gottingen: Germany, 1996.
- (28) Sheldrick, G., Crystal structure refinement with SHELXL. *Acta Cryst. C* **2015**, *71* (1), 3-8.
- (29) Sheldrick, G., Phase annealing in SHELX-90: direct methods for larger structures. *Acta Cryst. A* **1990**, *46* (6), 467-473.
- (30) Sheldrick, G., A short history of SHELX. *Acta Cryst. A* **2008**, *64* (1), 112-122.
- (31) Dolomanov, O. V.; Bourhis, L. J.; Gildea, R. J.; Howard, J. A. K.; Puschmann, H., OLEX2: a complete structure solution, refinement and analysis program. *J. Appl. Crystallogr.* **2009**, *42* (2), 339-341.
- (32) Yaegaki, K.; Sanada, K., Volatile sulfur compounds in mouth air from clinically healthy subjects and patients with periodontal disease. *J. Periodontal Res.* **1992**, *27* (4), 233-238.

- (33) Boyd, J. M.; Teoh, W. P.; Downs, D. M., Decreased transport restores growth of a *Salmonella enterica* apbC mutant on tricarballoylate. *J. Bacteriol.* **2012**, *194* (3), 576-583.
- (34) Roberts, C. A.; Al-Tameemi, H. M.; Mashruwala, A. A.; Rosario-Cruz, Z.; Chauhan, U.; Sause, W. E.; Torres, V. J.; Belden, W. J.; Boyd, J. M., The suf iron-sulfur cluster biosynthetic system is essential in *Staphylococcus aureus*, and decreased suf function results in global metabolic defects and reduced survival in human neutrophils. *Infect. Immun.* **2017**, *85* (6).
- (35) *Methods for Dilution Antimicrobial Susceptibility Tests for Bacteria That Grow Aerobically; Approved Standard - Ninth Edition.* Clinical and Laboratory Standards Institute: Wayne, PA, 2012.
- (36) Richardson, J. J.; Björnmalm, M.; Caruso, F., Technology-driven layer-by-layer assembly of nanofilms. *Science* **2015**, *348* (6233), aaa2491.
- (37) Brunauer, S.; Emmett, P. H.; Teller, E., Adsorption of gases in multimolecular layers. *J. Am. Chem. Soc.* **1938**, *60* (2), 309-319.
- (38) Barrett, E. P.; Joyner, L. G.; Halenda, P. P., The determination of pore volume and area distributions in porous substances. I. Computations from nitrogen isotherms. *J. Am. Chem. Soc.* **1951**, *73* (1), 373-380.
- (39) Gelmboldt, V. O.; Anisimov, V. Y.; Bevz, N. Y.; Georgiyants, V. A., Development of methods for identification of cetylpyridinium hexafluorosilicate. *Der Pharma Chemica* **2016**, *8* (1), 169-173.
- (40) Cook, D., Vibrational spectra of pyridinium salts. *Can. J. Chem.* **1961**, *39*, 2009-2024.
- (41) Tukey, J. W., Comparing individual means in the analysis of variance. *Biometrics* **1949**, *5* (2), 99-114.
- (42) Planet, P. J., Life after USA300: The rise and fall of a superbug. *J. Infect. Dis.* **2017**, *215*, S71-S77.
- (43) Loesche, W. J., Role of *Streptococcus mutans* in human dental decay. *Microbiol. Rev.* **1986**, *50* (4), 353.
- (44) Fàbrega, A.; Vila, J., *Salmonella enterica* serovar Typhimurium skills to succeed in the host: virulence and regulation. *Clin. Microbiol. Rev.* **2013**, *26* (2), 308.
- (45) Li, Z.; Barnes, J. C.; Bosoy, A.; Stoddart, J. F.; Zink, J. I., Mesoporous silica nanoparticles in biomedical applications. *Chem. Soc. Rev.* **2012**, *41* (7), 2590-2605.
- (46) Scherrer, P., *Nachr. Ges. Wiss. Gottingen* **1918**, *26*, 98-100.
- (47) Langford, J. I.; Wilson, A. J. C., Scherrer after sixty years: A survey and some new results in the determination of crystallite size. *J. Appl. Crystallogr.* **1978**, *11* (2), 102-113.
- (48) Kung, K. H. S.; Hayes, K. F., Fourier transform infrared spectroscopic study of the adsorption of cetyltrimethylammonium bromide and cetylpyridinium chloride on silica. *Langmuir* **1993**, *9* (1), 263-267.
- (49) Yang, P.; Huang, S.; Kong, D.; Lin, J.; Fu, H., Luminescence functionalization of SBA-15 by YVO₄:Eu³⁺ as a novel drug delivery system. *Inorg. Chem.* **2007**, *46*, 3203-3211

CHAPTER 4

Synthesis, Characterization, and Antimicrobial Investigation of a Novel Chlorhexidine Cyclamate Complex



4.1. Overview

The synthesis, crystal structure, and antimicrobial efficacy are reported for a novel complex comprising a 1:2 ratio of chlorhexidine (CHX) to N-cyclohexylsulfamate (*i.e.*, artificial sweetener known as cyclamate). The chemical structure is unambiguously identified by incorporating a combination of single-crystal X-ray diffraction (SC-XRD), electrospray ionization mass spectrometry (ESI-MS), ^1H nuclear magnetic resonance (NMR) spectroscopy, correlation spectroscopy (COSY), and attenuated total reflection Fourier-transform infrared spectroscopy (ATR-FTIR). The new material: 1) is amongst only several reported structures identified to date incorporating the vital chlorhexidine antimicrobial drug; 2) exhibits broad spectrum antimicrobial activity at concentrations less than $15 \mu\text{g/mL}$; and 3) provides a unique delivery method for the essential active pharmaceutical ingredient (API). Furthermore, substitution of inactive gluconate with

bioactive cyclamate counterion potentially provides the additional benefit of improving the taste profile of chlorhexidine.

4.2. Introduction

Chlorhexidine is a chemical disinfectant and antiseptic with broad antimicrobial activity against a variety of microorganisms including fungi and bacteria.¹ Since its introduction in the 1950's, it has become increasingly ubiquitous in cosmetic, healthcare, and pharmaceutical industries as a preservative, disinfectant, and antiseptic.²⁻⁵ CHX is widely used in mouth rinses for the prevention of plaque formation and development of gingivitis.⁶ In fact, CHX was included in the “World Health Organization (WHO) Model List of Essential Medicines” for antiseptic (*i.e.*, 5% digluconate solution) and neonatal umbilical cord care (*i.e.*, 7.1% digluconate solution or gel) applications.⁷ Due to the fact that the neutral chlorhexidine molecule exhibits low water solubility (*i.e.*, less than 0.1 g/L),⁸ it is typically delivered as an aqueous dication (H_2CHX) salt of an appropriate counterion (Figure 4.1). For example, water soluble salts can be formed by protonating the guanidine groups with gluconic acid (*i.e.*, chlorhexidine digluconate), acetic acid, or hydrochloric acid. Largely attributed to this low solubility and propensity to form micelles in solution, chlorhexidine does not typically crystallize and only five crystal structures of chlorhexidine salts have been reported in the literature over the past 60 years despite its widespread use in global healthcare.⁹

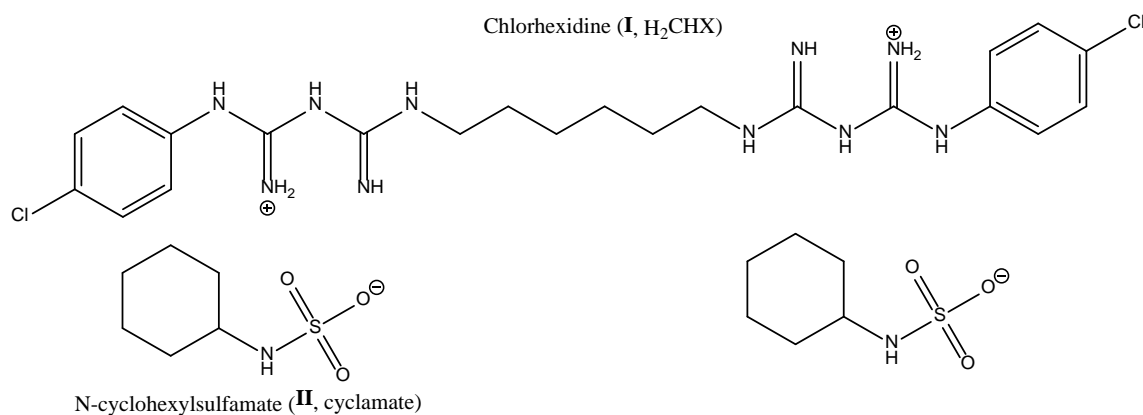


Figure 4.1. Molecular structure of chlorhexidine-cyclamate complex.

In 2008, Dupont *et al.* reported the crystal structures of complexes between CHX and three anionic calix[4]arene derivatives.¹⁰ Nearly a decade later, in 2016, Cattaneo *et al.* reported crystallographic characterization of the hydrated salts of CHX with SO_4^{2-} and CO_3^{2-} .¹¹ However, the effect of the anion on the antimicrobial activity of CHX was not investigated. Herein, we report the crystal structure of a chlorhexidine salt of cyclamate as well as an investigation of the antimicrobial activity of dicyclamate (*i.e.*, CHX-cyclamate or CHC) counterion as compared to digluconate (*i.e.*, CHX-gluconate or CHG) and dihydrochloride (*i.e.*, CHX-HCl) counterparts.

In some cases of chlorhexidine (digluconate) oral treatments, patients often report an initial unpleasant bitter taste while prolonged use often produces taste disturbances which may last for several hours.^{12,13} The presence of these side effects may lead to reduced patient compliance and incomplete antimicrobial effect causing a reduction in overall treatment efficacy. In the current work, an artificial sweetener was utilized as a counterion for chlorhexidine in attempts to mitigate chlorhexidine side effects and thus

enhance its oral treatment compliance. Hence, the biologically inactive gluconate or acetate counterions are replaced by the bioactive and functional cyclamate anion.

Sodium cyclamate is a relatively stable and inexpensive artificial sweetener produced by the sulfonation of cyclohexylamine.^{14,15} Besides its potential capability to mask the bitter taste of CHX, it is known and well-studied that the combination of molecules can have an enhancing or synergistic effect on chemical and physical properties (*e.g.*, antimicrobial activity).¹⁶ In fact, Cavicchioli *et al.* reported how the complexation of cyclamate with Ag(I) caused more than a four-fold reduction in minimum inhibitory concentration (MIC) against *mycobacterium tuberculosis* as compared to AgNO₃.¹⁷

Due to the critical role that CHX plays in human health, a considerable amount of research has been devoted to understanding its antibacterial mechanism.¹⁸ Isotopic labeling studies demonstrated that the uptake of CHX by bacteria occurs rapidly, reaching maximum binding at *ca.* 20 s, and is concentration-dependent.¹⁹ At low concentrations, CHX affects the intracellular cytoplasmic membrane integrity, while at high concentrations it causes congealing of cytoplasm.¹ On the other hand, CHX has little effect on the germination of bacterial spores, exhibits low activity against many viruses, and its effect against mycobacteria is bacteriostatic. It is therefore highly desirable to modulate the chemistry of CHX (*e.g.*, conjugation or complexation with other molecules) as to discover synergistic effects.

4.3. Experimental Section

4.3.1 Synthesis

Synthesis of CHX-cyclamate was carried out in both methanol and water environments. Chlorhexidine digluconate (20 wt.%), chlorhexidine dihydrochloride, and sodium N-cyclohexylsulfamate (referred to as sodium cyclamate herein) were supplied by Sigma-Aldrich (St. Louis, MO). All materials were used as received by manufacturer without further purification.

The aqueous synthesis entailed dropwise addition of an aqueous 1 wt.% sodium cyclamate solution to a 20 wt.% CHG solution, to achieve a 2:1 molar ratio in accordance with charge balance considerations, yielding a precipitate. The heterogeneous mixture was filtered, washed with copious amounts of water, and dried in a 40 °C vacuum. Synthesis in methanol was conducted by combining dilute solutions of chlorhexidine dihydrochloride (0.2 wt.%) and sodium cyclamate (0.14 wt.%) to achieve a final solution comprising 0.1 wt.% chlorhexidine dihydrochloride and (chlorhexidine)(cyclamate)₂ stoichiometry. Slow evaporation of solvent yielded crystal formation.

4.3.2. Characterization

The X-ray diffraction data were collected using Bruker D8 Venture PHOTON 100 CMOS system equipped with a Cu K α INCOATEC ImuS micro-focus source ($\lambda = 1.54178 \text{ \AA}$). The data was collected at 100 K. Indexing was performed using *APEX3* (Difference Vectors method).²⁰ Data integration and reduction were performed using SaintPlus 6.01.²¹ Absorption correction was performed by multi-scan method

implemented in SADABS.²² Space group was determined using XPREP implemented in APEX3.²⁰ The structure was solved using SHELXT (direct methods) and was refined using SHELXL-2017²³⁻²⁵ (full-matrix least-squares on F^2) through OLEX2 interface program.²⁶ All non-hydrogen atoms were refined anisotropically. Hydrogen atoms were placed in geometrically calculated positions and were included in the refinement process using riding model.

Infrared spectra were collected using a Bruker Vertex 70 FTIR spectrometer (Bruker Optics, Billerica, MA) equipped with a GladiATR diamond ATR accessory (Pike technologies, Madison, WI). The spectral range was 80-4000 cm^{-1} with a resolution of 4 cm^{-1} . All measurements were carried out at room temperature on as-prepared samples.

^1H NMR measurements were performed on 1 wt.% samples in deuterated dimethyl sulfoxide (DMSO) solution. All NMR spectra were acquired on a Bruker Avance spectrometer (Bruker-Biospin, Billerica, MA, USA) with a 5 mm BBI probe operating at 500.0 MHz for ^1H at 25 °C. The ^1H NMR resonance of the compounds were further assigned using the homonuclear shift correlation 2D NMR (COSY) method.

LC-MS analysis was performed using a AB Sciex tandem mass spectrometer (AB Sciex LLC, Framingham, MA, USA) equipped with an ESI interface and Agilent 1260 capillary LC system (Model Agilent 1260, Agilent Technologies, Palo Alto, CA, USA). The capillary LC system was equipped with a capillary binary pump (Model G1376A), a DAD detector (G1315C), a micro vacuum degasser (Model G4225A), and a thermostatted column compartment (Model G1316A). The capillary pump was set under the micro-flow mode. Direct injection was used for complex characterization. The

solvent delivery was methanol with a flow rate and injected volume of 70 $\mu\text{L}/\text{min}$ and 1 μL , respectively. The AB Sciex tandem mass spectrometer was operated in both positive and negative ionization modes under the following conditions: nitrogen (>99.99%) was used for curtain gas at 10 psi, ion source gas 1 and 2 at 10 and 10 psi, respectively. ESI IonSpray voltage was set at 5.5 kV for positive and 3.5 kV for negative mode in the ESI interface. The declustering and entrance potential were set up at 80 and 5.5 V, respectively. The temperature of the ionization interface was maintained at 550 $^{\circ}\text{C}$. For total ion count (TIC) mode, the MS screen range was from 50 to 1000 m/z . Data was acquired with an Analyst software 1.6.2 system (AB Sciex LLC, Framingham, MA, USA).

4.3.3. Antimicrobial Assays

Salmonella enterica serovar Typhimurium LT2,²⁷ *Staphylococcus aureus* USA300_LAC²⁸ and *Streptococcus mutans* Clark (ATCC) were used to study the effect of chlorhexidine compounds on survival. *S. enterica* and *S. aureus* were cultured in Muller Hinton media (Sigma-Aldrich) and *S. mutans* was cultured in Reinforced Clostridial Media (Oxoid). Stock solutions for chlorhexidine·2HCl (CHX-HCl; 2.2 mg mL^{-1}) and chlorhexidine cyclamate (CHC; 2 mg mL^{-1}), were prepared by dissolving the compounds in DMSO prior to use. Chlorhexidine gluconate (CHG; 2 mg mL^{-1}) was provided as a 19% w/v solution and further diluted in deionized water.

Growth analyses were conducted as previously described with slight alterations.²⁹ Single bacterial colonies were inoculated into 2 mL of medium in 10 mL capacity culture tubes. Inoculated cultures of *S. aureus* and *S. enterica* were grown aerobically at 37 $^{\circ}\text{C}$

with shaking at 200 rpm for 24 hours. *S. mutans* was cultured statically for 48 hours. End-point Minimum Inhibitory Concentrations (MICs) were determined for CHX-HCl, CHC and CHG using the broth microdilution method from Clinical and Laboratory Standards Institute.³⁰ Overnight cultures were standardized, in triplicates, to 0.5 McFarland standards ($OD_{600} = 0.1$). MICs were determined in cultures grown in 96-well microtiter plates. 100 μ L of the standardized culture was sub-cultured into wells containing 100 μ L of medium containing the antimicrobial compound. Control wells containing 200 μ L of media only or media with antimicrobial compound were used to standardize the data. The microtiter plates were aerobically incubated statically at 37 °C. The *S. aureus* and *S. enterica* cultures were analyzed after 20 hours and *S. mutans* was analyzed after 48 hours. Culture optical densities (A_{600}) were determined using a Biotek EPOCH 2 microplate reader.

4.4. Results and Discussion

Synthesis of CHX-cyclamate was carried out in aqueous and organic (*i.e.*, methanol) solvent using commercially available precursors. Initial observation of complex formation occurred upon mixing cationic chlorhexidine precursors with sodium cyclamate, which yielded precipitation.

The single crystal X-ray diffraction (SC-XRD) analysis, carried out at 100 K, shows that the coordination complex CHX-cyclamate crystallizes in the monoclinic $P2_1/c$ space group. The asymmetric unit consists of half a molecule of protonated chlorhexidine (CHX) cation and one molecule of cyclamate anion. Disordered solvent is also present which was modeled as a water molecule (atom O1) with an occupancy of ~0.5. The

hydrogen atoms of the water could not be modeled accurately. The unit cell parameters and crystallographic details are listed in Table 4.1.

Table 4.1. Crystal data and structure refinement for CHX-cyclamate.

Identification code	CHX-cyclamate
Empirical formula	$C_{36}H_{58}C_{12}N_{10}O_7S_2$
Formula weight	877.94
Temperature/K	99.98
Crystal system	monoclinic
Space group	$P2_1/c$
$a/\text{\AA}$	17.0809(9)
$b/\text{\AA}$	12.7844(7)
$c/\text{\AA}$	9.8602(5)
$\alpha/^\circ$	90
$\beta/^\circ$	93.024(3)
$\gamma/^\circ$	90
Volume/ \AA^3	2150.2(2)
Z	2
$\rho_{\text{calc}}/\text{g/cm}^3$	1.356
μ/mm^{-1}	2.749
F(000)	932.0
Crystal size/ mm^3	$0.152 \times 0.098 \times 0.045$
Radiation	$\text{CuK}\alpha$ ($\lambda = 1.54178$)
2Θ range for data collection/ $^\circ$	5.18 to 149.416

Table 4.1. (continued)

Index ranges	$-21 \leq h \leq 21, -15 \leq k \leq 15, -11 \leq l \leq 12$
Reflections collected	22516
Independent reflections	4384 [$R_{\text{int}} = 0.0820$, $R_{\text{sigma}} = 0.0554$]
Data/restraints/parameters	4384/0/262
Goodness-of-fit on F^2	1.472
Final R indexes [$I \geq 2\sigma(I)$]	$R_1 = 0.0637$, $wR_2 = 0.1833$
Final R indexes [all data]	$R_1 = 0.0794$, $wR_2 = 0.2017$
Largest diff. peak/hole / $e \text{ \AA}^{-3}$	0.99/-0.97

The overall structure consists of symmetrically diprotonated CHX molecule surrounded by two cyclamate units (Figure 4.2) and the structural formula can be described as $[\text{C}_{22}\text{H}_{32}\text{N}_{10}\text{Cl}_2][\text{C}_7\text{H}_{13}\text{O}_3\text{S}]_2$. The CHX molecules adopt a spiral conformation as observed in previous reported structures with the simple CO_3^{2-} and SO_4^{2-} anions but instead of the U-shaped coils,¹¹ they arrange into S-shaped coils (Figure 4.3a). The two Cl ends of the CHX are antiparallel to each other and show weak C-H...Cl hydrogen bonding interactions (3.168 \AA)³¹ with the hydrogens of the cyclamate ring (Figure 4.3b).

The SO_3^- anions from the cyclamate ring form strong to moderate hydrogen bonds (2.059 to 2.706 \AA) with the $-\text{NH}/\text{NH}_2$ groups ($2.064/2.153 \text{ \AA}$ respectively) of three adjacent chlorhexidine cations all arranged in a left-handed conformation. Each CHX unit interacts with four cyclamate units and each of the cyclamate unit shows interaction with two cyclamate units. Interestingly, the cyclamate molecules also show strong hydrogen



Figure 4.2. View of the CHX unit with two cyclamate units.

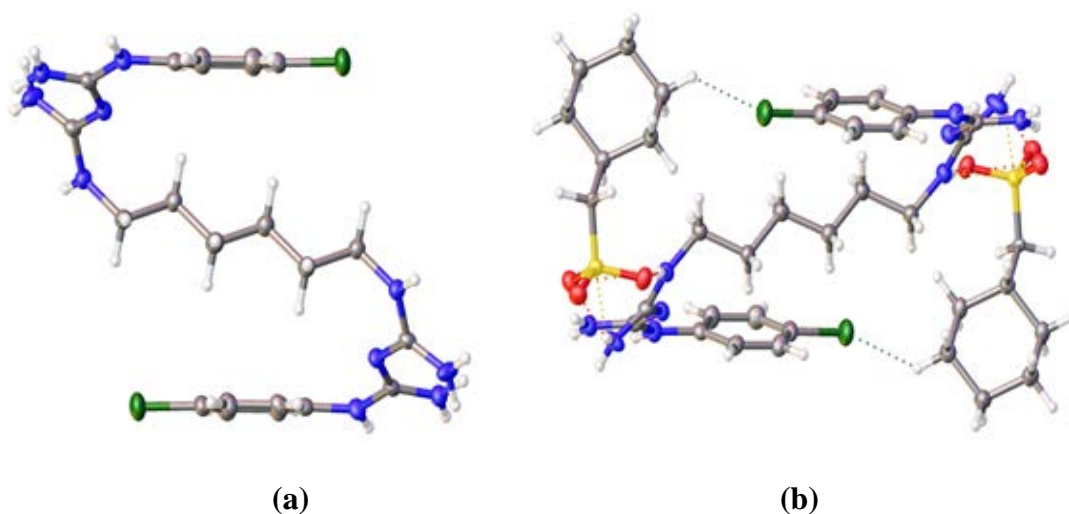


Figure 4.3. (a) The S-shaped CHX coils; and (b) depiction of the C-H...Cl hydrogen bonding interactions.

bonding amongst each other whereby the oxygens of the SO_3^- of one cyclamate interacts with the hydrogens from the $-\text{CH}_2$ of the other cyclamate, forming dimers extending along the c-axis. Adjacent cyclamate molecules alternate with the sulfonate groups pointing at opposing ends giving rise to the dimer network along the b-axis. The water

No significant pi-pi interactions were observed in the structure. The C-N bond lengths within the biguanidine units of CHX showed some delocalization of single and double bonds (1.319-1.363 Å) indicating resonance between the protonated forms. The selected bond lengths and angles are summarized in Tables 4.2 and 4.3, respectively.

Atom	Atom	Length/Å	Atom	Atom	Length/Å
S1	O1	1.464(2)	C4	C5	1.399(4)
S1	C27	1.635(2)	C10	C9	1.527(4)
C11	C1	1.741(3)	C10	C11	1.526(4)
N5	C8	1.324(3)	C25	C26	1.522(4)
N3	C7	1.319(3)	C22	C23	1.521(4)
N2	C7	1.338(4)	C22	C21	1.522(4)
N1	C4	1.411(4)	C1	C2	1.383(4)
N4	C8	1.342(4)	C11	C11 ¹	1.512(6)
C27	C24	1.487(3)	C5	C6	1.386(4)
C4	C3	1.398(4)			

¹2-X,1-Y,-Z

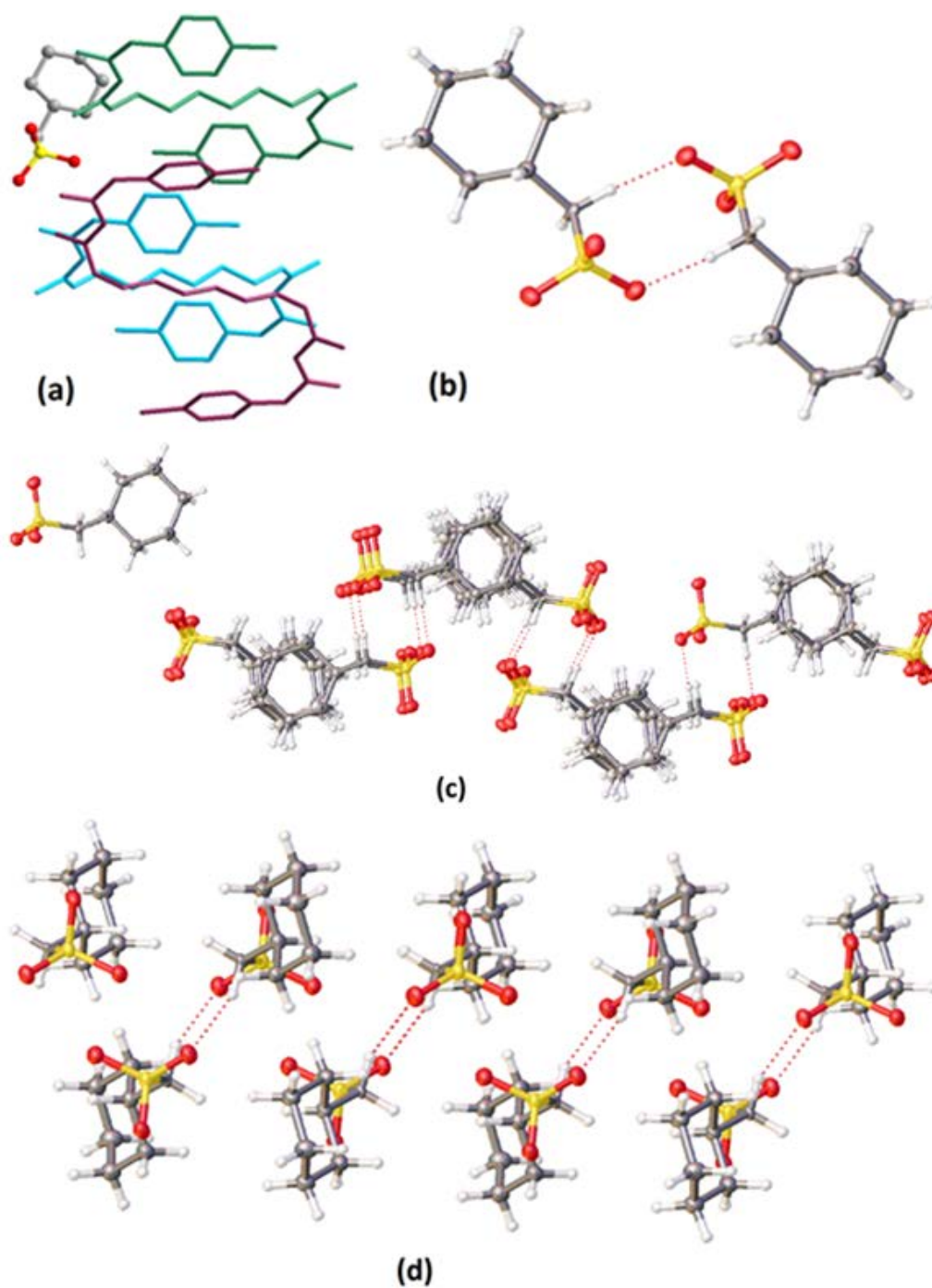


Figure 4.4. (a) The cyclamate showing interaction with three CHX units; (b) the cyclamate dimer; (c) extension of dimers along the c-axis; and (d) alternating cyclamate molecules along the b-axis.

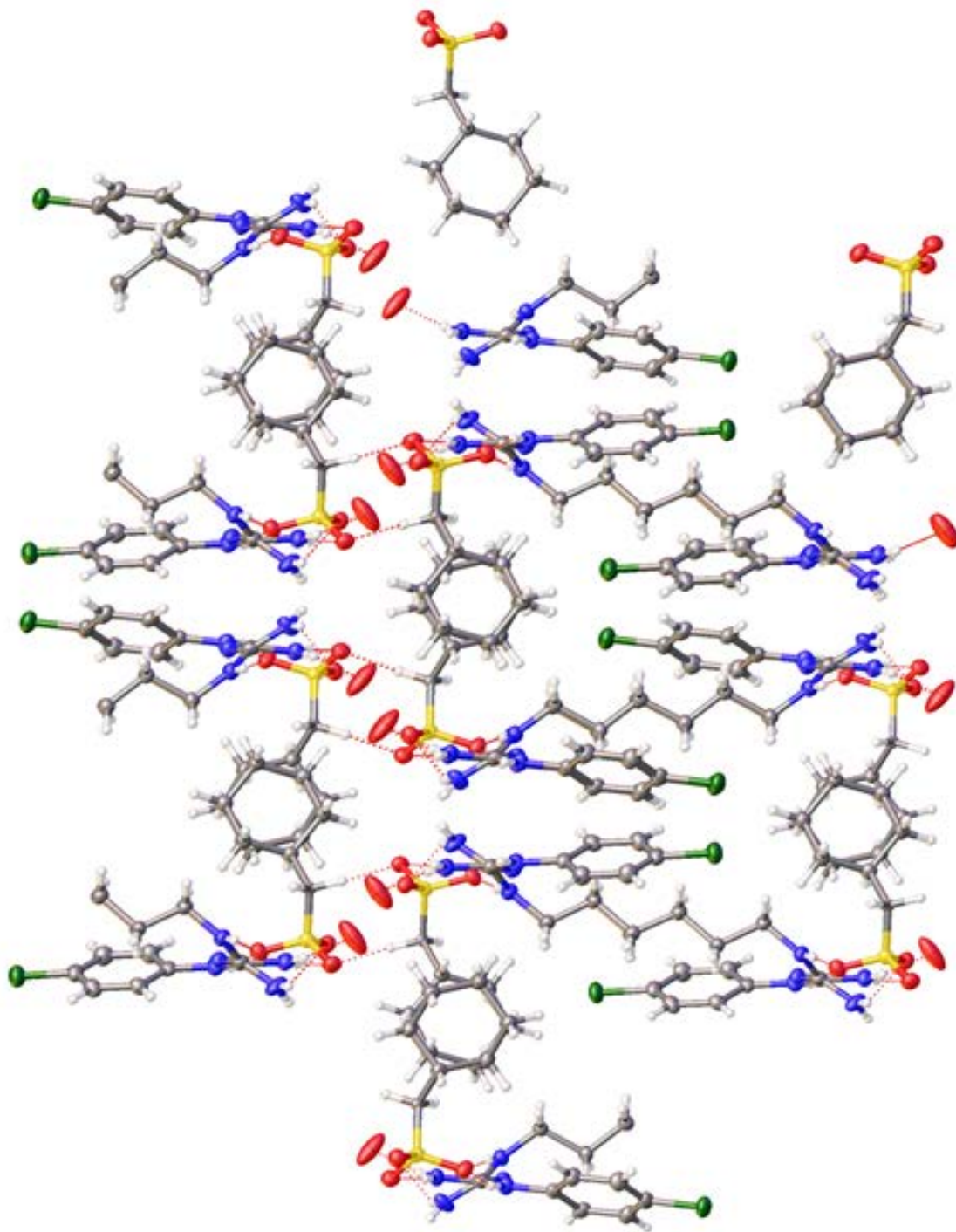


Figure 4.5. Packing arrangement showing the network formation with CHX coils and cyclamate dimers.

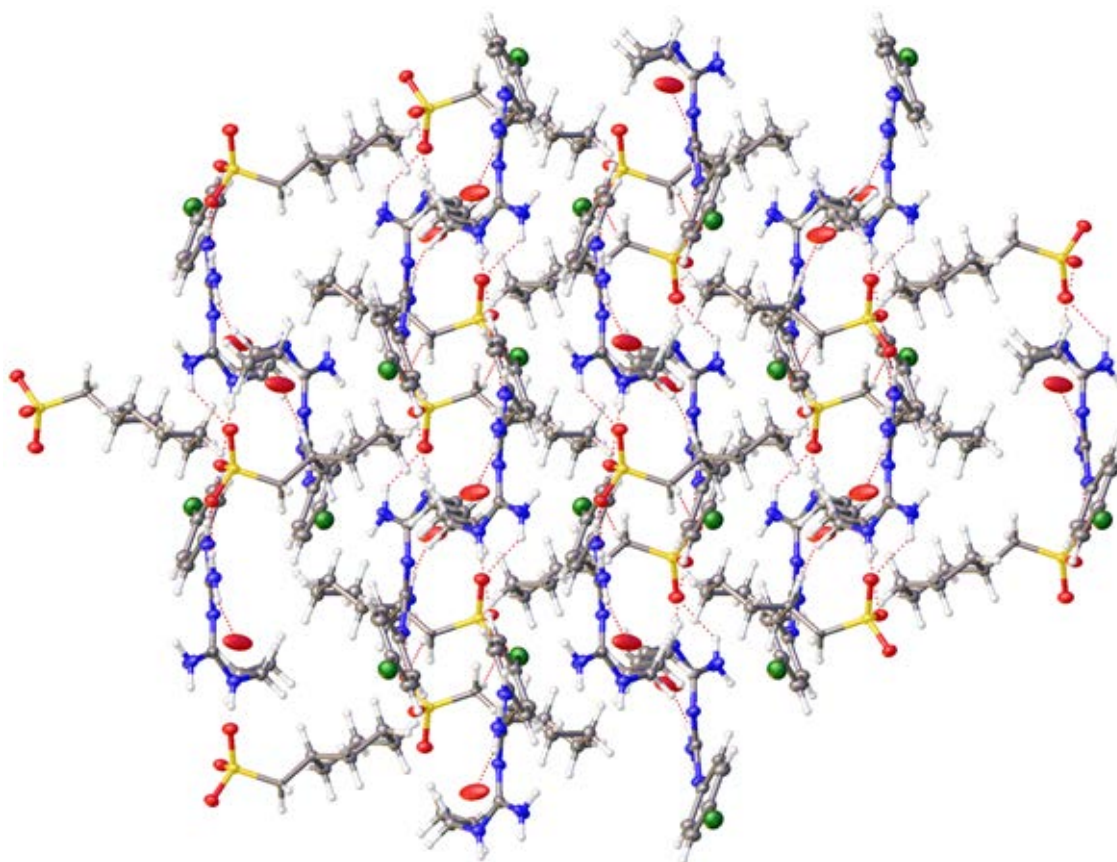


Figure 4.6. View of packing along (100) plane showing alternating cyclamate units.

Table 4.3. Selected bond angles for CHX-cyclamate.

Atom	Atom	Atom	Angle/°		Atom	Atom	Atom	Angle/°
O1	S1	C27	106.09(12)		C27	C24	C25	109.1(2)
C8	N5	C9	123.3(2)		N5	C9	C10	113.5(2)
C24	C27	S1	117.92(17)		C22	C23	C24	111.1(2)
C3	C4	N1	124.3(2)		C2	C1	Cl1	120.1(2)
N3	C7	N2	126.3(2)		C22	C21	C26	111.3(2)
N3	C7	N1	118.2(2)		C1	C6	C5	119.6(3)

The mass spectra of the complex (200 ppm in methanol) are shown in Figures 4.7 and 4.8 with positive and negative modes, respectively. In Figure 4.7, chlorhexidine molecular ion $[M+1]^+$ at $m/z = 505/507$ (chlorine isotopic pattern) and corresponding fragments at $m/z = 335$, 252 and 170 were observed in the positive mode. Based on the formula analysis, the chlorohexidine adducts at $[M+178]$ and $[M+356]$ were identified. The same evidence was observed in the negative mode (Figure 4.8). To confirm the adduct presence, MS/MS experiments were conducted (Figures 4.9-4.11). In Figure 4.9, the parent ion was locked at $m/z = 681$ ($Cl = 35$) and the daughter ion at $m/z = 178$ was observed in the negative mode. In Figure 4.10, the parent ion was locked at $m/z = 683$ ($Cl = 35$) and the daughter ion was observed at $m/z = 505$ ($Cl = 35$) in the positive mode. In Figure 4.11, the parent ion was locked at $m/z = 863$ ($Cl = 35$) and the daughter ion was observed at $m/z = 505$ ($Cl = 35$) in the positive mode.

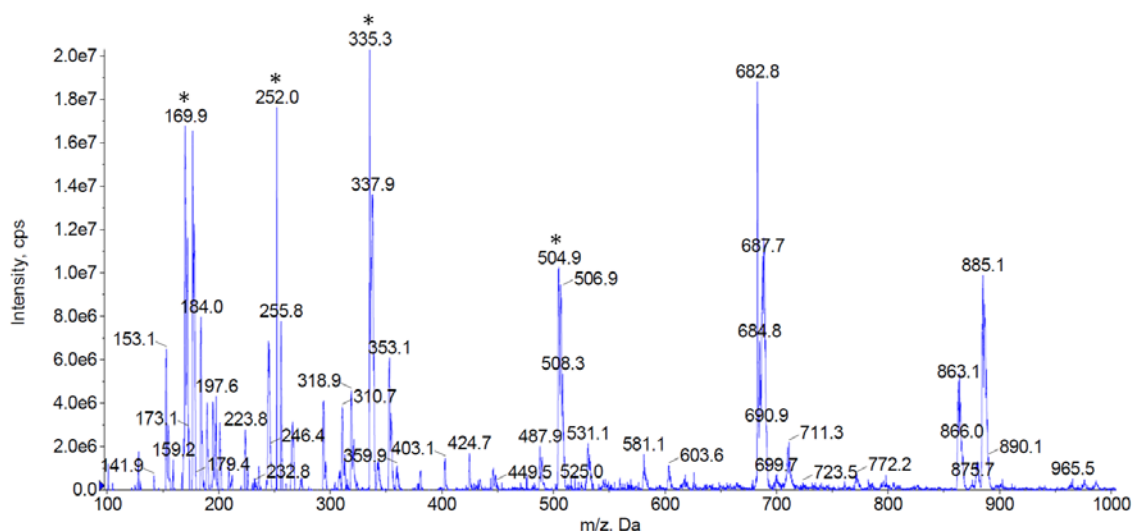


Figure 4.7. Mass spectrum (positive mode) of CHX-cyclamate complex in methanol. Peaks denoted with an asterisk correspond to the molecular chlorhexidine ion ($m/z = 504.9$) and its corresponding fragments.

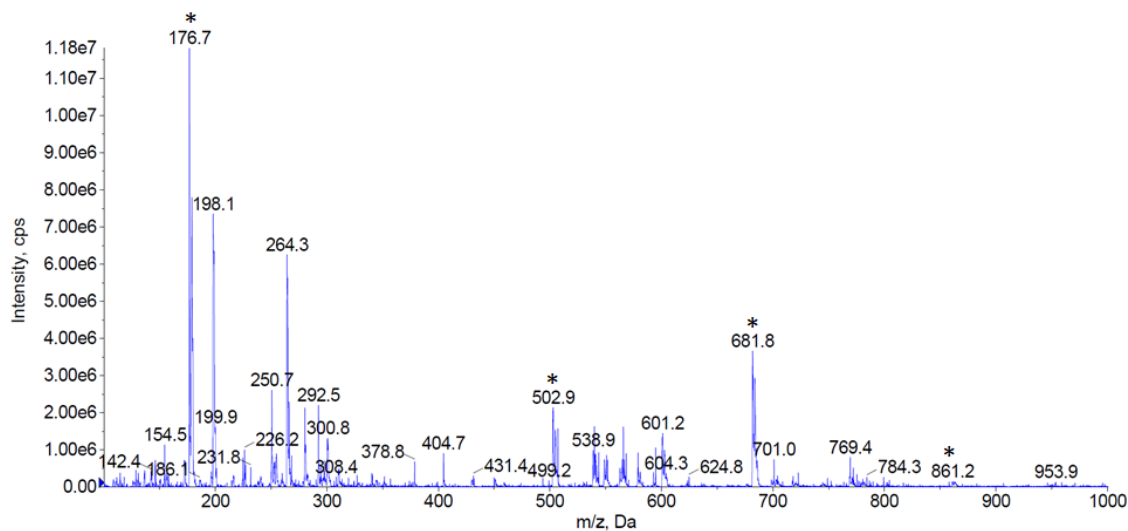


Figure 4.8. Mass spectrum (negative mode) of CHX-cyclamate complex in methanol. Peaks from left to right (denoted with an asterisk): cyclamate, chlorhexidine anion, 1:1 chlorhexidine-cyclamate anionic adduct, and 1:2 chlorhexidine-cyclamate anionic adduct.

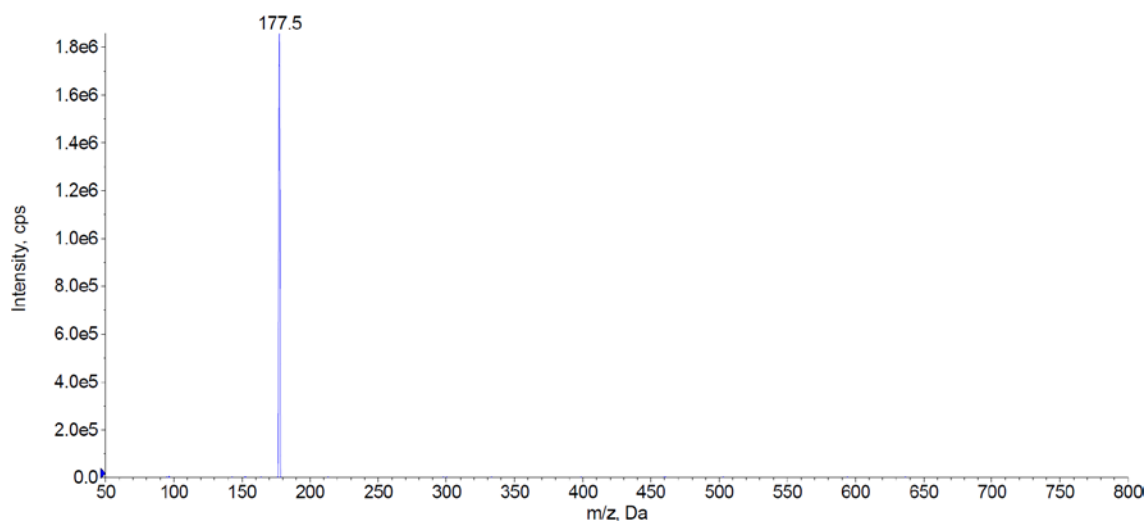


Figure 4.9. MS/MS spectrum (negative mode) from the parent ion at m/z = 681.

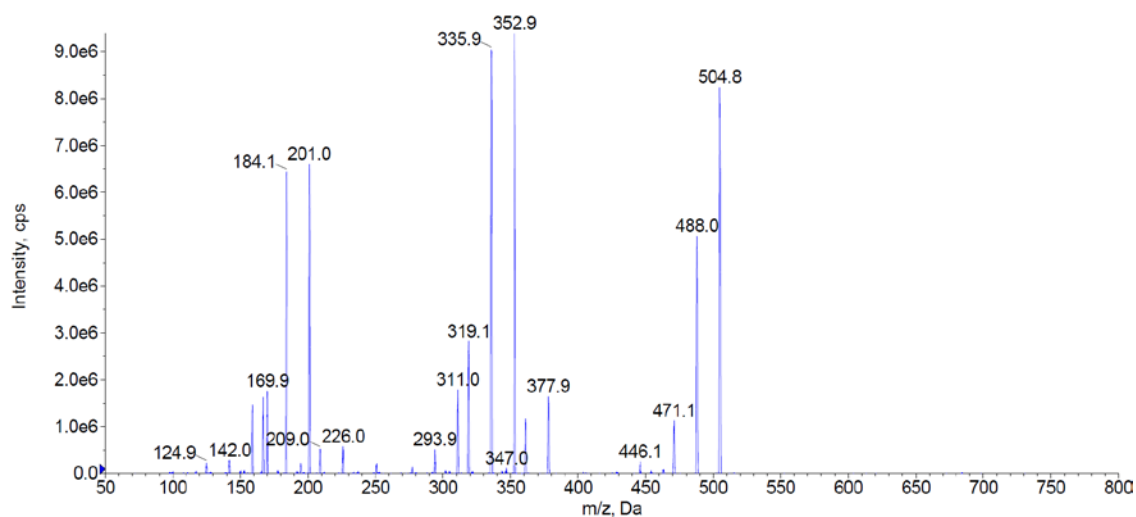


Figure 4.10. MS/MS spectrum (positive mode) from the parent ion at $m/z = 683$.

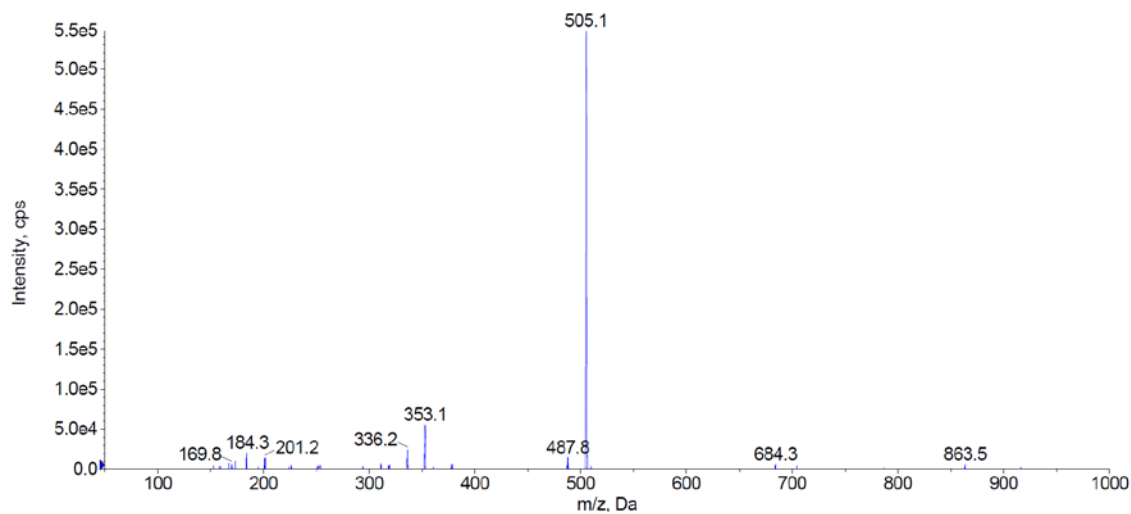


Figure 4.11. MS/MS spectrum (positive mode) from the parent ion at $m/z = 863$.

Figure 4.12 compares the infrared absorption spectra of CHX-cyclamate samples prepared in two different solvents (methanol and water) to the sodium N-cyclohexylsulfamate, chlorhexidine dihydrochloride and lyophilized chlorhexidine

digluconate raw materials. Presence of both components (*i.e.*, chlorhexidine and cyclamate) is immediately apparent in the spectra of CHX-cyclamate samples. As an example, chlorhexidine bands corresponding to $\nu(\text{C}=\text{C})$, $\nu(\text{C}=\text{N})$ and $\delta(\text{NH}_2)$ vibrations are clearly evident in the region above 1480 cm^{-1} where sodium cyclamate has no infrared absorption.³³⁻³⁵ Similarly, N-H stretching vibrations of -NH, =NH and NH_2 functional groups of chlorhexidine can be identified in the $3000\text{--}3500\text{ cm}^{-1}$ high frequency range. The cyclamate component is manifested for instance, by the two prominent sets of bands near the 1030 and 1170 cm^{-1} region, associated with as/sym (SO_2) vibrations.³⁶⁻³⁷ Evidence of both precursors in the prepared samples along with the fact that the vibrational bands are significantly different in their shape and positions from

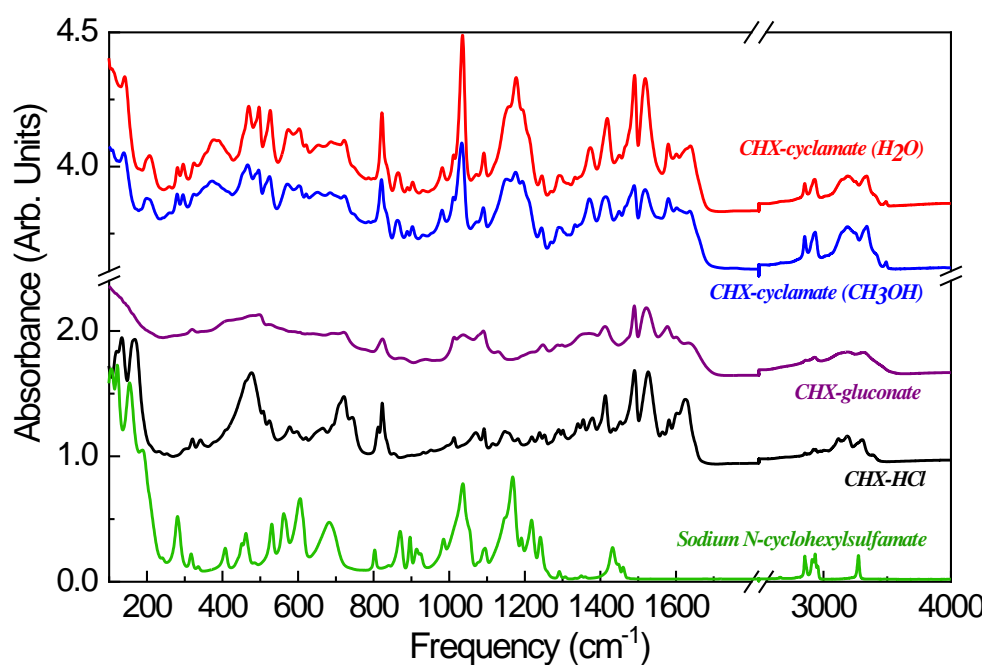


Figure 4.12. FTIR spectra of sodium N-cyclohexylsulfamate, CHX-HCl, CHX-gluconate, CHX-cyclamate crystals prepared from methanol and water. Spectra are offset for clarity.

the initial raw materials suggests the formation of the complex between chlorhexidine and cyclamate ions. Finally, comparison of the spectrum of CHX-cyclamate synthesized in methanol versus water reveals that the two samples display overall similar vibrational profiles with some variations in their relative bands' intensities likely originating from the small differences in the purity and local structure of the two samples.

^1H NMR spectroscopy (Figure 4.13) and COSY (Figure 4.14) confirmed that both chlorhexidine and cyclamate exist in the crystal dissolved in DMSO. The ^1H NMR chemical shifts corresponding to specific protons of chlorhexidine and cyclamate are indicated in Figure 4.13. Specifically, the ^1H NMR spectrum showed the presence of signals for the benzene rings of CHX, resonating at 7.34 and 7.38 ppm, as well as characteristic signals of methylene protons of CHX at 1.04, 1.46, and 3.06 ppm. In addition, the methylene protons of the cyclohexane ring of cyclamate were identified at 1.16, 1.61, 1.88, 2.87 ppm. Due to the line broadening of the sample, the proton J coupling was not clearly observed. COSY was further performed to confirm the peak assignment of the NMR spectrum. According to peak integrals in Figure 4.13, the stoichiometric ratio between chlorhexidine and cyclamate is 1:2.

The ability of CHX-HCl, CHC and CHG to inhibit the growth of the bacterial pathogens *Staphylococcus aureus* LAC, *Streptococcus mutans*, and *Salmonella enterica* serovar Typhimurium was examined. *S. aureus* LAC is a gram-positive community-associated methicillin-resistant CA-MRSA strain and a representative strain of the USA300 clone, which is a leading cause of skin and soft tissue infections in North America.³⁸ *S. mutans* is also gram-positive and the leading causes of dental caries.³⁹ *Salmonella enterica* serovar Typhimurium is a gram-negative and a primary enteric

pathogen affecting humans.⁴⁰

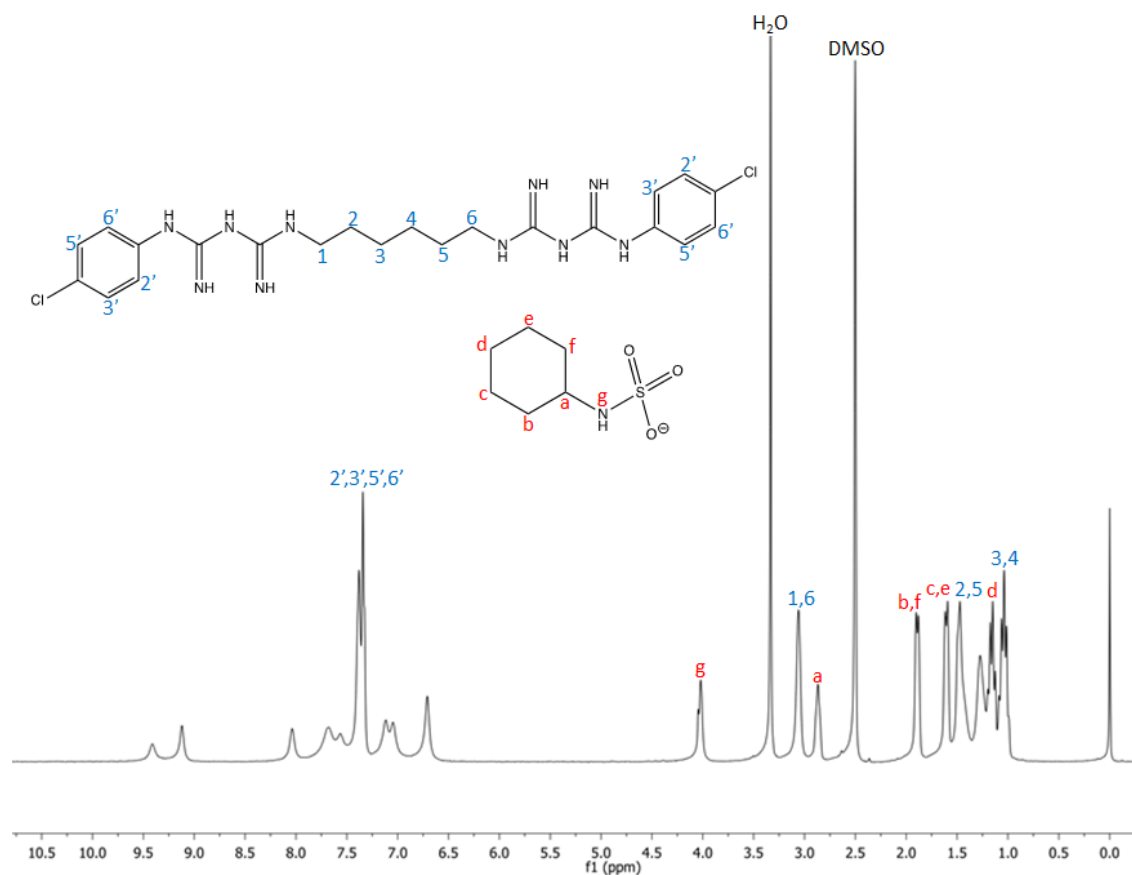


Figure 4.13. ¹H NMR spectroscopy of crystal dissolved in deuterated DMSO.

The MICs of CHX-cyclamate, CHX-gluconate, and CHX-HCl were determined in a liquid culture after static growth. All of the three bacteria displayed typical dose-responses to the compounds utilized (Figure 4.15-4.16). The MICs for CHX-cyclamate, CHX-gluconate, and CHX-HCl are reported in Table 4.4 for *S. mutans*, *S. aureus*, and *S. enterica*. CHX-HCl demonstrated the lowest MIC values for all tested bacteria,

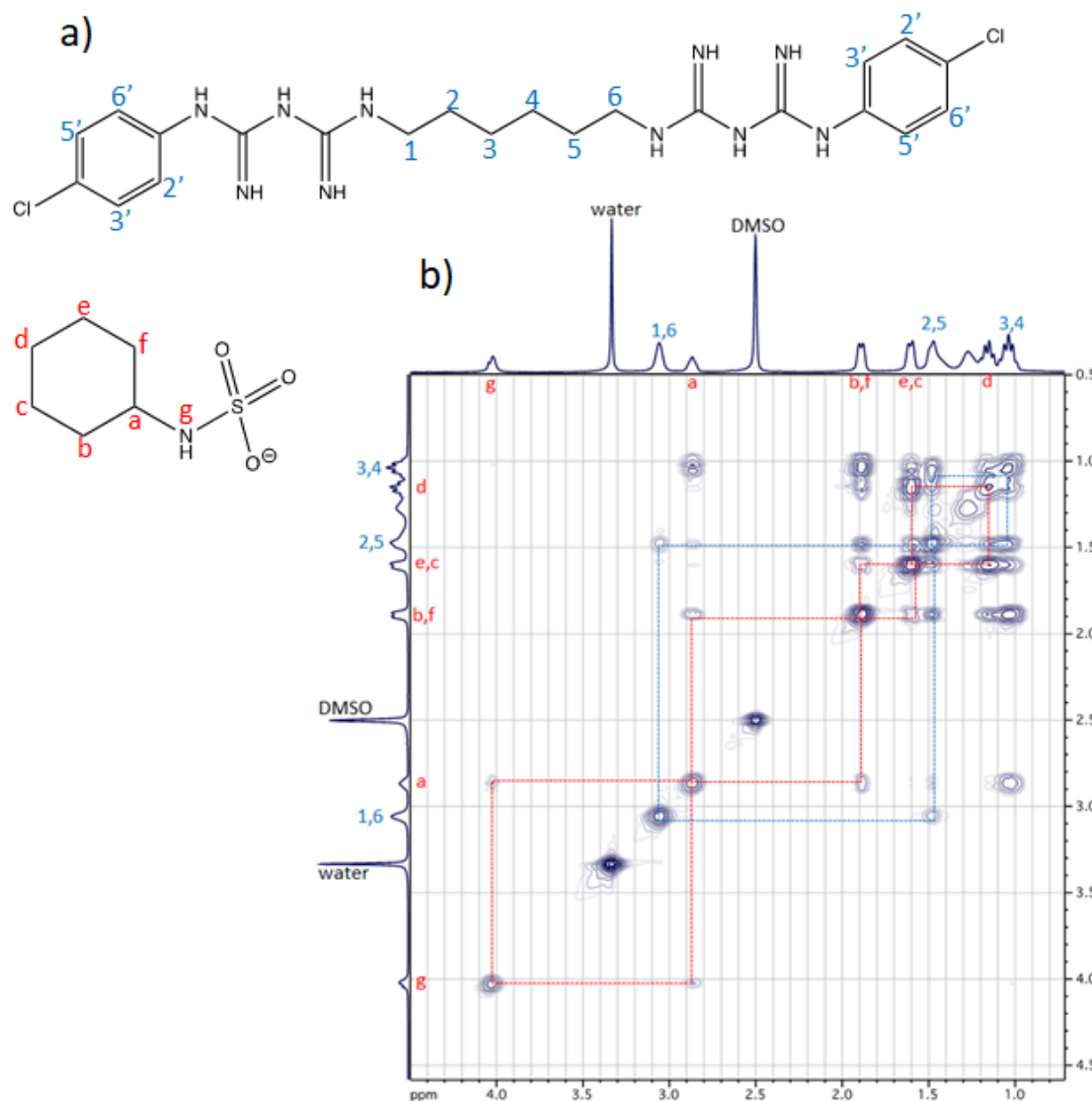


Figure 4.14. Chlorhexidine and cyclamate structures (a) with labelled protons and their corresponding COSY spectrum (b) illustrating chlorhexidine (blue) and cyclamate (red) proton coupling.

potentially due to the additional cellular toxicity provided by the coordinated strong acid. The gluconate and cyclamate counterparts exhibited parity efficacy versus the oral strain *S. mutans*. CHX-cyclamate was slightly less effective against *S. aureus* and more so

against *S. enterica*. Nevertheless, all of the three tested compounds were on the same order of efficacy with efficient gram-positive and gram-negative bacteria inhibition at ppm concentration levels. Based on this data, we posit that the cyclamate counterion does not deactivate chlorhexidine's antimicrobial mode of action. The MIC values for CHX-gluconate are in good agreement with those reported in literature.⁸

Table 4.4. MIC values for CHX-cyclamate, CHX-gluconate, and CHX-HCl.

Compound	Minimum inhibitory concentration (MIC)		
	<i>S. mutans</i> ($\mu\text{g mL}^{-1}$)	<i>S. aureus</i> ($\mu\text{g mL}^{-1}$)	<i>S. enterica</i> ($\mu\text{g mL}^{-1}$)
CHX-HCl	1.5	2.0	7.0
CHX-gluconate	2.5	3.5	7.5
CHX-cyclamate	2.5	5.0	12.0

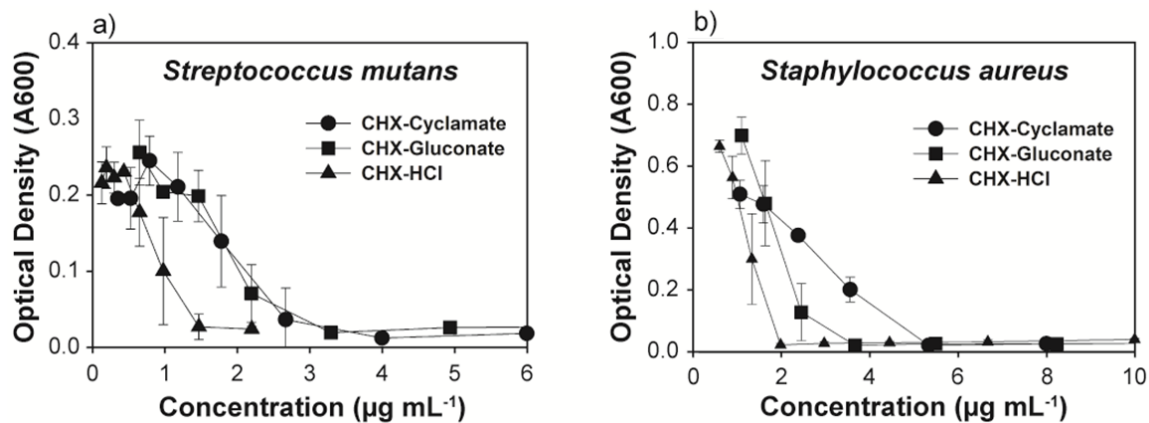


Figure 4.15. MIC assays for CHX-cyclamate, CHX-gluconate, and CHX-HCl with (a) *S. mutans* and (b) *S. aureus*.

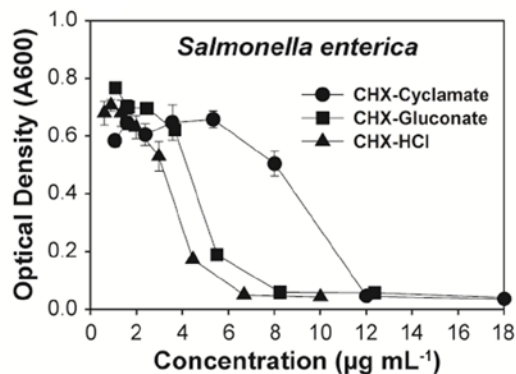


Figure 4.16. MIC assay for CHX-cyclamate, CHX-gluconate, and CHX-HCl with *S. enterica*.

4.5. Conclusion

A novel complex of an essential antimicrobial drug chlorhexidine was synthesized, characterized, and evaluated for its antibacterial properties. Substitution of the biologically inert gluconate anion with the bioactive N-cyclohexylsulfamate, an artificial sweetener known as cyclamate, counterpart yielded a material which can potentially enhance the taste profile while maintaining parity antimicrobial efficacy against *S. mutans* which is known to cause dental caries. The novel material is an important progression to the solid state understanding of an indispensable biocide which does not easily crystallize under normal conditions. Moreover, the newly developed technology furthers our understanding of CHX and paves the way for further research to improve the current leading antimicrobial treatment in a worldwide campaign to promote oral and overall healthcare.

4.6. References

- (1) McDonnell, G.; Russell, A. D., Antiseptics and disinfectants: Activity, action, and resistance. *Clin. Microbiol. Rev.* **1999**, *12* (1), 147-179.
- (2) Emilson, C. G., Potential efficacy of chlorhexidine against mutans streptococci and human dental caries. *J. Dent. Res.* **1994**, *73* (3), 682-91.
- (3) Addy, M., Chlorhexidine compared with other locally delivered antimicrobials. A short review. *J. Clin. Periodontol.* **1986**, *13* (10), 957-64.
- (4) Milstone, A. M.; Passaretti, C. L.; Perl, T. M., Chlorhexidine: expanding the armamentarium for infection control and prevention. *Clinical infectious diseases : an official publication of the Infectious Diseases Society of America* **2008**, *46* (2), 274-81.
- (5) Block, S. S., *Disinfection, Sterilization, and Preservation*. 5th ed.; Lippincott Williams & Wilkins: Philadelphia, PA.
- (6) Addy, M., Chlorhexidine compared with other locally delivered antimicrobials. *J. Clin. Periodontol.* **1986**, *13* (10), 957-964.
- (7) WHO Model List of Essential Medicines 2017. World Health Organization. 2017. [cited 2020 Jan 16]. Available from: <http://www.who.int/medicines/publications/essentialmedicines/en/>
- (8) Paulus, W., *Directory of Microbicides for the Protection of Materials*. Kluwer Academic Publishers: The Netherlands, 2004.
- (9) Groom, C. R.; Bruno, I. J.; Lightfoot, M. P.; Ward, S. C., The Cambridge structural database. *Acta Crystallogr. B* **2016**, *72* (2), 171-179.
- (10) Dupont, N.; Lazar, A. N.; Perret, F.; Danylyuk, O.; Suwinska, K.; Navaza, A.; Coleman, A. W., Solid state structures of the complexes between the antiseptic chlorhexidine and three anionic derivatives of calix[4]arene. *CrystEngComm* **2008**, *10* (8), 975-977.
- (11) Cattaneo, D.; McOrmick, L. J.; Cordes, D. B.; Slawin, A. M. Z.; Morris, R. E., Crystal structure resolution of two different chlorhexidine salts. *J. Mol. Struct.* **2016**, *1121*, 70-73.
- (12) Flotra, L.; Gjermo, P.; Rolla, G.; Waerhaug, J., Side effects of chlorhexidine mouth washes. *Eur. J. Oral Sci.* **1971**, *79* (2), 119-125.
- (13) Lang, N.; Brex, M. C., Chlorhexidine digluconate—an agent for chemical plaque control and prevention of gingival inflammation. *J. Periodontal Res.* **1986**, *21* (s16), 74-89.
- (14) Chattopadhyay, S.; Raychaudhuri, U.; Chakraborty, R., Artificial sweeteners - a review. *J. Food Sci. Technol.* **2014**, *51* (4), 611-621.
- (15) McKetta, J. J., *Encyclopedia of Chemical Processing and Design*. Marcel Dekker, Inc.: New York, 1996.
- (16) Bollenbach, T., Antimicrobial interactions: mechanisms and implications for drug discovery and resistance evolution. *Curr. Opin. Microbiol.* **2015**, *27*, 1-9.
- (17) Cavicchioli, M.; Leite, C. Q. F.; Sato, D. N.; Massabni, A. C., Synthesis, characterization and antimycobacterial activity of Ag(I)-aspartame, Ag(I)-saccharin and Ag(I)-cyclamate complexes. *Archiv der Pharmazie* **2007**, *340* (10), 538-542.

- (18) Ranganathan, N. S., Handbook of disinfectants and antiseptics. Ascenzi, J. M., Ed. Marcel Dekker, Inc.: New York, 1996; pp 235-264.
- (19) Fitzgerald, K. A.; Davies, A.; Russell, A. D., Uptake of ^{14}C -chlorhexidine diacetate to *Escherichia coli* and *Pseudomonas aeruginosa* and its release by azolectin. *FEMS Microbiol. Lett.* **1989**, *60* (3), 327-332.
- (20) Bruker APEX3 (Version 2015.9), Bruker AXS Inc.: Madison, Wisconsin, USA, 2016.
- (21) Bruker SAINT-V8.35A. *Data Reduction Software*, Madison, Wisconsin, USA, 2016.
- (22) Sheldrick, G. M. SADABS. *Program for Empirical Absorption Correction*, University of Gottingen: Germany, 1996.
- (23) Sheldrick, G., Crystal structure refinement with SHELXL. *Acta Cryst. C* **2015**, *71* (1), 3-8.
- (24) Sheldrick, G., Phase annealing in SHELX-90: direct methods for larger structures. *Acta Cryst. A* **1990**, *46* (6), 467-473.
- (25) Sheldrick, G., A short history of SHELX. *Acta Cryst. A* **2008**, *64* (1), 112-122.
- (26) Dolomanov, O. V.; Bourhis, L. J.; Gildea, R. J.; Howard, J. A. K.; Puschmann, H., OLEX2: a complete structure solution, refinement and analysis program. *J. Appl. Crystallogr.* **2009**, *42* (2), 339-341.
- (27) Boyd, J. M.; Teoh, W. P.; Downs, D. M., Decreased transport restores growth of a *Salmonella enterica* apbC mutant on tricarballylate. *J. Bacteriol.* **2012**, *194* (3), 576-583.
- (28) Roberts, C. A.; Al-Tameemi, H. M.; Mashruwala, A. A.; Rosario-Cruz, Z.; Chauhan, U.; Sause, W. E.; Torres, V. J.; Belden, W. J.; Boyd, J. M., The suf iron-sulfur cluster biosynthetic system is essential in *Staphylococcus aureus*, and decreased suf function results in global metabolic defects and reduced survival in human neutrophils. *Infect. Immun.* **2017**, *85* (6).
- (29) Dubovoy, V.; Ganti, A.; Zhang, T.; Al-Tameemi, H.; Cerezo, J. D.; Boyd, J. M.; Asefa, T., One-pot hydrothermal synthesis of benzalkonium-templated mesostructured silica antibacterial agents. *J. Am. Chem. Soc.* **2018**, *140* (42), 13534-13537.
- (30) *Methods for Dilution Antimicrobial Susceptibility Tests for Bacteria That Grow Aerobically; Approved Standard - Ninth Edition*. Clinical and Laboratory Standards Institute: Wayne, PA, 2012.
- (31) B. Aakeröy, C.; A. Evans, T.; R. Seddon, K.; Pálinkó, I., The C–H...Cl hydrogen bond: does it exist? *New J. Chem.* **1999**, *23* (2), 145-152.
- (32) Jeffrey, G. A. J.; Jeffrey, G. A., *An Introduction to Hydrogen Bonding*. Oxford University Press: 1997.
- (33) Călinescu, M.; Negreanu-Pîrjol, T.; Georgescu, R.; Călinescu, O., Synthesis and characterization of new copper(II) complex compounds with chlorhexidine. Part I. In *Open Chem.*, 2010; Vol. 8, p 543.
- (34) Luo, D.; Shahid, S.; Wilson, R. M.; Cattell, M. J.; Sukhorukov, G. B., Novel formulation of chlorhexidine spheres and sustained release with multilayered encapsulation. *ACS Appl. Mater. Interfaces* **2016**, *8* (20), 12652-60.

- (35) Rema, T.; Lawrence, J. R.; Dynes, J. J.; Hitchcock, A. P.; Korber, D. R., Microscopic and spectroscopic analyses of chlorhexidine tolerance in *Delftia acidovorans* biofilms. *Antimicrob. Agents Chemother.* **2014**, 58 (10), 5673-86.
- (36) Katiyar, R. S., Raman and infra-red spectra of crystalline potassium sulphamate. *Proc. Indian Acad. Sci.* **1965**, 62 (3), 169-175.
- (37) Ilczyszyn, M. M.; Ilczyszyn, M., Raman, infrared and ^{13}C NMR studies on betaine–sulfamic acid (2:1) crystal and its hydrogen bonds. *J. Raman Spectrosc.* **2003**, 34 (9), 693-704.
- (38) Planet, P. J., Life after USA300: The rise and fall of a superbug. *J. Infect. Dis.* **2017**, 215, S71-S77.
- (39) Loesche, W. J., Role of *Streptococcus mutans* in human dental decay. *Microbiol. Rev.* **1986**, 50 (4), 353.
- (40) Fàbrega, A.; Vila, J., *Salmonella enterica* serovar Typhimurium skills to succeed in the host: virulence and regulation. *Clin. Microbiol. Rev.* **2013**, 26 (2), 308.

CHAPTER 5

Conclusions and Perspectives

In late 1928, as a result of a serendipitous accident, professor Alexander Fleming observed a peculiar zone of inhibition forming in a Petri dish of a *Staphylococci* bacteria which was mistakenly left open overnight and contaminated with the mold *Penicillium chrysogenum*. The Scottish scientist concluded that the mold released a substance that inhibited the growth and resulted in lysing of the bacteria. Throughout the next fourteen years, multinational collaborations resulted in the isolation, clinical evaluation, and commercialization of the first true antibiotic drug, penicillin. This new wonder drug revolutionized healthcare and paved the way for many of the greatest medical advances of the 20th century. Common, yet at the time often deadly bacterial infections occurring as a result of a small cut or routine surgery could be treated effectively with a relatively small amount of the antibiotic. Countless lives have been saved as a result of the efforts of Alexander Fleming, Ernst Boris Chain, and Howard Walter Florey (who were ultimately credited with the discovery and commercialization of penicillin in the 1945 Nobel Prize) and the subsequent pioneers of modern medicine. However, microorganisms (*e.g.*, bacteria) have always evolved as to become resistant to the medicine which is used to inhibit their proliferation. This concept, antimicrobial resistance (AMR), is giving rise to new groups of antibiotic-resistant bacteria (*e.g.*, methicillin-resistant *Staphylococcus aureus* (MRSA)) and pose a significant challenge for improving global healthcare. In fact, due to the slowing rate of discovering novel antibiotics and increasing rate of antibiotic use, it is projected that in the year 2050 as many as 10 million deaths

worldwide will be caused by AMR-related infections (Figure 5.1). One approach to dealing with this growing problem is to develop or discover antimicrobial technology where the bacteria or other pathogens are simultaneously attacked by a synergistic or cooperative combination of growth-inhibiting processes. The research embodied herein, collectively comprising my doctorate dissertation, stem from this urgent need to redefine the drugs and methodologies utilized to treat antimicrobial infections.

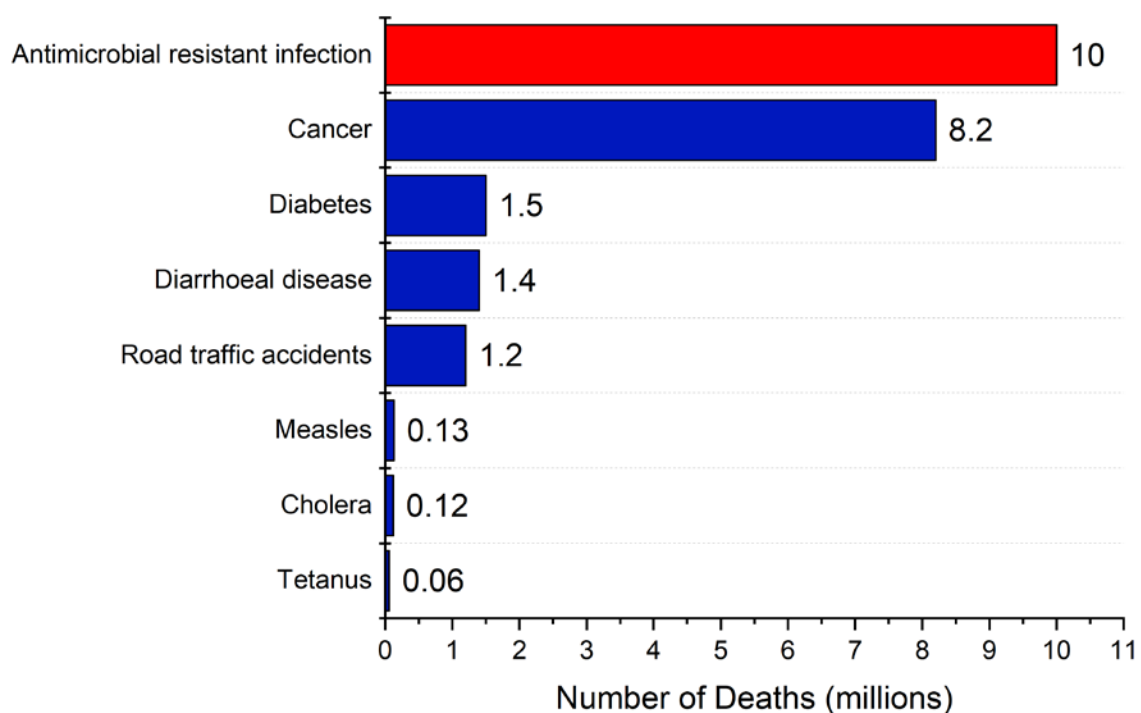


Figure 5.1. Projected deaths (per year) attributable to antimicrobial resistance infections compared to other major causes of death in 2050.¹

In the synthesis of benzalkonium-templated MSNs, a quaternary ammonium surfactant commonly referred to as benzalkonium chloride (BAC) was used as a template to synthesize mesostructured silica nanoparticles with a relatively high density (0.56 g

per 1 g of SiO₂) of BAC and a high surface area (1500 m² g⁻¹) MSN upon calcination.² The inorganic-organic composite material demonstrated a pH-responsive controlled release of BAC in the physiologically-relevant pH range of 4.0 to 7.4. Moreover, the material demonstrated inhibition of the gram-positive *Staphylococcus aureus* and the gram-negative *Salmonella enterica* at 10 and 130 mg/L, respectively. Considering that the tested material comprised *ca.* 36 wt.% loading content of BAC and a release of *ca.* 8% of the total loaded content within 72 hrs, this is a 10-fold enhancement compared to the minimum inhibitory concentration (MIC) of 40 mg/L for pure BAC.³ These results suggest that either the release of BAC (or other drug) from the MSNs is not a prerequisite for bactericidal efficacy or the host-guest relationship between BAC and silica MSNs in some way boosts antimicrobial activity, which warrants further investigation.

On a different note, we explored synthesizing novel materials comprising cetylpyridinium chloride (CPC) in efforts to enhance its antimicrobial efficacy. Cetylpyridinium tetrachlorozincate, a complex comprising CPC and ZnCl₂ with the stoichiometry of C₄₂H₇₆Cl₄N₂Zn, was synthesized and its solid-state structure was elucidated *via* single crystal X-ray diffraction (SC-XRD). The material showed parity or potentially enhanced (*e.g.*, MIC against *S. mutans*) antimicrobial efficacy despite the fact that *ca.* 16% of the bactericidal CPC is replaced with bacteriostatic ZnCl₂ in the structure. Methodology to load the novel material into porous frameworks was proposed yielding a material with *ca.* 9.0 and 8.9 wt.% of CPC and Zn, respectively. One possible route to expand upon this concept and enhance the antimicrobial efficacy even further is to replace Zn, which can be described as bacteriostatic due to its relatively weak

antimicrobial activity, with another metal (*e.g.*, Ag) which demonstrates significantly stronger antimicrobial action.

Chlorhexidine is another important biocide, due to its broad spectrum antimicrobial efficacy and relatively low MIC concentration, which was investigated herein. A novel complex, comprising chlorohexidine and N-cyclohexylsulfamate (referred to herein as cyclamate) with the stoichiometry $[C_{22}H_{32}N_{10}Cl_2][C_7H_{13}O_3S]_2$, was synthesized, crystal structure elucidated, and antimicrobial efficacy evaluated. This newly discovered material exhibits excellent antimicrobial activity with an MIC of 2.5 $\mu\text{g/mL}$ for *Streptococcus mutans* (*i.e.*, the gram-positive bacteria known to cause dental caries). Additional advantageous of chlorhexidine dicyclamate are manifested by the substitution of the inactive gluconate anion with the bioactive cyclamate artificial sweetener which has the capability to mask the bitter taste of chlorhexidine. Future research on enhancing the benefits of chlorhexidine can focus on developing new chemical moieties based on the bisguanide backbone as well as complexation of chlorhexidine with anions which may synergistically or cooperatively boost the antimicrobial efficacy of the molecule.

In summary, the design, synthesis, characterization, and application of various novel antimicrobial technology based on quaternary ammonium compounds is demonstrated in this thesis. The incorporation of quaternary ammonium compounds into mesoporous silica frameworks *via* soft-templating method proved to be an efficient method to fabricate an inorganic-organic composite material with excellent broad spectrum antimicrobial efficacy. Complexation of CPC with $ZnCl_2$ yielded another inorganic-organic composite material which demonstrates parity antimicrobial efficacy as compared to CPC at a lower CPC concentration. Moreover, combining chlorhexidine

with N-cyclohexylsulfamate produced a broad spectrum biocide which may be preferred for treatments of plaque build-up and mild gingivitis as compared to chlorhexidine gluconate. The aforementioned works demonstrate the advantages of rational combination or complexation of quaternary ammonium biocides with either inorganic moieties or organic bioactive molecules in efforts to combat the next generation of antibiotic-resistant bacteria such as MRSA. As we continually improve our understanding of bactericidal mode of actions and the chemical moieties that facilitate them, the next breakthrough eagerly awaits us. This much needed breakthrough will likely be a result of worldwide perseverance and collaboration as well as a little serendipity (as in the case of the discovery of penicillin).

References

- (1) O'Neill, J. *Antimicrobial Resistance: Tackling a crisis for the health and wealth of nations*; Review on Antimicrobial Resistance: 2015.
- (2) Dubovoy, V.; Ganti, A.; Zhang, T.; Al-Tameemi, H.; Cerezo, J. D.; Boyd, J. M.; Asefa, T., One-pot hydrothermal synthesis of benzalkonium-templated mesostructured silica antibacterial agents. *J. Am. Chem. Soc.* **2018**, *140* (42), 13534-13537.
- (3) Fazlara, A.; Ekhtelat, M., The disinfectant effects of benzalkonium chloride on some important foodborne pathogens. *Am. Eurasian J. Agric. Environ. Sci.* **2012**, *12* (1), 23-29.

Appendix



RightsLink®

[Home](#)
[Account Info](#)
[Help](#)


ELSEVIER

Chapter: 9.09 Ordered Mesoporous/Nanoporous Inorganic Materials via Self-Assembly
Book: Comprehensive Supramolecular Chemistry II
Author: T. Asefa, V. Dubovoy
Publisher: Elsevier
Date: 2017
 Copyright © 2017 Elsevier Ltd. All rights reserved.

Logged in as:
 Viktor Dubovoy
 Rutgers, The State University of New Jersey
 Account #: 3001505504

[LOGOUT](#)

Order Completed

Thank you for your order.

This Agreement between Rutgers, The State University of New Jersey -- Viktor Dubovoy ("You") and Elsevier ("Elsevier") consists of your license details and the terms and conditions provided by Elsevier and Copyright Clearance Center.

Your confirmation email will contain your order number for future reference.

[printable details](#)

License Number	4654400012933
License date	Aug 22, 2019
Licensed Content Publisher	Elsevier
Licensed Content Publication	Elsevier Books
Licensed Content Title	Comprehensive Supramolecular Chemistry II
Licensed Content Author	T. Asefa, V. Dubovoy
Licensed Content Date	Jan 1, 2017
Licensed Content Pages	36
Type of Use	reuse in a thesis/dissertation
Portion	figures/tables/illustrations
Number of figures/tables/illustrations	15
Format	both print and electronic
Are you the author of this Elsevier chapter?	Yes
Will you be translating?	No
Original figure numbers	Figures 1-5, 9-10, 23-26 Tables 1-2
Title of your thesis/dissertation	Development of novel antimicrobial functional materials comprising quaternary ammonium compounds and mesoporous silica nanoparticles
Expected completion date	Oct 2019
Estimated size (number of pages)	190
Requestor Location	Rutgers, The State University of New Jersey 57 US Highway 1 NEW BRUNSWICK, NJ 08901 United States Attn: Viktor Dubovoy
Publisher Tax ID	98-0397604
Total	0.00 USD

[ORDER MORE](#)
[CLOSE WINDOW](#)

Copyright © 2019 [Copyright Clearance Center, Inc.](#) All Rights Reserved. [Privacy statement](#), [Terms and Conditions](#).
 Comments? We would like to hear from you. E-mail us at customercare@copyright.com



RightsLink®

[Home](#)
[Create Account](#)
[Help](#)


ACS Publications
Most Trusted. Most Cited. Most Read.

Title: One-Pot Hydrothermal Synthesis of Benzalkonium-Templated Mesoporous Silica Antibacterial Agents

Author: Viktor Dubovoy, Anjani Ganti, Tao Zhang, et al

Publication: Journal of the American Chemical Society

Publisher: American Chemical Society

Date: Oct 1, 2018

Copyright © 2018, American Chemical Society

LOGIN

If you're a [copyright.com](#) user, you can login to RightsLink using your copyright.com credentials. Already a RightsLink user or want to [learn more?](#)

PERMISSION/LICENSE IS GRANTED FOR YOUR ORDER AT NO CHARGE

This type of permission/license, instead of the standard Terms & Conditions, is sent to you because no fee is being charged for your order. Please note the following:

- Permission is granted for your request in both print and electronic formats, and translations.
- If figures and/or tables were requested, they may be adapted or used in part.
- Please print this page for your records and send a copy of it to your publisher/graduate school.
- Appropriate credit for the requested material should be given as follows: "Reprinted (adapted) with permission from (COMPLETE REFERENCE CITATION). Copyright (YEAR) American Chemical Society." Insert appropriate information in place of the capitalized words.
- One-time permission is granted only for the use specified in your request. No additional uses are granted (such as derivative works or other editions). For any other uses, please submit a new request.

[BACK](#)

[CLOSE WINDOW](#)

Copyright © 2019 [Copyright Clearance Center, Inc.](#) All Rights Reserved. [Privacy statement](#). [Terms and Conditions](#). Comments? We would like to hear from you. E-mail us at customer@copyright.com



RightsLink®

[Account Info](#)
[Help](#)


Chapter: 9.09 Ordered Mesoporous/Nanoporous Inorganic Materials via Self-Assembly
Book: Comprehensive Supramolecular Chemistry II
Author: T. Asefa, V. Dubovoy
Publisher: Elsevier
Date: Jan 1, 2017
 Copyright © 2017 Elsevier Ltd. All rights reserved.

Logged in as:
 Viktor Dubovoy
 Rutgers, The State University of New Jersey
 Account #: 3001505504
[LOGOUT](#)

Order Completed

Thank you for your order.

This Agreement between Viktor Dubovoy ("You") and Elsevier ("Elsevier") consists of your order details and the terms and conditions provided by Elsevier and Copyright Clearance Center.

License number	Reference confirmation email for license number
License date	Oct, 02 2019
Licensed Content Publisher	Elsevier
Licensed Content Publication	Elsevier Books
Licensed Content Title	Comprehensive Supramolecular Chemistry II
Licensed Content Author	T. Asefa, V. Dubovoy
Licensed Content Date	2017
Licensed Content Pages	36
Type of Use	reuse in a thesis/dissertation
Portion	full chapter
Circulation	5
Format	both print and electronic
Are you the author of this Elsevier chapter?	Yes
Will you be translating?	No
Title of your thesis/dissertation	Development of novel antimicrobial functional materials comprising quaternary ammonium compounds and mesoporous silica nanoparticles
Expected completion date	Oct 2019
Estimated size (number of pages)	190
Requestor Location	Rutgers, The State University of New Jersey 57 US Highway 1 NEW BRUNSWICK, NJ 08901 United States Attn: Viktor Dubovoy
Publisher Tax ID	98-0397604
Billing Type	Invoice
Billing address	Rutgers, The State University of New Jersey 57 US Highway 1 NEW BRUNSWICK, NJ 08901 United States Attn: Viktor Dubovoy
Total	0.00 USD